



Three-dimensional patterns in cylindrical Rayleigh-Benard convection

Katarzyna Boronska

► To cite this version:

Katarzyna Boronska. Three-dimensional patterns in cylindrical Rayleigh-Benard convection. Fluid Dynamics [physics.flu-dyn]. Université Paris-Diderot - Paris VII, 2005. English. NNT: . tel-00337840

HAL Id: tel-00337840

<https://theses.hal.science/tel-00337840>

Submitted on 9 Nov 2008

HAL is a multi-disciplinary open access archive for the deposit and dissemination of scientific research documents, whether they are published or not. The documents may come from teaching and research institutions in France or abroad, or from public or private research centers.

L'archive ouverte pluridisciplinaire **HAL**, est destinée au dépôt et à la diffusion de documents scientifiques de niveau recherche, publiés ou non, émanant des établissements d'enseignement et de recherche français ou étrangers, des laboratoires publics ou privés.

UNIVERSITE PARIS 7 – DENIS DIDEROT
UFR DE PHYSIQUE

DOCTORAT
Mécanique des fluides

KATARZYNA MĄCZYŃSKA BOROŃSKA

MOTIFS TRIDIMENSIONNELS DANS LA CONVECTION
DE RAYLEIGH–BENARD CYLINDRIQUE

Thèse dirigée par L. S. Tuckerman

Soutenue le 19 septembre 2005

JURY

M. Yves Couder, Président
M. Daniel Henry
M. Patrice LeGal
M. Tom Mullin
Mlle Caroline Nore
Mme Laurette S. Tuckerman
M. Paul Manneville

UNIVERSITE PARIS 7 – DENIS DIDEROT

Ph.D. Thesis
Fluid Mechanics

KATARZYNA MĄCZYŃSKA BOROŃSKA

THREE-DIMENSIONAL PATTERNS IN CYLINDRICAL
RAYLEIGH–BENARD CONVECTION

Supervisor: L. S. Tuckerman

Defended September 19th 2005

Résumé

Nous simulons numériquement les équations de Boussinesq pour la convection de Rayleigh-Bénard en récipient cylindrique. Dans la première partie, pour un rapport d'aspect d'environ 1.5, le nombre de Prandtl 1 et parois verticales isolantes, une transition d'un écoulement stationnaire axisymétrique vers des écoulements non-stationnaires est étudiée, par moyens de simulations non-linéaires, analyse de stabilité linéaire et théorie de bifurcations. Pour un nombre de Rayleigh d'environ 25000, l'état axisymétrique devient instable vers les ondes azimutales stationnaires ou progressives. Les ondes stationnaires sont légèrement instables vers les ondes progressives. Ce scénario est identifié comme une bifurcation de Hopf dans un système avec une symétrie $O(2)$. Dans la deuxième partie nous étudions le phénomène de coexistence d'états stables pour le rapport d'aspect 2, le nombre de Prandtl 6.7 et les parois verticales soit parfaitement isolantes, soit parfaitement conductrices. En faisant varier le nombre de Rayleigh et les conditions initiales, nous obtenons une grande variété de motifs convectifs pour le même nombre de Rayleigh. Nous donnons un diagramme de bifurcations préliminaire, montrant les branches stables. Les résultats pour les parois verticales parfaitement isolantes sont en bon accord avec les expériences.

Summary

We simulate the Boussinesq equations for Rayleigh-Bénard convection in a cylindrical container. In the first part, for aspect ratios near 1.5, Prandtl number 1 and insulating sidewalls, the transition from an axisymmetric stationary flow to time-dependent flows is studied using nonlinear simulations, linear stability analysis and bifurcation theory. At a Rayleigh number near 25000, the axisymmetric flow becomes unstable to standing or travelling azimuthal waves. The standing waves are slightly unstable to travelling waves. This scenario is identified as a Hopf bifurcation in a system with $O(2)$ symmetry. In the second part of the study we investigate the phenomenon of coexisting stable states, using the aspect ratio 2, Prandtl number 6.7 and either perfectly insulating or perfectly conducting sidewalls. Varying Rayleigh number and initial conditions, we obtain various convective patterns for the same Rayleigh number. We show also a preliminary bifurcation diagram containing stable branches. The results for perfectly insulating sidewalls are in good agreement with experiments.

Contents

Résumé	11
1 Rayleigh–Bénard instability	27
1.1 Rayleigh–Bénard instability	27
1.1.1 Instability	27
1.1.2 Rayleigh–Bénard convection	27
1.1.3 Rayleigh number and convection onset	28
1.1.4 Secondary flows and Prandtl number	28
1.1.5 Higher Rayleigh numbers	29
1.1.6 Investigation tools	29
1.2 Cylindrical system	30
1.2.1 Features of the system	30
1.2.2 Azimuthal wavenumber	30
1.2.3 Large aspect ratios	31
1.2.4 Small aspect ratios	31
1.3 Motivation	33
2 Governing equations	35
2.1 Navier–Stokes equations	35
2.2 Boundary conditions	36
2.3 Linear analysis	36
2.3.1 Linearised equations	36
2.3.2 Power method	37
2.3.3 Complex eigenvalues	38
2.4 Symmetries	38
2.4.1 Symmetries of Boussinesq equations	38
2.4.2 \mathbb{Z}_2 symmetry and inverse patterns	38
2.4.3 $O(2)$ symmetry	39
2.4.4 Representations of complex eigenvectors in $O(2)$ symmetry	39
2.5 Amplitude equations and normal form	41
3 Numerical integration	43
3.1 Spectral discretisation – Galerkin projection	43
3.1.1 Galerkin decomposition	43
3.1.2 Fourier series in θ	43
3.1.3 Chebyshev polynomials in z	44
3.1.4 Chebyshev polynomials in r	44
3.2 Time discretisation	45
3.3 Influence matrix	46

3.3.1	Tau method	46
3.3.2	Velocity–pressure decoupling	46
3.3.3	Influence matrix	46
3.3.4	Tau correction	48
3.4	Linear simulation	48
3.4.1	Power method	48
3.4.2	Arnoldi–Krylov method	49
3.4.3	Calculating the base state	49
3.5	Code vectorisation	49
3.6	Program output	51
3.7	Visualisation	51
4	Code validation	53
4.1	Choice of resolution	53
4.2	Choice of timestep	57
4.3	Choice of parameters for linear runs	57
4.4	Convergence criteria	57
4.5	Test cases	57
5	Standing and travelling waves	61
5.1	Oscillatory bifurcation of the axisymmetric state — linear analysis	61
5.1.1	Steady axisymmetric state	61
5.1.2	Eigenvalues and eigenvectors	61
5.2	Nonlinear simulation of time-dependent states	64
5.2.1	Weakly unstable standing waves	64
5.2.2	Stable travelling waves	67
5.2.3	Amplitudes and frequencies	67
5.2.4	Normal form coefficients	68
5.3	Conclusion	69
6	Convective patterns – insulating sidewalls	71
6.1	Simulation of the experiment	71
6.2	Evolution from perturbed conductive state	72
6.3	Three-roll patterns	72
6.4	Evolution from four-rolls	74
6.5	Evolution from pizza pattern	75
6.6	Evolution from two rolls	77
6.7	Axisymmetric flows	77
6.8	Evolution from mercedes pattern	77
6.9	Evolution from dipole pattern	78
6.10	Dipole-shaped perturbation	80
6.11	Summary diagram	82
7	Convective patterns – conducting sidewalls	85
7.1	Start from perturbed conductive state	85
7.2	Three rolls	85
7.3	Four rolls	87
7.4	Evolution from dipole pattern	87
7.5	Evolution from hourglass pattern	87

CONTENTS	9
-----------------	----------

7.6 Evolution from star pattern	88
7.7 Evolution from da Vinci pattern	89
7.8 Evolution from Y pattern	89
7.9 Summary diagram	89

8 Conclusion	91
---------------------	-----------

Resumé

0.1 Instabilité de Rayleigh–Bénard

0.1.1 Mouvements convectifs

L'instabilité de Rayleigh–Bénard apparaît si une couche de fluide confinée horizontalement, chauffée par le bas et refroidie par le haut, est soumise au champ de gravité. Un gradient vertical de densité est alors créé, avec le fluide le plus lourd en haut. Une telle situation correspond à un équilibre de forces qui peut être stable ou instable – si l'on y introduit une perturbation, elle sera dissipée ou provoquera une évolution du système vers un autre état. La situation où le fluide reste au repos est appelée état conductif. L'équilibre entre les facteurs stabilisant et déstabilisant dans cette situation est décrit par le nombre de Rayleigh

$$Ra \equiv \frac{g\gamma d^3}{\kappa v} \Delta T,$$

où d est l'épaisseur de la couche du fluide, κ sa diffusivité thermique, v sa viscosité cinématique, γ le coefficient d'expansion thermique, ΔT la différence de températures entre les plaques et g l'accélération gravitationnelle. Lord Rayleigh (1916) a trouvé que, pour une couche de fluide entre deux plaques infinies, les mouvements convectifs apparaissent au-dessus du nombre critique $Ra_c = 1708$. Pour les systèmes d'extension finie, le nombre de Rayleigh critique dépend du rapport de forme hauteur sur largeur.

Au-dessus du nombre de Rayleigh critique, des écoulements convectifs apparaissent : le fluide chaud et léger monte, se refroidit en montant, puis devient froid, donc lourd, et redescend. Ce cycle est à l'origine des rouleaux représentés dans la figure 1. Une grande variété d'écoulements convectifs a été observée : rouleaux convectifs, droits ou courbés, parallèles ou concentriques, formes spirales ou cibles ainsi que des combinaisons plus complexes.

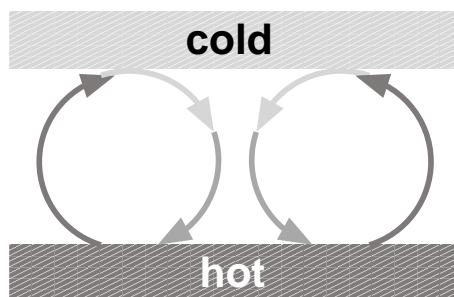


Figure 1: Représentation schématique des rouleaux convectifs : une partie du fluide chaude et légère monte, poussée par la poussée d'Archimède, se refroidit près de la surface supérieure froide et redescend.

L'écoulement qui apparaît au seuil de la convection est souvent appelé écoulement primaire. Si l'on augmente le nombre de Rayleigh, cet écoulement peut perdre sa stabilité en faveur d'un écoulement secondaire. Cette transition est régie non seulement par le nombre de Rayleigh, mais aussi par le nombre de Prandtl, défini comme le rapport entre la viscosité cinématique et le coefficient de diffusion thermique du fluide

$$Pr \equiv \frac{\nu}{\kappa}.$$

Dans notre projet, nous avons étudié la convection de Rayleigh–Bénard dans un récipient cylindrique avec un petit rapport de forme $\Gamma \equiv \text{rayon}/\text{hauteur}$ entre 1.5 et 2.0. Dans la cavité cylindrique, il est naturel de représenter la dépendance des champs physiques en fonction de la direction azimutale θ en utilisant la décomposition de Fourier

$$f(r, z, \theta) = \sum_m \hat{f}(r, z) \exp(im\theta).$$

A cause de l'influence des parois verticales, il arrive souvent que, dans la forme du motif convectif, seul un mode $\exp(im\theta)$ est visiblement dominant. Le nombre d'onde correspondant m est alors utilisé pour décrire la périodicité spatiale de la structure de l'écoulement.

Plusieurs études, théoriques, expérimentales et numériques, d'écoulements convectifs dans des boîtes cylindriques ont été effectuées (§ 1.2.3 and 1.2.4). Deux d'entre elles sont à l'origine de notre projet. Dans la première, Wunschura, Kuhlmann & Rath (1996) ont étudié la stabilité linéaire d'écoulements primaires axisymétriques pour $Pr = 1$. Pour $1.45 \leq \Gamma \leq 1.57$ ils ont observé une bifurcation oscillatoire vers un état instationnaire caractérisé par le nombre d'onde azimutal $m = 3$ ou $m = 4$. Selon la théorie de la bifurcation de Hopf dans des systèmes avec symétries, le nouvel écoulement devrait avoir la forme d'ondes azimutales, soit stationnaires, soit progressives. L'étude étant linéaire, il n'était pas possible de vérifier laquelle de ces deux solutions possibles devait succéder à l'écoulement axisymétrique. Puisque les écoulements oscillatoires ne sont pas très courants dans la convection dans des petites boîtes cylindriques, nous avons décidé d'étudier cette transition suggérée par Wunschura *et al.* (1996) à l'aide de calculs d'analyse linéaire, de simulations non linéaires et de comparaisons avec les scénarios théoriques (voir chapitre 5).

La deuxième partie de notre projet a été inspirée par l'étude expérimentale de Hof, Lucas & Mullin (1999). Ces derniers ont utilisé un récipient cylindrique de rapport de forme $\Gamma = 2$, rempli avec de l'eau ($Pr = 6.7$). En faisant varier le nombre de Rayleigh suivant différentes séquences, ils ont réussi à obtenir plusieurs états stables pour le même nombre de Rayleigh final. Pour $Ra = 14\,200$, ils ont observé cinq types d'écoulements stationnaires : deux, trois et quatre rouleaux parallèles, un motif *mercedes* avec trois zones radiales de fluide descendant ou montant et même un état axisymétrique. Le phénomène de coexistence d'un grand nombre d'états stables est bien connu pour la convection dans les grandes boîtes cylindriques, mais moins bien décrit pour les cylindres avec petits Γ . Dans le but de reproduire et compléter les résultats de Hof *et al.* (1999), nous avons lancé plusieurs séries de simulations pour $Pr = 6.7$, $\Gamma = 2.0$, en faisant varier le nombre de Rayleigh et les conditions initiales. Nous avons utilisé deux types de conditions thermiques aux parois latérales : soit parfaitement isolantes (chapitre 6) soit parfaitement conductrices (7).

0.2 Equations

Nous considérons un fluide confiné dans un cylindre de profondeur d et de rayon R (figure 2). La viscosité cinématique du fluide est ν , la densité ρ , la diffusivité thermique κ et le coefficient

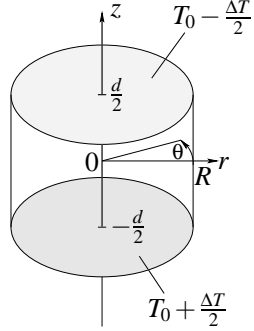


Figure 2: Géométrie de la cavité et système de coordonnées.

d'expansion thermique (à pression constante) γ . La plaque haute est maintenue à la température $T_0 - \Delta T/2$ et la plaque basse à $T_0 + \Delta T/2$. En utilisant les unités d^2/κ , d , κ/d et $\nu\kappa/\gamma gd^3$ pour adimensionner le temps, la distance, la vitesse et la température, nous obtenons la forme adimensionnée des équations de Navier–Stokes sous l'hypothèse de Boussinesq suivantes :

$$Pr^{-1} (\partial_t \mathbf{u} + (\mathbf{u} \cdot \nabla) \mathbf{u}) = -\nabla p + \Delta \mathbf{u} + h \mathbf{e}_z \quad (1a)$$

$$\partial_t h + (\mathbf{u} \cdot \nabla) h = Ra u_z + \Delta h \quad (1b)$$

$$\nabla \cdot \mathbf{u} = 0. \quad (1c)$$

La température adimensionnée T vaut alors $T = \tilde{T}_0 - z + h$, où \tilde{T}_0 est la température T_0 adimensionnée et h une déviation adimensionnée de la température par rapport au profil linéaire vertical. Les nombres Ra et Pr sont définis comme auparavant.

Nous avons utilisé des conditions aux bords réalistes, avec non-pénétration et non-glissement sur toutes les parois :

$$\mathbf{u} = 0 \quad \text{pour } z = \pm 1/2 \quad \text{ou} \quad r = \Gamma. \quad (2)$$

Nous assupposons que les plaques verticales sont maintenues à une température constante, donc $h = 0$ pour $z = \pm 1/2$. Les parois verticales sont soit parfaitement isolantes, donc $\partial_r h = 0$ pour $r = \Gamma$ (condition de Neumann), soit parfaitement conductrices, donc $h = 0$ en $r = \Gamma$ (condition de Dirichlet).

Un outil important dans une étude de stabilité est l'analyse linéaire. Si (\mathbf{U}, H) est une solution convergée des équations (1), nous pouvons examiner sa stabilité en vérifiant si des petites perturbations autour de cet état meurent ou grandissent, faisant évoluer le système vers un autre type d'écoulement. Si nous dénotons la perturbation par (\mathbf{u}, h) et négligeons les termes non linéaires d'ordre $(\mathbf{u}, h)^2$, nous obtenons les équations linéarisées pour $(\mathbf{U} + \mathbf{u}, H + h)$:

$$Pr^{-1} (\partial_t \mathbf{u} + (\mathbf{U} \cdot \nabla) \mathbf{u} + (\mathbf{u} \cdot \nabla) \mathbf{U}) = -\nabla p + \Delta \mathbf{u} + h \mathbf{e}_z \quad (3a)$$

$$\partial_t h + (\mathbf{U} \cdot \nabla) h + (\mathbf{u} \cdot \nabla) H = Ra u_z + \Delta h \quad (3b)$$

$$\nabla \cdot \mathbf{u} = 0. \quad (3c)$$

Les conditions aux limites sont les mêmes que pour les équations non linéaires (1).

L'évolution linéaire peut être représentée sous la forme

$$\partial_t \begin{pmatrix} \mathbf{u} \\ h \end{pmatrix} = L \begin{pmatrix} \mathbf{u} \\ h \end{pmatrix}. \quad (4)$$

Une solution générale de ce problème est une évolution exponentielle

$$\begin{pmatrix} \mathbf{u} \\ h \end{pmatrix}(t) = e^{Lt} \begin{pmatrix} \mathbf{u} \\ h \end{pmatrix}(t=0). \quad (5)$$

Si l'on décompose le champ initial $(\mathbf{u}, h)(t=0)$ dans la base des vecteurs propres ϕ de l'opérateur L

$$\begin{pmatrix} \mathbf{u} \\ h \end{pmatrix}(t=0) = \sum_i c_i \phi_i, \quad L\phi_i = \lambda_i \phi_i, \quad (6)$$

l'évolution (5) devient

$$\begin{pmatrix} \mathbf{u} \\ h \end{pmatrix}(t) = \sum_i e^{\lambda_i t} c_i \phi_i. \quad (7)$$

Si la solution (\mathbf{U}, H) est stable, chaque perturbation doit décroître, alors tous les λ_i ont une partie réelle négative. Au moment de la bifurcation, la partie réelle d'une valeur propre λ_c devient positive et, après un temps suffisamment long, seul un mode survit, qui est proportionnel au vecteur propre critique ϕ_c . La forme spatiale du vecteur peut fournir une information sur la structure de la nouvelle solution, qui, dans le cas de bifurcation supercritique, sera la somme de la solution de base et du vecteur propre critique, modifiée par les effets non linéaires.

Dans le cas où la valeur propre critique est complexe, $\lambda = \sigma \pm i\omega$, l'évolution temporelle du vecteur propre critique est

$$e^{Lt} \phi^R = e^{\sigma t} (\phi^R \cos(\omega t) - \phi^I \sin(\omega t)) \quad (8a)$$

$$e^{Lt} \phi^I = e^{\sigma t} (\phi^R \sin(\omega t) + \phi^I \cos(\omega t)). \quad (8b)$$

$$\begin{pmatrix} \mathbf{u} \\ h \end{pmatrix}(t) = e^{Lt} \begin{pmatrix} \mathbf{u} \\ h \end{pmatrix}(t=0). \quad (9)$$

L'écoulement va donc osciller entre la forme ϕ^R et ϕ^I (§ 2.3.3).

Deux types de symétrie jouent un rôle important dans la dynamique du système. Le premier type est la symétrie de réflexion par rapport au plan médian $z = 0$. Cette symétrie est brisée lors du déclenchement de la convection, ce qui implique que, pour chaque solution, il existe une autre solution, qui peut être obtenue par la transformation

$$\begin{pmatrix} u_r \\ u_\theta \\ u_z \\ h \end{pmatrix}(r, \theta, z) \mapsto \begin{pmatrix} u_r \\ u_\theta \\ -u_z \\ -h \end{pmatrix}(r, \theta, -z).$$

Le système possède aussi la symétrie $O(2)$ – il est invariant vis-à-vis de réflexions par rapport à chaque plan contenant l'axe $r = 0$ et rotations autour de cette axe. Cette symétrie est brisée lors du passage d'un écoulement axisymétrique vers une structure non axisymétrique. La bifurcation de Hopf en présence de cette symétrie a été largement étudiée théoriquement (§ 2.4.3). Le problème peut être découpé pour chaque mode azimuthal $\exp(im\theta)$. Ensuite, pour chaque nombre d'onde m , le problème peut être découpé en deux sous-problèmes

$$\hat{u}_r(r, z) \cos(m\theta), \quad \hat{u}_\theta(r, z) \sin(m\theta), \quad \hat{u}_z(r, z) \cos(m\theta), \quad \hat{h}(r, z) \cos(m\theta), \quad (10a)$$

et

$$\hat{u}_r(r, z) \sin(m\theta), \quad \hat{u}_\theta(r, z) \cos(m\theta), \quad \hat{u}_z(r, z) \sin(m\theta), \quad \hat{h}(r, z) \sin(m\theta). \quad (10b)$$

Ceci nous donne une espace à quatre dimensions : par exemple, pour le champ h , nous avons

$$\hat{h}^R(r,z)\cos(m\theta), \quad (11a)$$

$$\hat{h}^I(r,z)\cos(m\theta), \quad (11b)$$

$$\hat{h}^R(r,z)\sin(m\theta), \quad (11c)$$

$$\hat{h}^I(r,z)\sin(m\theta). \quad (11d)$$

Les vecteurs propres trouvés dans les deux sous-espaces peuvent être combinés de façon à donner de nouveaux vecteurs propres, correspondant à la même valeur propre, mais avec des formes spatiales différentes (2.4.4).

0.3 Intégration numérique

Nous avons intégré les équations numériquement, en projetant les champs sur les séries de Fourier dans la direction azimutale et sur les polynômes de Chebyshev dans les directions radiale et verticale. Nous avons utilisé un schéma mixte explicite et implicite. Le découplage de la vitesse et de la pression et l'imposition de la divergence nulle ont été implémentés par la méthode de la matrice d'influence. Pour intégrer les équations linéarisées, les mêmes méthodes ont été utilisées. En plus, la méthode d'Arnoldi-Krylov a été implementée pour extraire plusieurs valeurs et vecteurs propres, réels et complexes. Une description détaillée des méthodes numériques utilisées se trouve dans le chapitre 3.

0.4 Validation du code

Plusieurs tests ont été effectués sur le programme de simulation, afin de vérifier le choix de résolution spatiale et du pas de temps (voir chapitre 4). Les résultats ont été aussi comparés avec quelques cas-test, obtenus auparavant.

0.5 Ondes stationnaires et progressives

0.5.1 Analyse linéaire

Nous avons souhaité effectuer une étude approfondie pour les paramètres $Pr = 1$ et $1.45 \leq \Gamma \leq 1.57$, où Wanschura *et al.* (1996) ont observé une bifurcation oscillatoire. Nous avons commencé par l'analyse linéaire. Nous avons calculé la solution non linéaire axisymétrique, qui comprenait un rouleau toroïdal. Nous avons ensuite intégré les équations d'évolution linéarisées autour de cette solution. Cette procédure a été répétée pour plusieurs rapports de forme dans la zone d'intérêt et plusieurs nombres de Rayleigh autour de Ra_{c2} prévu par Wanschura *et al.* (1996). Nous avons obtenu les valeurs propres les plus significatives (avec la plus grande partie réelle) et leurs vecteurs propres (§ 5.1.2). Nous avons déterminé les seuils de bifurcation de Hopf Ra_{c2} , les fréquences critiques et les nombres d'onde azimutaux correspondants. Ces valeurs, dépendantes du rapport de forme, étaient en accord avec les observations de Wanschura (tableau 5.1).

Alors que les vecteurs propres existent dans un espace à quatre dimensions (sinus, cosinus, partie réelle et partie imaginaire), nous avons utilisé seulement un des deux sous-espaces invariants (10a) ou (10b) du problème. En conséquence, les formes spatiales des vecteurs propres que

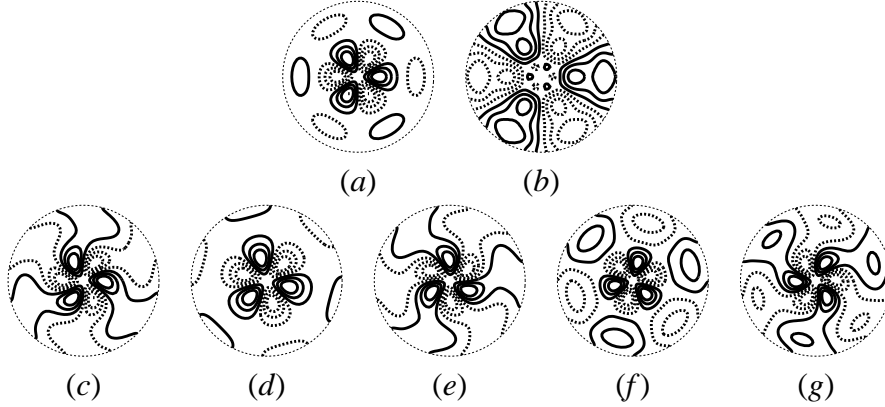


Figure 3: Vecteurs propres pour $\Gamma = 1.47$, $Ra = 25\,000$ (champs de température en $z = 0$): (a) partie réelle du vecteur propre; (b) partie imaginaire du vecteur propre; (c-g) superposition des deux champs via $\hat{h}^R(r,z) \cos(m(\theta - \theta_0)) + \hat{h}^I(r,z) \sin(m(\theta + \theta_0))$, avec $m\theta_0$ égal à : (c) 0, (d) $\pi/4$, (e) $\pi/2$, (f) $3\pi/4$, (g) 0.92π .

nous avons obtenus ont trois axes de symétrie de réflexion ce qui correspond aux ondes stationnaires. Pourtant, à partir d'un vecteur propre complexe, d'autres états peuvent être obtenus qui appartiennent au complémentaire de cette espace. Par exemple, si la composante h du vecteur propre est

$$\hat{h}^R(r,z) \cos(m\theta) + i\hat{h}^I(r,z) \cos(m\theta),$$

de nouveaux vecteurs (parties réelles ou imaginaires) peuvent être générés par

$$C(\hat{h}^R(r,z) \cos(m(\theta - \theta_0)) + \hat{h}^I(r,z) \sin(m(\theta + \theta_0))), \quad (12)$$

(§ 2.4.4 et 5.1.2). Les figures 3(a, b) montrent $\hat{h}^R(r,z) \cos(m\theta)$ et $\hat{h}^I(r,z) \cos(m\theta)$, et les figures 3(c-g) – les formes créées par (12) pour quelques θ_0 . Les ondes progressives tournantes à droite proviennent de $m\theta_0 = 0$ (c), les ondes progressives tournantes à gauche de $m\theta_0 = \pi/2$ (e) et les ondes stationnaires de $m\theta_0 = \pm\pi/4$ (d,f) (deux différentes phases temporelles). L'angle $m\theta_0$ est donc similaire à celui utilisé en figure 7. Un vecteur propre, qui ne correspond ni aux ondes stationnaires ni aux ondes progressives, est montré sur la figure 3(g). Toutes ces visualisations représentent la tranche $z = 0$. Si nous faisons la coupe en $z = 0.3$ du champ présenté sur la figure 3(c), nous retrouvons la forme montrée par Wanschura *et al.* (1996). Néanmoins, nous soulignons que les autres vecteurs propres de la figure 3 sont également valables. Une analyse non linéaire, comme celle présentée en-dessous, est nécessaire pour déterminer si l'écoulement non linéaire final prendra la forme d'ondes stationnaires ou progressives.

0.5.2 Simulation non linéaire des états instationnaires

Au-dessus du nombre de Rayleigh critique Ra_{c2} , l'état axisymétrique légèrement perturbé évolue dans nos simulations vers un écoulement instationnaire tridimensionnel (§ 5.2.1). La figure 4 présente cet état; les contours du champ de température sont visualisés pour six instants durant une période d'oscillations. L'allure des champs est différente des vecteurs propres correspondants car les états non linéaires sont dominés par l'état de base axisymétrique. La structure comprend six extrema qui pulsent en créant une oscillation entre deux formes triangulaires de phases opposées (figures 4, a et 4, d). Les extrema étant fixes, nous identifions cet état comme une onde stationnaire. A chaque instant, l'écoulement est invariant par rapport à une rotation de $\theta = 2\pi/3$.

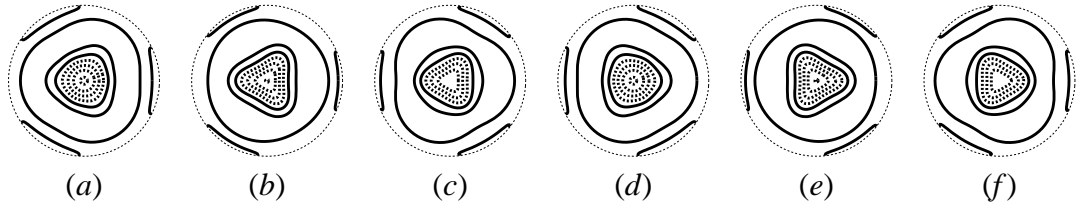


Figure 4: Ondes stationnaires en $Ra = 26000$: contours de température pour $t = 0, T/6, 2T/6, \dots, 5T/6$.

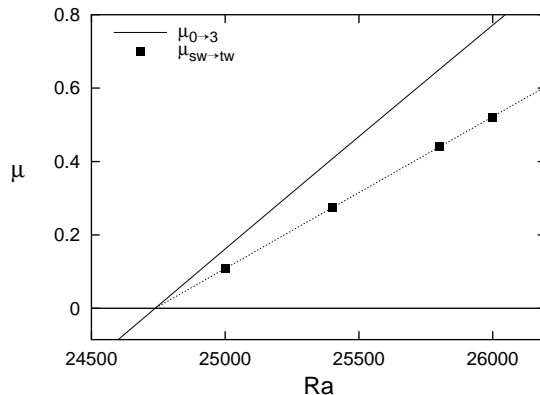


Figure 5: Taux de croissance en fonction du nombre de Rayleigh. Ligne continue : taux de croissance $\mu_{0 \rightarrow 3}$ du vecteur propre $m = 3$ (ondes stationnaires ou progressives) obtenu à partir de l'évolution linéaire autour de l'état axisymétrique. Carrés : taux de croissance $\mu_{SW \rightarrow TW}$ des ondes progressives évoluant vers les ondes stationnaires (obtenus par simulation non linéaire). Ligne pointillée : approximation linéaire.

L'onde stationnaire existe pendant un temps si long qu'elle peut sembler stable. Pourtant, au cours de l'évolution temporelle, une petite imperfection brisant la symétrie de réflexion apparaît, grandit et finalement cause une transition vers une onde progressive. Le temps de vie des ondes stationnaires diminue si l'on augmente le nombre de Rayleigh. Nous avons mesuré le taux de croissance exponentielle de la perturbation qui correspond aux ondes progressives en vérifiant le rapport entre les coefficients symétriques (avec trois axes de symétrie de réflexion) et antisymétriques. Ces taux de croissance, proportionnels au nombre de Rayleigh, sont affichés sur la figure 5. Sur la même figure, nous montrons les taux de croissance du vecteur propre, qui correspondent à l'évolution à partir de l'écoulement axisymétrique vers une onde stationnaire ou progressive et qui sont plus grands que les taux de croissance de l'évolution à partir des ondes stationnaires vers les ondes progressives.

Une fois que la symétrie de réflexion de l'onde stationnaire est brisée, le motif avec les six extrema pulsants évolue vers une structure avec trois sommets tournants – une onde progressive (figure 5.9). La symétrie par rotation de $2\pi/3$ est conservée. Cet état est la forme finale de l'évolution temporelle. La raison pour laquelle nous avons observé d'abord des ondes stationnaires était que nos conditions initiales possédaient la symétrie de réflexion et que nos procédures numériques introduisaient des perturbations asymétriques à un taux très faible. Si le nombre de Rayleigh est diminué, les ondes progressives existent jusqu'à $Ra = Ra_{c2}$.

Nous avons fait des simulations pour plusieurs valeurs du rapport de forme, dans la plage $1.45 \leq \Gamma < 1.53$; pour chaque valeur, nous avons réussi à obtenir les ondes stationnaires et

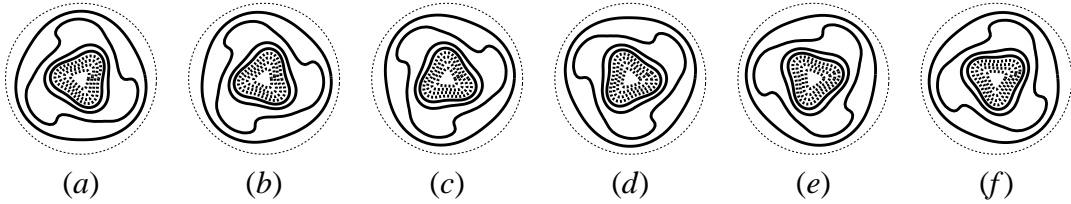


Figure 6: Onde progressive tournante à gauche en $Ra = 26000$: iso-contours de température pour $t = 0, T/6, 2T/6, \dots, 5T/6$.

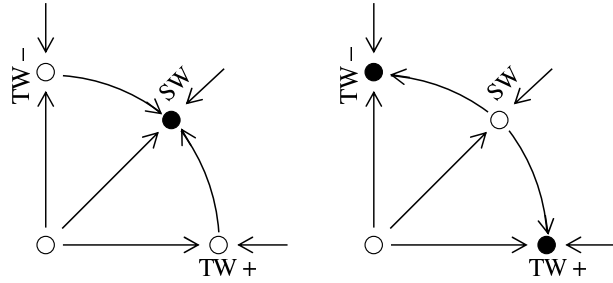


Figure 7: Diagramme de phase illustrant la stabilité des ondes stationnaires (SW) ou des ondes progressives droites (TW+) ou gauches (TW-). Gauche : les ondes stationnaires sont stables; droite : les ondes progressives sont stables. L'origine correspond à la solution axisymétrique et les axes aux amplitudes des ondes progressives tournantes à droite ou gauche. Les ondes stationnaires peuvent être construites comme une superposition des deux ondes progressives.

progressives. Le même scénario existe pour $1.53 \leq \Gamma \leq 1.57$, mais avec le nombre d'onde azimuthal $m = 4$ au lieu de $m = 3$. Nous avons calculé les amplitudes et fréquences d'ondes observées (§ 5.2.3). L'amplitude et la fréquence augmentent avec le nombre de Rayleigh. Si le nombre de Rayleigh est diminué jusqu'à Ra_{c2} , l'amplitude tombe à zéro et la fréquence s'approche de la valeur de la fréquence critique issue du calcul linéaire.

L'évolution non linéaire, près du point de bifurcation de Hopf, peut être décrite par les équations d'amplitude de la forme normale correspondante (§ 2.5). Quand la solution axisymétrique perd sa stabilité, de nouvelles solutions naissent : ondes progressives tournantes à gauche, ondes progressives tournantes à droite et ondes stationnaires. La stabilité de ces solutions dépend des coefficients de la forme normale. Si toutes ces nouvelles solutions existent pour $Ra > Rac2$, alors deux scénarios sont possibles : soit les ondes stationnaires sont stables et les ondes progressives droites et gauches sont instables, soit l'inverse (figure 7). A l'aide des taux de croissance, amplitudes et fréquences trouvés, nous avons déterminé les valeurs numériques des coefficients de la forme normale (§ 5.2.4).

0.5.3 Conclusion

Nous avons utilisé des simulations non linéaires et des calculs de stabilité linéaire dans le but de mieux comprendre le comportement de la convection de Rayleigh–Bénard dans la zone de paramètres $1.45 \leq \Gamma \leq 1.57$, $Pr = 1$, étudiée pour la première fois par Wanschura *et al.* (1996). Dans ce régime, l'état convectif primaire perd sa stabilité vis-à-vis d'une perturbation de mode azimuthal $m = 3$ ou $m = 4$, via une bifurcation de Hopf, où l'espace propre a quatre dimensions. Nous avons calculé les vecteurs propres et expliqué le rapport entre eux et les formes montrées

par Wanschura *et al.* (1996). La théorie prévoit que, au moment de la bifurcation de Hopf, deux branches devraient être créées, correspondant aux ondes stationnaires et progressives, et que, au maximum, une de ces nouvelles branches est stable. Dans nos simulations non linéaires, nous avons observé des ondes stationnaires qui existent longtemps et qui cèdent finalement la place aux ondes progressives. Nous avons expliqué ce comportement en montrant que le taux de transition des ondes stationnaires vers les ondes progressives, tout en étant positif, est petit. En l'absence d'une longue intégration temporelle et de ces analyses, il aurait été possible de conclure prématurément que les ondes stationnaires étaient stables. Ceci souligne l'importance du calcul des taux de croissance (en plus des simulations non linéaires) et l'utilisation des scénarios de bifurcations décrits auparavant pour interpréter les phénomènes physiques.

0.6 Motifs convectifs – parois isolantes

0.6.1 Simulation de l'expérience

La deuxième partie de nos études a été inspirée par l'expérience de Hof *et al.* (1999), qui ont obtenu, en changeant le nombre de Rayleigh suivant différents chemins, plusieurs structures convectives stables pour la même configuration de paramètres de contrôle. Notre but a été de simuler et peut-être compléter leur étude. En accord avec leur paramètres, nous avons choisi le nombre de Prandtl $Pr = 6.7$ et le rapport de forme $\Gamma = 1$. Quant aux parois verticales, qui, dans l'expérience de Hof *et al.* (1999), étaient d'une mauvaise conductivité, nous les avons supposées parfaitement isolantes dans la première série de simulations. Nous avons ensuite utilisé une intégration temporelle en faisant varier à chaque lancement le nombre de Rayleigh et les conditions initiales et nous avons observé vers quel motif asymptotique le système évoluait. Ce protocole nous a permis d'obtenir plusieurs motifs convectifs pour le même nombre de Rayleigh. La figure 8 présente les résultats obtenus pour les parois isolantes; pour chaque motif, le diagramme indique la zone de Ra où l'écoulement de ce type existe, et le nouvel état vers lequel le système évolue, si la solution convergée est utilisée comme condition initiale au-delà de cette zone. Les visualisations des conditions initiales utilisées et des motifs finaux obtenus se trouvent sur la figure 9.

0.6.2 Initialisation avec l'état conductif perturbé

Nous avons commencé les simulations en initialisant les champs avec la solution conductive, légèrement perturbée (cf figure 9, *a*). La perturbation évolue alors vers un écoulement convectif, dont la forme dépend du nombre de Rayleigh. Pour $Ra \lesssim 1900$, la perturbation initiale diminue vers zéro, en donnant naissance à l'état conductif. Pour Ra d'environ 2000, l'état final, que nous avons appelé *pizza*, est un motif invariant par la symétrie D_2 , avec quatre parties distinctes, qui ressemble à des parts de pizza. Chaque section a soit une zone chaude dans son centre et une zone froide le long de la paroi, soit l'inverse (figure 9, *b*). Pour $3000 \leq Ra < 10000$, la perturbation initiale évolue vers quatre rouleaux quasi parallèles (figure 9, *c*) et pour $10000 \leq Ra \leq 20000$ vers trois rouleaux quasi parallèles (figure 9, *d*). Les rouleaux deviennent plus courbés quand le nombre de Rayleigh croît. Enfin, pour $Ra \approx 23000$, l'état final est composé de trois zones radiales de fluide froid, nommé par Hof (1997) *motif mercedes* (figure 9, *e*).

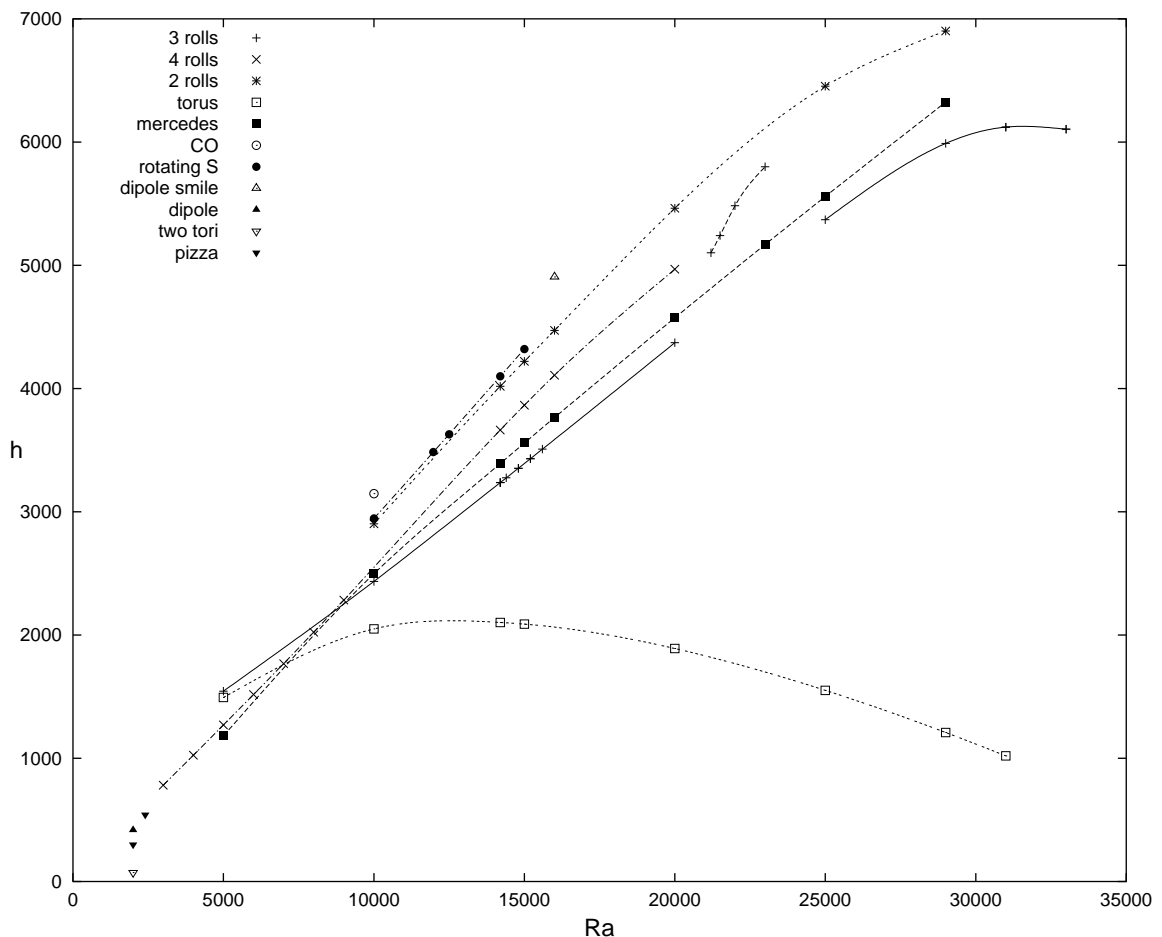


Figure 8: Diagramme résumant les résultats pour les parois isolantes : température $\max_{\theta} h(r = 0.3, \theta, z = 0)$ en fonction du nombre de Rayleigh pour tous les états convectifs stables trouvés.

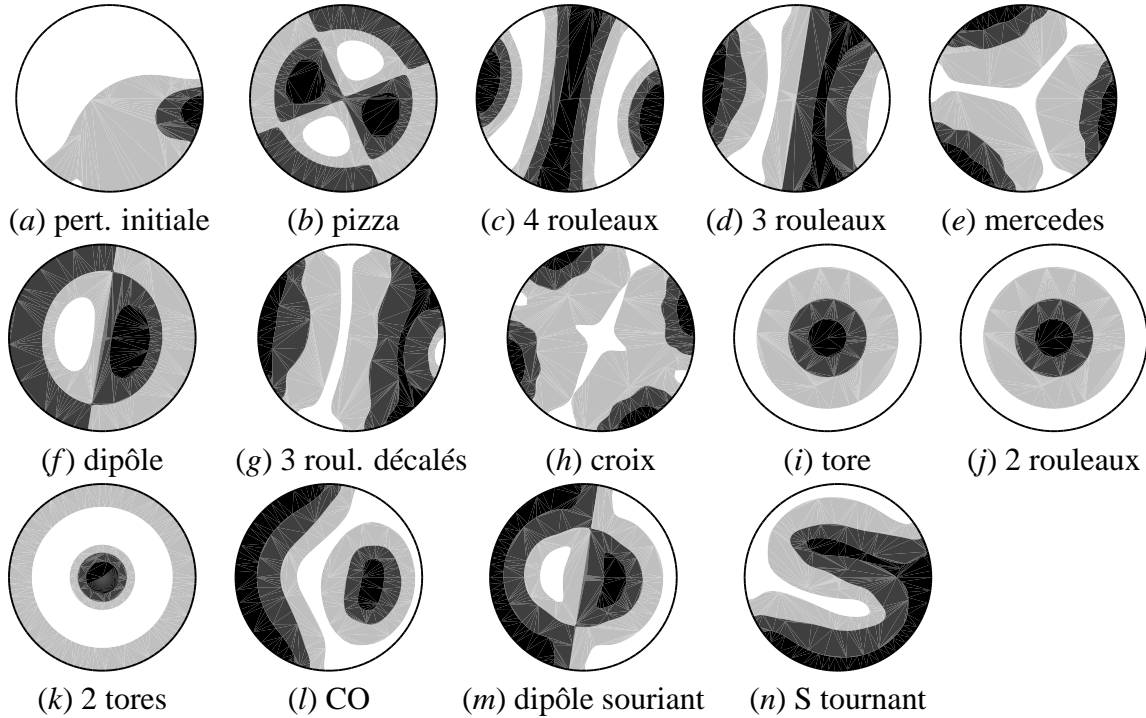


Figure 9: Motifs convectifs trouvés pour les parois verticales isolantes : visualisation de la température (*h*) dans le plan médian $z = 0$. Les parties foncées correspondent au fluide plus chaud (montant) et les zones claires au fluide plus froid (descendant).

0.6.3 Trois rouleaux

Ayant obtenu les solutions en forme de trois rouleaux dans la série de simulations précédente, nous avons repris la solution convergée à $Ra = 14\,200$, et nous l'avons fourni au code comme champ initial pour un autre nombre de Rayleigh. En-dessous du seuil de convection, la vitesse tend vers zéro et la structure de l'écoulement, avant de disparaître, change pour prendre la forme d'un dipôle. Pour $Ra = 2\,000$, les trois rouleaux évoluent vers un écoulement dipôle stable (figure 9,*f*). Entre $Ra = 5\,000$ et $Ra = 33\,000$, les trois rouleaux sont stables, sauf pour $20\,000 < Ra < 25\,000$, où le rouleau central est déplacé par rapport au diamètre central (figure 9,*g*). Nous avons conclu l'existence d'une bifurcation dans cette zone (figure 6.6). Dans l'expérience, cela a donné finalement deux rouleaux pour $Ra = 21\,000$, mais nous n'avons pas observé une telle transition.

0.6.4 Quatre rouleaux

Ayant utilisé une structure à quatre rouleaux comme condition initiale, nous avons obtenu quatre rouleaux stables pour $3\,000 \leq Ra \leq 20\,000$. Pour $Ra \geq 25\,000$, la structure évolue vers une croix (figure 9, *h*), qui est probablement transitoire.

0.6.5 Evolution de l'écoulement de type pizza

Dans cette série de simulations, nous avons utilisé comme condition initiale l'état pizza obtenu auparavant à $Ra = 2\,000$. Pour $5\,000 \leq Ra \leq 29\,000$ ce motif évolue vers une autre structure. En $Ra = 5\,000$ l'état final est l'état à quatre rouleaux, pour $Ra = 10\,000$ trois rouleaux, pour $Ra = 14\,200$ un état axisymétrique comprenant un rouleau toroïdal (figure 9, *i*), et pour $15\,000 \leq$

$Ra \leq 29000$, deux rouleaux (figure 9, *j*). Pendant l'évolution vers les deux rouleaux, le système passe par une suite d'états intermédiaires (§ 6.5).

0.6.6 Deux rouleaux

L'écoulement avec deux rouleaux, utilisé comme condition initiale pour les simulations pour des nombres de Rayleigh variés, garde sa forme pour $10000 \leq Ra \leq 29000$. Pour $Ra = 5000$, il évolue vers la solution à trois rouleaux et, pour $Ra = 2000$, vers l'état pizza. A $Ra = 29000$, les contours des rouleaux vibrent légèrement.

0.6.7 Etats axisymétriques

Le motif axisymétrique (obtenu à $Ra = 14200$) utilisé comme condition initiale donne aussi des motifs axisymétriques pour une grande plage de nombres de Rayleigh $2000 \leq Ra \leq 33000$. Ceci est en accord partiel avec l'expérience, où Hof *et al.* (1999) ont trouvé cet écoulement instable vers une forme tournante pour $Ra \geq 23000$. A $Ra = 2000$, l'état axisymétrique comprend deux rouleaux toroïdaux concentriques (figure 9, *k*).

0.6.8 Evolution de la forme de type mercedes

Nous avons lancé une série de simulations initialisées avec le motif mercedes (figure 9, *e*). Pour chaque nombre de Rayleigh utilisé dans l'intervalle $5000 \leq Ra \leq 29000$, l'écoulement garde sa forme et, pour $Ra = 2000$, il évolue vers l'état axisymétrique avec deux tores.

0.6.9 Evolution de l'état dipôle

L'état dipôle, observé à $Ra = 2000$, n'est pas stable pour des nombres de Rayleigh plus grands. Fourni comme condition initiale, il évolue vers trois rouleaux pour Ra entre 5000 et 29 000, à l'exception de 10 000. A $Ra = 10000$ l'état final, que nous avons nommé CO, a un rouleau semi-circulaire et un rouleau toroïdal (figure 9, *l*). Au cours de l'évolution vers l'état à trois rouleaux ou le CO, une structure transitoire *dipôle souriant* apparaît (figure 9, *m*).

0.6.10 Perturbation en forme de dipôle

Finalement, nous avons initialisé les simulations avec l'écoulement transitoire de dipôle, qui apparaît en-dessous du seuil de convection avant que les mouvements convectifs s'arrêtent. L'amplitude du champ que nous avons utilisé est déjà très petite, ce qui nous amène à considérer cet état comme une perturbation à la solution conductive plutôt que comme un état convergé. Ceci est différent de la première série de simulations seulement par la forme de la perturbation – au début, nous avons perturbé la solution triviale avec un mélange arbitraire de modes, alors qu'ici la perturbation utilisée a été observée pendant l'évolution du système. Pour ces deux types de conditions initiales, les motifs finaux sont différents. La perturbation en forme de dipôle évolue vers un dipôle à $Ra = 2000$ et vers trois rouleaux à $Ra = 10000$. Pour $10000 \leq Ra \leq 15000$, l'état final est un rouleau en forme de lettre S qui tourne à droite, avec une période très grande (de l'ordre de dix temps de diffusion thermique vertical) (figure 9, *n*). Pour $Ra = 16000$, le système évolue vers un dipôle souriant stable. Enfin, pour $20000 \leq Ra \leq 29000$, quelques motifs intermédiaires apparaissent avant l'état final de trois rouleaux.

0.6.11 Remarques

Nous avons observé une coexistence de plusieurs types d’écoulements convectifs pour un nombre de Rayleigh donné. Pour les bas nombres de Rayleigh, de l’ordre de 2000, nous avons déjà trouvé trois motifs : dipôle, deux rouleaux toroïdaux et pizza. Pour les nombres de Rayleigh plus élevés, les états que nous avons observés comme étant stables sur un grande intervalle de Ra sont : deux, trois et quatre rouleaux parallèles, mercedes et un rouleau toroïdal. Ces résultats sont en bon accord avec l’expérience de Hof *et al.* (1999), qui ont observé les cinq mêmes types d’écoulement pour cette plage de nombres de Rayleigh.

Dans le chapitre 6, nous donnons plus d’informations sur les transitions entre les états, les motifs intermédiaires et l’énergie des écoulements observés. Nous présentons aussi un diagramme quantitatif des plages d’existence des motifs stables en fonction du nombre de Rayleigh.

0.7 Motifs convectifs – parois conductrices

0.7.1 Initialisation avec l’état conductif perturbé

Ayant obtenu de nombreux motifs convectifs pour le modèle avec les parois verticales isolantes, nous avons utilisé la même procédure pour un cylindre avec des parois d’une conductivité parfaite (condition aux limites de type Dirichlet). Comme dans le cas précédent, nous avons commencé les simulations en initialisant les champs avec l’état conductif perturbé, en faisant varier le nombre de Rayleigh. Ensuite, nous utilisons les solutions convergées pour initialiser les nouveaux lancements du code pour d’autres Ra . La figure 10 présente, d’une façon schématique, les plages de stabilité des motifs obtenus, et les états vers lesquels évolue le système, s’il est initialisé avec un motif instable pour un nombre de Rayleigh donné. Les motifs sont visualisés sur la figure 11.

Pour $Ra = 1900$ et $Ra = 2000$, la perturbation initiale (figure 11, *a*) évolue vers un écoulement dipôle (figure 11, *b*). Pour 1900 et 2000, l’état final est l’état *sablier* – un motif qui ressemble au motif pizza, sauf que les deux parties froides se rejoignent au centre (figure 11, *c*). Pour $Ra = 2700$ et $Ra = 4000$, le système a évolué vers la solution à trois rouleaux (figure 11, *d*) et, pour $6000 \leq Ra \leq 15\,000$, vers celle à quatre rouleaux (figure 11, *e*). Les différences entre ces rouleaux parallèles et ceux obtenus pour les parois isolantes sont visibles seulement près des parois car ici la déviation du profil linéaire doit être nulle sur les bords. Pour $Ra = 20\,000$ nous avons obtenu un motif *Y*, avec trois bandes de fluide montant selon les rayons, en forme d’une lettre Y (figure 11, *f*). Cet état ressemble au motif mercedes obtenu auparavant, mais il possède seulement une et non pas trois axes de symétrie de réflexion. Pour $Ra = 25\,000$, le système a convergé vers l’état en forme d’étoile avec six rayons de fluide chaud (figure 11, *g*). Finalement, pour $Ra \geq 30\,000$, nous avons obtenu un état que nous avons appelé *da Vinci*, en raison de sa ressemblance avec son esquisse des proportions pour le corps humain (figure 11, *h*). Tous ces écoulements sont stationnaires.

0.7.2 Trois rouleaux

Nous avons utilisé l’état à trois rouleaux convergé à $Ra = 4000$ comme état initial pour des nombres de Rayleigh différents. Ceci nous a donné les écoulements en forme de trois rouleaux pour $3000 \leq Ra \leq 29\,000$, à l’exception de 25 000, où le système a évolué vers deux rouleaux.

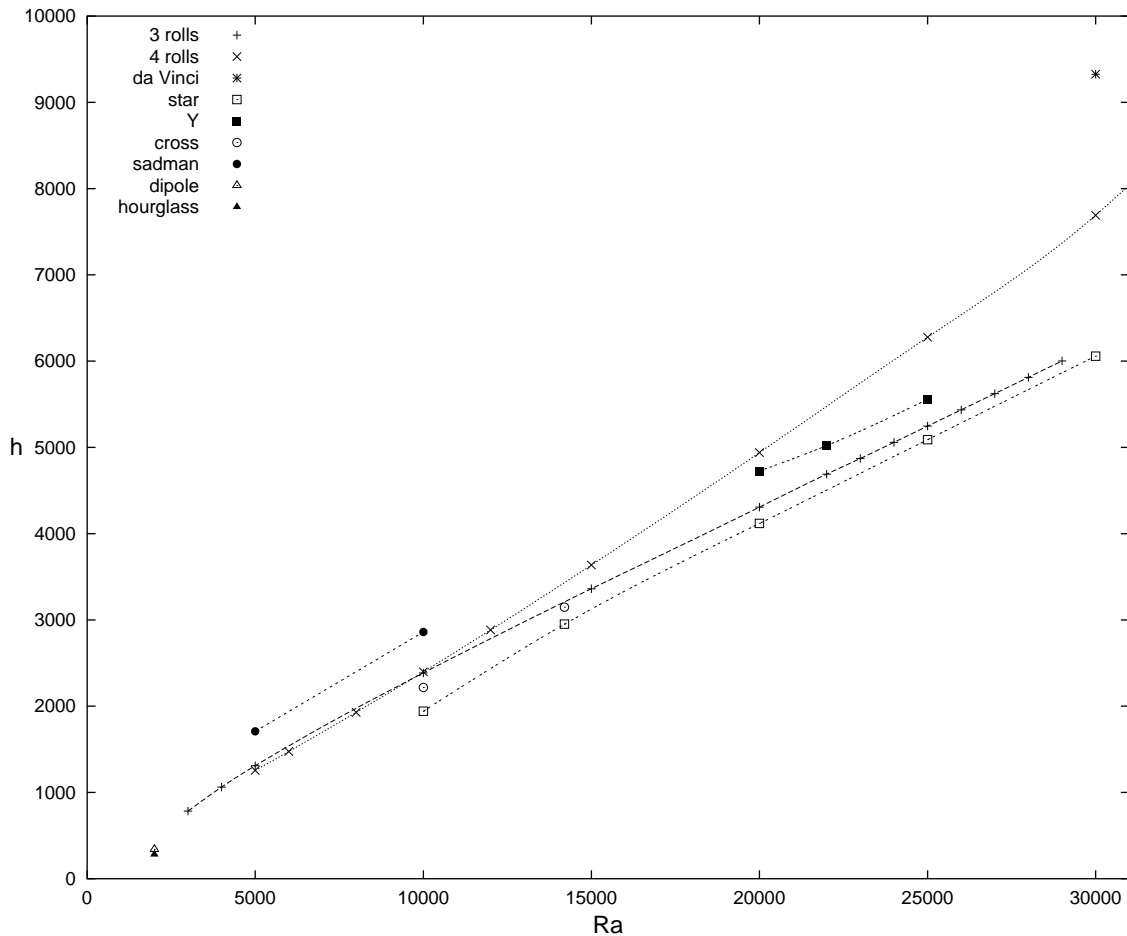


Figure 10: Diagramme résumant les résultats pour les parois conductrices : température $\max_{\theta} h(r = 0.3, \theta, z = 0)$ en fonction du nombre de Rayleigh pour tous les états convectifs stables trouvés.

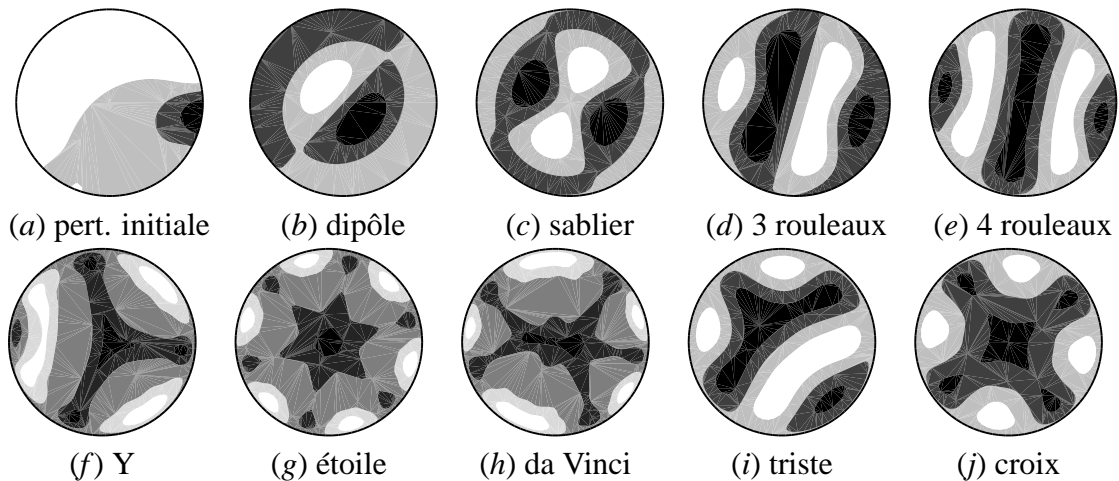


Figure 11: Motifs convectifs trouvés pour les parois conductrices : visualisation de la température (h) dans le plan médian $z = 0$.

Néanmoins, nous avons réussi à obtenir trois rouleaux stables pour $Ra = 25\,000$ en initialisant le système avec trois rouleaux convergés à $Ra = 20\,000$.

0.7.3 Quatre rouleaux

Les écoulements en forme de quatre rouleaux, utilisés comme condition initiale, gardent leur structure pour une grande plage de nombres de Rayleigh $5\,000 \leq Ra \leq 35\,000$. Pour $Ra = 2\,000$ l'écoulement initial évolue vers le motif de dipôle et, pour $Ra = 40\,000$, la structure de quatre rouleaux existe, mais les bords des rouleaux vibrent légèrement, avec une période $T = 0.026$.

0.7.4 Evolution de l'état dipôle

Quand nous utilisons le motif dipôle (convergé en $Ra = 2\,000$) comme condition initiale pour les nombres de Rayleigh plus élevés, l'écoulement évolue vers trois rouleaux pour $Ra = 5\,000$ et quatre rouleaux pour $10\,000 \leq Ra \leq 20\,000$. Pour $Ra = 25\,000$, nous avons obtenu le motif Y. Pour $Ra = 30\,000$ le dipôle évolue vers trois rouleaux; nous savons grâce aux simulations précédentes que cette forme est instable pour ce nombre de Rayleigh et que le système devrait évoluer vers l'état étoile.

0.7.5 Evolution de l'état sablier

Dans les simulations initialisées avec l'état sablier (convergé en $Ra = 2100$), nous avons obtenu : un sablier stable à $Ra = 2\,000$; quatre rouleaux pour $5\,000 \leq Ra \leq 20\,000$; et une étoile de six rayons à $Ra = 25\,000$ et $30\,000$. Pour $Ra = 35\,000$, le dipôle initial a évolué vers un état instationnaire, oscillant entre un écoulement en forme de lettre X penchée à droite et à gauche (figure 7.5, chapitre 7) avec une période $T = 3.05$.

0.7.6 Evolution de l'état étoile

Nous avons obtenu les écoulements en forme d'étoile en initialisant les simulations avec l'état étoile obtenu à $Ra = 25\,000$. Ce motif est stable pour $10\,000 \leq Ra \leq 30\,000$. En-dessous de cette plage, la structure initiale évolue vers un état *triste* (figure 11, i) à $Ra = 5\,000$ et état sablier à $Ra = 2\,000$. Pour ces deux nombres de Rayleigh, un état axisymétrique transitoire apparaît.

0.7.7 Evolution de l'état da Vinci

L'état da Vinci (figure 11, h), utilisé comme condition initiale, est stable seulement pour $Ra \geq 30\,000$. Pour $Ra = 25\,000$ cette structure évolue lentement, probablement vers une étoile de cinq rayons. Pour les nombres de Rayleigh plus bas, l'écoulement initial évolue vers : une étoile à $Ra = 20\,000$, une croix entre 14 200 et 10 000 (figure 11, j), triste à 5 000 et sablier à 2 000.

0.7.8 Evolution de l'état Y

Ayant obtenu l'écoulement Y à $Ra = 20\,000$, nous l'avons utilisé comme condition initiale. Nous l'avons trouvé stable pour $20\,000 \leq Ra < 30\,000$. Pour $Ra = 14\,200$, le système évolue vers trois rouleaux. Pour les nombres de Rayleigh plus bas, nous avons obtenu l'état triste pour 10 000 et 5 000 et sablier pour 2 000. Les états triste et Y se ressemblent; il est donc possible que ce soit le même type d'écoulement.

0.7.9 Remarques

Nous avons réussi à obtenir plusieurs types d'écoulements stables: à bas nombres de Rayleigh, ce sont les états dipôle et sablier, à hauts nombres Ra , ce sont les états trois et quatre rouleaux, da Vinci, étoile, Y et croix. Ceci est différent des résultats obtenus avec les conditions adiabatiques. Dans le chapitre 7, nous donnons un graphe d'énergie des écoulements obtenus (figure 7.9) et un diagramme quantitatif des plages d'existence des motifs stables en fonction du nombre de Rayleigh.

0.8 Conclusion

Nous avons présenté les résultats de nos simulations non linéaires d'écoulements convectifs pour deux configurations différentes. Dans la première partie, nous avons étudié les écoulements convectifs pour les rapports de forme $1.45 \leq \Gamma \leq 1.57$, le nombre de Prandtl $Pr = 1$ et les parois isolantes. Nous avons réalisé une analyse linéaire de stabilité d'états axisymétriques. Les nombres de Rayleigh et les fréquences critiques trouvés sont en accord avec les résultats de Wanschura *et al.* (1996). Nous avons montré une procédure pour obtenir l'ensemble des valeurs et vecteurs propres les plus importants. Notre représentation prend en compte les symétries du système : les vecteurs propres qui correspondent à la même valeur propre peuvent avoir des formes spatiales différentes, avec ou sans lignes nodales. Ainsi nous avons expliqué et complété les résultats de Wanschura *et al.* (1996).

La théorie de la bifurcation de Hopf dans un système avec symétrie $O(2)$ prévoit que l'évolution non linéaire devrait mener vers des ondes azimutales, soit stationnaires, soit progressives. Nous avons vérifié que les ondes progressives sont stables. En plus, nous avons réussi à observer des ondes stationnaires instables. Nous avons évoqué les études théoriques de Golubitsky & Stewart (1985) et Knobloch (1986) de la bifurcation de Hopf en présence de symétrie $O(2)$ et nous avons déterminé les valeurs des coefficients de la forme normale décrite par ces auteurs.

Dans la seconde partie de notre projet, nous avons réalisé plusieurs simulations pour le rapport de forme $\Gamma = 2$ et le nombre de Prandtl $Pr = 6.7$. Ces paramètres ont été utilisés auparavant par Hof, Lucas & Mullin (1999), qui ont observé expérimentalement plusieurs motifs convectifs différents pour un même nombre de Rayleigh. Alors que les parois verticales dans l'expérience sont plutôt bien isolantes, nous avons utilisé deux types de conditions aux limites, en les supposant soit parfaitement isolantes, soit parfaitement conductrices.

Pour les deux types de conditions, nous avons réussi à obtenir plusieurs états stables coexistants, même à bas nombres de Rayleigh. Nous avons décrit la dynamique des motifs convectifs et présenté les diagrammes des états stables coexistants. Le comportement du système dépend fortement des conditions aux limites thermiques. Pour les parois parfaitement isolantes que nous avons obtenu un très bon accord avec les motifs expérimentaux.

Le but de notre projet était de trouver plusieurs états stables. Ceci accompli, nos résultats fournissent une très bonne base pour la réalisation d'un diagramme de bifurcations complet, contenant les états stables et instables.

Chapter 1

Rayleigh–Bénard instability

This chapter contains a basic introduction to convective instabilities. We give a brief sketch of the main results for Rayleigh–Bénard convection in cylindrical containers and we focus on phenomena reported by Hof, Lucas & Mullin (1999) and Wanschura, Kuhlmann & Rath (1996). These two studies define the two sets of control parameters we used in our simulations.

1.1 Rayleigh–Bénard instability

1.1.1 Instability

An instability occurs in a dynamical system when a slight perturbation to a solution does not die, but grows, causing an evolution of the whole system towards another solution. As in the real world, slight perturbations always exist, the stable solution is that observed experimentally. Usually the stability of a given solution depends on several control parameters. This is the case of Rayleigh–Bénard convection, where the stability of the flow structure is determined by the properties of the fluid and its container.

1.1.2 Rayleigh–Bénard convection

Rayleigh–Bénard instability occurs when a fluid layer is heated from below and cooled from above. A vertical temperature gradient is then created, with upper layers heavier than lower layers. The situation in which the fluid remains motionless and its density stratified, is called the conductive state. This state can become unstable in the presence of gravity. If the balance between the stabilising and destabilising forces is favourable to the latter, the onset of convection is observed. Hot zones begin to ascend and then are cooled as they approach the upper plate; cold zones descend, and are heated. Such cycles are at the origin of convective motions, which take the form of rolls (see figure 1.1). A rich variety of convective flows has been reported: convective rolls, straight or curved, can be parallel or concentric, forming targets, spirals, and more complex combinations.

The Rayleigh–Bénard problem is one of several widely-studied convective systems, in which a density variation in the presence of gravity engenders fluid motions. A similar problem is Bénard–Marangoni convection, where the rigid upper plate is replaced by a free surface; surface tension must be then taken into account. In convection in mixtures the instability is driven by a concentration gradient, either with or without the presence of a temperature gradient. In natural convection, the instability occurs in a cavity with differentially heated lateral

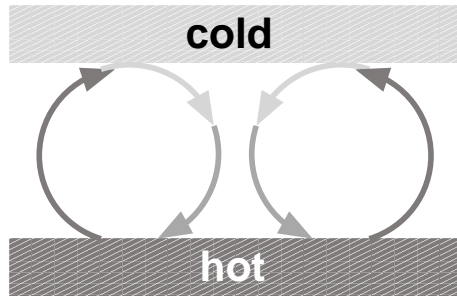


Figure 1.1: Schematic representation of convective rolls: hot fluid ascends, lifted by buoyancy forces, it becomes colder and heavier at the upper cold surface, and then starts to descend.

walls. We should mention here also forced convection, where the flow influencing the temperature field is engendered mainly by forces other than buoyancy. Finally, more complex models are investigated in industrial research.

Convection is an important phenomenon in nature; its comprehension is necessary in understanding the dynamics of such large-scale systems as the atmosphere, the oceans or the interiors of stars and planets (Busse, 1978; Getling, 1998; Marcus, 2004). At smaller scales, the interest in studying convection comes from multiple applications, such as designing heating systems of buildings, controlling crystal growth or constructing cooling systems for electronic devices. Another motivation for studying Rayleigh–Bénard convection comes from the fact that this is a classic pattern-forming system. Formation of patterns and their dynamics are a common challenge occurring in many nonlinear problems, not only in fluid mechanics, but also in condensed-matter physics, chemistry and biology. As patterns observed in different systems can be very similar, there exist attempts to find unifying concepts (e.g. Cross & Hohenberg, 1993); results for one particular configuration can then elucidate the dynamics of another system or contribute to a generalising theory.

1.1.3 Rayleigh number and convection onset

Lord Rayleigh (1916) showed that the balance between effects favourable and unfavourable to convection onset can be described by a dimensionless number, called *the Rayleigh number*. For a fluid layer of depth d , thermal diffusivity κ , kinematic viscosity ν and thermal expansion coefficient (at constant pressure) γ , confined between two parallel plates of temperature difference ΔT , this number is defined by

$$Ra \equiv \frac{g\gamma d^3}{\kappa\nu} \Delta T,$$

where g is gravitational acceleration. Lord Rayleigh found analytically that for plates of infinite extent, convection occurs above the critical number $Ra_{\infty} = 1708$. For finite systems, the critical Rayleigh number and the convective flow structure depend on the form of the lateral boundaries.

1.1.4 Secondary flows and Prandtl number

The flow which appears at the convection onset is often referred to as the primary flow. As the Rayleigh number is increased, this flow can lose its stability to a secondary flow. This transition is governed not only by the Rayleigh number and container form, but also by the *Prandtl number*, defined as the ratio of the kinematic viscosity to the thermal diffusivity of the

fluid

$$Pr \equiv \frac{\nu}{\kappa}.$$

The Prandtl number varies widely: it is of order of 10^{-2} for liquid metals, 1 for gases and up to 10^5 for oils. An extensive study of the stability of parallel rolls in function of their horizontal wavenumber, Rayleigh number and Prandtl number was carried out by Busse and co-workers (Busse, 1978). The stability zone in the three-dimensional parameter space Ra - Pr - k (where k is the wavenumber of the rolls) is therefore called the *Busse balloon*.

1.1.5 Higher Rayleigh numbers

As the Rayleigh number is increased, the convective patterns become more complicated and more irregular, their symmetries and periodicities being successively broken. If we continue to increase Ra , spatio-temporal chaos appears and finally, the flow becomes turbulent. In the present work we focus on lower Rayleigh numbers; the description of turbulent regimes is a separate branch in fluid dynamics research.

1.1.6 Investigation tools

Experiments

Since Bénard's experiments in the beginning of the twentieth century (Bénard, 1901), there has been constant progress in experimental techniques, allowing researchers to vary largely the Prandtl number, to work with quasi-Boussinesq fluids, and to observe the patterns not only in fluids but also in gases (Croquette, 1989). The experiments provide either two-dimensional views of patterns (shadowgraphy technique) or approximate velocity fields (Particle Image Velocimetry), and usually also the Nusselt number, which measures the global heat transport. A great variety of convective patterns has been observed, especially for large rectangular, cylindrical and annular containers (Koschmieder, 1993; Croquette, 1989; Bodenschatz *et al.*, 2000).

Theoretical approaches

Theoretical analysis of convective instabilities, with purely mathematical tools, could be performed only for the simplest cases because of the complexity of the problem – the laws governing the system are described by partial differential equations, which are, in general, three-dimensional, nonlinear and time-dependent. There are some common simplifications: one of them is treating the fluid as incompressible and using the Boussinesq approximation. The latter assumes that the fluid properties do not vary with temperature, except for the density, which varies linearly in the buoyancy term. Sometimes free-slip boundary conditions are used, which substantially facilitates calculations (Rosenblat, 1982). Convective patterns are also modelled by several kinds of amplitude equations, with simpler nonlinearities and vertical dependence maximally reduced (Manneville, 1990).

Linear analysis is a useful method in stability problems. Its principle is to add a small perturbation to a given base solution, linearise the equations (retaining only terms linear in the perturbation), and checking whether the perturbation grows or decreases. If the perturbation decreases, then the base solution is stable. If, increasing a control parameter, we cross a limit above which the base solution is unstable, the initial perturbation grows, evolving into a form called the critical eigenvector. However, as this formalism does not take into account nonlinear effects, linear analysis does not provide quantitative results concerning the new stable solution.

The structure of the critical eigenvector can, at best (in the case of a supercritical bifurcation), give an idea of the symmetry of the new stable solution, which is the sum of the base solution and the eigenvector, modified by nonlinear effects.

Numerical simulations

A new chapter in investigating convective instabilities began with the appearance of computers. At first, numerical computations were used in the last stages of theoretical analysis, or to perform linear analysis for perturbations with different wavenumbers, then slightly nonlinear or simplified models were studied numerically. Finally, fast increase of computer performance and development of numerical methods made feasible three-dimensional, nonlinear, high-resolution simulations of the governing equations.

The incompressibility and Boussinesq approaches are widely used in simulations. This limits the possible range of investigations; incompressible models work only for flow velocities far below the speed of sound and the Boussinesq approximation is adequate only for small temperature gradients. There are also approaches with free-slip boundary conditions (Siggers, 2003), but contrary to the incompressibility and Boussinesq approximation, these models usually give rather unrealistic results (see Wanschura *et al.*, 1996).

Several methods for numerical integration of the governing equations are in use. In the finite difference method, discrete analogs of derivatives are calculated using local values. This method, the simplest in implementation, is still used in some models (Leong, 2002). Finite volume methods, where the equations are integrated over control volumes corresponding to grid-points, have good local conservation properties and are therefore used even at high Rayleigh numbers, where turbulent regimes appear. Finite element methods, with their solid mathematical foundations and a great deal of generality, are appreciated by engineers, as they are suitable for complicated geometries. They are widely used, but rather expensive numerically. Finally spectral methods, based on projecting unknown quantities on series of functions, are the most precise for a fixed number of points, but convenient only for simple geometries. In our simulations we used a spectral code; we describe the projection further, in § 3.1.

1.2 Cylindrical system

1.2.1 Features of the system

In the present work we focus on convective flows in cylindrical containers with aspect ratios $\Gamma \equiv \text{radius}/\text{height}$ between 1.5 and 2.0 and with lateral boundaries that are either perfectly conducting or insulating. The advantage of cylindrical containers in comparison with finite rectangular boxes is the azimuthal symmetry, which permits us to use trigonometric basis functions; The system is invariant under rotation around the vertical axis, which influences the symmetry of the flow patterns. The disadvantage of the cylindrical geometry is the singularity at the cylinder axis.

1.2.2 Azimuthal wavenumber

As the azimuthal direction is periodic, a Fourier decomposition is a convenient representation : $f(r, z, \theta) = \sum_m \hat{f}(r, z) \exp(im\theta)$. Because of the influence of the form of lateral boundaries on the flow geometry, for small aspect ratios there is often only one Fourier mode $\exp(im\theta)$ visi-

bly dominating in a given convective pattern. The corresponding wavenumber is then used to describe the periodicity of the flow structure.

1.2.3 Large aspect ratios

A summary covering the developments since the mid 1980s for convective systems with large aspect ratio ($\Gamma \gg 1$) can be found in Bodenschatz, Pesch & Ahlers (2000). In such domains a great variety of patterns was reported: “Pan Am” patterns (arches with several centres of curvature, see Ahlers, Cannell & Steinberg, 1985), straight parallel rolls (Croquette, 1989; Croquette, Le Gal & Pocheau, 1986), concentric rolls (targets, see Koschmieder & Pallas, 1974; Croquette, Mory & Schosseler, 1983), one- and several- armed rotating spirals (Plapp, Egolf, Bodenschatz & Pesch, 1998), targets with dislocated centre (Croquette, 1989), hexagonal cells (Ciliberto, Pampaloni & Pérez-García, 1988) and spiral-defect chaos (Morris *et al.*, 1993). A large overview on convective phenomena observed experimentally before this time can also be found in Koschmieder (1993).

1.2.4 Small aspect ratios

We focus on cylinders with moderate aspect ratio $\Gamma \sim 1$. The flow structure then depends strongly on system geometry. For this regime, the stability of the conductive state was well established in the 1970s–1980s by Charlson & Sani (1970), Stork & Müller (1975), Buell & Catton (1983). Critical Rayleigh numbers Ra_c are about 2000 for $\Gamma \sim 1$, increasing steeply for lower Γ and decreasing asymptotically towards $Ra_c = 1708$ for $\Gamma \rightarrow \infty$.

Convective state stability

Charlson & Sani (1970) estimated by a numerical variational technique the onset of axisymmetric convection in cylinders of aspect ratios between 0.5 and 8, with insulating and conducting sidewalls. They found the critical Rayleigh numbers ($Ra_c = 2545$ for $\Gamma = 1$, decreasing for higher Γ) and the corresponding number of rolls. They then generalised this analysis (Charlson & Sani, 1971), including non-axisymmetric modes and predicting Ra_c and corresponding critical azimuthal wavenumbers.

Stork & Müller (1975) observed experimentally convective patterns in annuli and cylinders of aspect ratio $0.7 \leq \Gamma \leq 3.2$, varying the sidewall insulation. Their critical Rayleigh numbers were in good agreement with those predicted by Charlson and Sani.

Rosenblat (1982) investigated convective instabilities numerically for free-slip boundary conditions, using a severely truncated expansion in a small number of eigenmodes. He described non-axisymmetric motions existing just above onset for aspect ratios between 0.5 and 2.0.

Finally, Buell & Catton (1983) described how the onset of convection is influenced by the ratio of the fluid conductivity to that of the wall, by performing linear analysis for the aspect ratio range $0 < \Gamma \leq 4$. They determined the critical Rayleigh number and azimuthal wavenumber as a function of both aspect ratio and sidewall conductivity, thus completing the results of the previous investigations, which considered either perfectly insulating or perfectly conducting walls. The flow succeeding the conductive state is three-dimensional over large ranges of aspect ratios, contrary to the expectations of Koschmieder (1993).

Γ	Ra_{c2}	ω_{c2}	m
1.47	24928	± 42.54	3
1.50	24536	± 42.26	3
1.57	23011	± 45.47	4

Table 1.1: Critical Rayleigh numbers Ra_{c2} , frequencies and wavenumbers found by Wanschura, Kuhlmann & Rath (1996) for $Pr = 1$ and different aspect ratios.

Secondary flows

The stability of the first convective state, depending on both aspect ratio and Prandtl number, has been investigated mainly for situations in which the primary flow is axisymmetric. Charlson & Sani (1975) attempted to predict numerically the stability of the primary axisymmetric flow, but the resolution available at that time was inadequate to the task. Müller, Neumann & Weber (1984) investigated convective flows experimentally and theoretically for aspect ratios $0.1 \leq \Gamma \leq 10$. For $\Gamma = 1$ and Prantl numbers 0.02 and 6.7, they observed that the axisymmetric primary flow was stable up to $Ra \sim 10Ra_c$.

Hardin & Sani (1993) calculated weakly nonlinear solutions to the Boussinesq equations for several moderate and small aspect ratios. They found a bifurcation from the axisymmetric state towards a mode with azimuthal wavenumber $m = 2$ for $\Gamma = 1$, $Pr = 6.7$ and $Ra_{c2} = 2430$.

A very complete numerical study of secondary convective instabilities for moderate aspect ratio cylinders and adiabatic sidewalls was performed by Wanschura, Kuhlmann & Rath (1996). They focused on aspect ratios $0.9 < \Gamma < 1.57$, where the primary flow is axisymmetric. They calculated the nonlinear two-dimensional solutions and conducted linear analysis for Prandtl numbers 0.02 and 1. They thus found Ra_{c2} and the azimuthal wavenumbers of corresponding critical eigenvectors.

Touihri, Ben Hadid & Henry (1999) numerically investigated the stability of the conductive state for aspect ratios $\Gamma = 0.5$ and $\Gamma = 1$. They described the main critical modes and established a diagram of primary bifurcations, including unstable branches. For $\Gamma = 1$ they also found a secondary bifurcation point Ra_{c2} , at which the axisymmetric flow becomes unstable towards a two-roll flow and calculated Ra_{c2} for $0 < Pr < 1$.

Hopf bifurcation

Wanschura *et al.* (1996), in their study, predicted the flows succeeding the primary axisymmetric state to be steady, except over a narrow aspect ratio range $1.45 \leq \Gamma \leq 1.57$ at $Pr = 1$. For this configuration they found a Hopf bifurcation. The corresponding eigenvectors had azimuthal wavenumbers $m = 3$ and $m = 4$ (see table 1.1). Thus the secondary flows should be oscillatory, and according to the theory of Hopf bifurcation in systems with this symmetry, should have the form of either standing or travelling waves. As the study was linear, it was not possible to verify which of these two solutions succeeds the axisymmetric flow.

Multiplicity of convective states

Far above the convection threshold, a description in which only one stable state exists, with its form depending only on Rayleigh number, is insufficient. For cylinders with small aspect ratios this was shown by the experimental study carried out by Hof, Lucas & Mullin (1999). Varying the Rayleigh number through different sequences of values, for fixed parameters $\Gamma = 2.0$ and

$Pr = 6.7$, they obtained several different stable patterns for the same final Rayleigh number. For 14 200 they observed two, three and four parallel rolls, a “mercedes” pattern with three spokes of ascending or descending fluid and even an axisymmetric state. They also reported a transition from an axisymmetric steady state towards azimuthal waves.

More recently, convective patterns were investigated by Rüdiger & Feudel (2000), who used a spectral simulation. For aspect ratio $\Gamma = 4$, they found stability ranges of several patterns: parallel rolls, target and spirals. The stability zones had common sections – depending on the initial conditions, different stable flows were observed at the same Rayleigh number.

Leong (2002) used a finite difference method to simulate convective flows for Prandtl number 7 in cylinders of aspect ratios 2 and 4 and adiabatic lateral walls. He observed several steady patterns: parallel rolls, three-spoke flow and axisymmetric state, all of which were stable in the range $6250 \leq Ra \leq 37500$. He also calculated the heat transfer for each pattern.

1.3 Motivation

The first part of our numerical study of Rayleigh–Bénard convection was stimulated by the results of Wanschura 5 Oscillatory states are common in binary fluid convection and in rotating convection, but not as much so in ordinary Rayleigh–Bénard convection, particularly in small aspect ratios. We wished to study in detail this configuration in which an instance of time-periodic Rayleigh–Bénard convection was suggested. Hence we have simulated numerically the loss of stability of the first convective axisymmetric solution undergoing an oscillatory bifurcation for $1.45 \leq \Gamma \leq 1.57$ and $Pr = 1$. In chapter 5 we describe the results of linear stability analysis and nonlinear simulations, which identify the scenario in terms of bifurcation theory in systems with symmetries.

We wished also to explore the multiplicity of stable states reported by Hof *et al.* (1999). This phenomenon is known in other hydrodynamic systems and in large cylinders, but rarely reported for Rayleigh–Bénard convection in cylinders of small aspect ratio. We ran a series of nonlinear simulations for Prandtl number $Pr = 6.7$, aspect ratio $\Gamma = 2.0$ and two types of thermal boundary conditions. Chapter 6 presents the results for perfectly insulating sidewalls and chapter 7 for perfectly conducting sidewalls.

The methods used in our study are described in the three chapters which follow. In chapter 2 we present the nonlinear equations governing the system and we explain the principles of linear analysis. We define also the symmetries characterising the problem and introduce and derive an appropriate representation describing linear and nonlinear dynamics of the system. Chapter 3 describes the most important aspects of the numerical methods used for integrating the differential equations. This comprises discretisation in space and time, imposing boundary conditions and finding the leading eigenvectors and eigenvalues for linearised equations. We also give some details concerning the optimisation of the code and post-processing of the results. The choice of the simulation parameters and some of the tests performed on the code are discussed in chapter 4.

Chapter 2

Governing equations

This chapter introduces the nonlinear Boussinesq equations governing the system and explains the principles of linear analysis. The symmetries of the problem are defined. An appropriate representation of eigenvectors, taking into account the $O(2)$ symmetry, is derived. The theory of Hopf bifurcation in systems with symmetries is evoked, stating that this bifurcation should lead either to standing or to travelling waves.

2.1 Navier–Stokes equations

We consider a fluid confined in a cylinder of depth d and radius R (figure 2.1). The aspect ratio is defined as $\Gamma \equiv R/d$. The fluid has kinematic viscosity ν , density ρ , thermal diffusivity κ and thermal expansion coefficient (at constant pressure) γ . The top and bottom temperatures of the cylinder are kept constant, at $T_0 - \Delta T/2$ and $T_0 + \Delta T/2$, respectively. Using the units d^2/κ , d , κ/d and $\nu\kappa/\gamma gd^3$ for time, distance, velocity and temperature, we obtain the Navier–Stokes and Boussinesq dimensionless equations governing the system

$$Pr^{-1} (\partial_t \mathbf{u} + (\mathbf{u} \cdot \nabla) \mathbf{u}) = -\nabla p + \Delta \mathbf{u} + h \mathbf{e}_z \quad (2.1a)$$

$$\partial_t h + (\mathbf{u} \cdot \nabla) h = Ra u_z + \Delta h \quad (2.1b)$$

$$\nabla \cdot \mathbf{u} = 0. \quad (2.1c)$$

The dimensionless temperature is $T = T_0 Ra / \Delta T - z Ra + h$, where h denotes the dimensionless temperature deviation from the basic vertical profile. The Rayleigh number Ra and the Prandtl

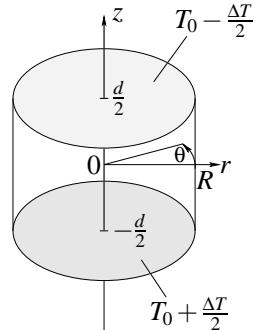


Figure 2.1: Geometry and coordinate system.

number Pr are defined by

$$Ra \equiv \frac{\Delta T g \gamma d^3}{\kappa v}, \quad (2.2)$$

$$Pr \equiv \frac{v}{\kappa}. \quad (2.3)$$

2.2 Boundary conditions

We used realistic boundary conditions for the velocity, with no penetration and no slip on the horizontal plates and sidewalls

$$\mathbf{u} = 0 \quad \text{for } z = \pm 1/2 \quad \text{or } r = \Gamma. \quad (2.4)$$

We assume that perfectly conducting horizontal plates maintain the temperature constant (Dirichlet condition for h)

$$h = 0 \quad \text{for } z = \pm 1/2. \quad (2.5)$$

As for sidewalls, we assume them either also perfectly conducting so that a linear vertical temperature profile is maintained within them and

$$h = 0 \quad \text{for } r = \Gamma, \quad (2.6)$$

or perfectly insulating (Neumann condition)

$$\partial_r h = 0 \quad \text{for } r = \Gamma. \quad (2.7)$$

(The code has also a possibility we have not explored, of mixing these two conditions in order to represent sidewalls with finite values of conductivity: $\mu_{Dir}h + \mu_{Neu}\partial_r h = 0$.)

2.3 Linear analysis

2.3.1 Linearised equations

Understanding convective phenomena is aided by means of linear simulation. When we have a converged stationary solution (\mathbf{U}, H) to the equations (2.1), we can examine its linear stability, i.e. verify whether slight perturbations to it die or lead to evolution towards another state. If we denote the perturbation by (\mathbf{u}, h) and neglect the nonlinear terms of order $(\mathbf{u}, h)^2$, we obtain the set of linearised equations for $(\mathbf{U} + \mathbf{u}, H + h)$

$$Pr^{-1} (\partial_t \mathbf{u} + (\mathbf{U} \cdot \nabla) \mathbf{u} + (\mathbf{u} \cdot \nabla) \mathbf{U}) = -\nabla p + \Delta \mathbf{u} + h \mathbf{e}_z \quad (2.8a)$$

$$\partial_t h + (\mathbf{U} \cdot \nabla) h + (\mathbf{u} \cdot \nabla) H = Ra u_z + \Delta h \quad (2.8b)$$

$$\nabla \cdot \mathbf{u} = 0. \quad (2.8c)$$

Equations (2.8) with the same boundary conditions as those described in § 2.2 can be then integrated in time in the same way as the nonlinear equations (2.1).

2.3.2 Power method

The linear evolution problem (2.8) can be abbreviated by

$$\partial_t \begin{pmatrix} \mathbf{u} \\ h \end{pmatrix} = L \begin{pmatrix} \mathbf{u} \\ h \end{pmatrix}. \quad (2.9)$$

A general solution to this equation is an exponential evolution

$$\begin{pmatrix} \mathbf{u} \\ h \end{pmatrix}(t) = e^{Lt} \begin{pmatrix} \mathbf{u} \\ h \end{pmatrix}(t=0). \quad (2.10)$$

We can decompose the initial condition $(\mathbf{u}, h)(t=0)$ in the basis of eigenvectors of L

$$\begin{pmatrix} \mathbf{u} \\ h \end{pmatrix}(t=0) = \sum_i c_i \phi_i, \quad (2.11)$$

where ϕ_i are eigenvectors and λ_i eigenvalues of L

$$L\phi_i = \lambda_i \phi_i, \quad (2.12)$$

so that

$$e^{Lt} \phi_i = e^{\lambda_i t} \phi_i. \quad (2.13)$$

The evolution equation (2.10) then becomes

$$\begin{pmatrix} \mathbf{u} \\ h \end{pmatrix}(t) = \sum_i e^{\lambda_i t} c_i \phi_i. \quad (2.14)$$

If the solution (\mathbf{U}, H) is stable, every perturbation to it should decrease, so every λ_i should be negative. A transition from parameters for which the solution is stable to parameters for which (\mathbf{U}, H) is unstable corresponds to changing the sign of one of the eigenvalues to positive. Then every component of (\mathbf{u}, h) dies, according to (2.14), except for the critical eigenvector ϕ_c corresponding to the positive eigenvalue λ_c . Therefore, after a long time evolution, we have $(\mathbf{u}, h)(t) \propto \phi_c$, and (2.10) becomes

$$\begin{pmatrix} \mathbf{u} \\ h \end{pmatrix}(t + \Delta t) = e^{\lambda_c \Delta t} \begin{pmatrix} \mathbf{u} \\ h \end{pmatrix}(t). \quad (2.15)$$

If the eigenvalue λ_c is real, we can calculate its value by taking the norm of the equation above

$$\lambda_c = \frac{1}{\Delta t} \log \frac{\left\| \begin{pmatrix} \mathbf{u} \\ h \end{pmatrix}(t + \Delta t) \right\|}{\left\| \begin{pmatrix} \mathbf{u} \\ h \end{pmatrix}(t) \right\|}. \quad (2.16)$$

This is the principle of the *power method*. We do not find the eigenvalues and eigenvectors of L by a direct diagonalisation method for several reasons. First, we do not have the explicit form of the matrix. L , which describes the whole sequence of operations necessary for solving the differential equation, could be obtained via $L(1, 0, 0, 0, \dots)$, then $L(0, 1, 0, 0, \dots)$, etc; but the cost of this procedure in terms of computer time and storage would be too great. Furthermore, direct diagonalisation of the resulting matrix would also be far too costly.

2.3.3 Complex eigenvalues

The time evolution operator L , a real matrix, can have either real eigenvalues or complex conjugate pairs of eigenvalues $\lambda = \sigma \pm i\omega$. The time evolution for a corresponding eigenvector $\phi = \phi^R + i\phi^I$ is

$$e^{Lt} (\phi^R + i\phi^I) = e^{(\sigma+i\omega)t} (\phi^R + i\phi^I), \quad (2.17)$$

or, after decoupling real and imaginary parts,

$$e^{Lt} \phi^R = e^{\sigma t} (\phi^R \cos(\omega t) - \phi^I \sin(\omega t)) \quad (2.18a)$$

$$e^{Lt} \phi^I = e^{\sigma t} (\phi^R \sin(\omega t) + \phi^I \cos(\omega t)). \quad (2.18b)$$

According to (2.18a), evolution from the eigenvector ϕ^R , after a time $t = 3\pi/2\omega$, leads to ϕ^I , while evolution from ϕ^I , after a time $t = \pi/2\omega$, leads to ϕ^R (both scaled by $e^{\sigma t}$). If the time evolution operator has a complex critical eigenvalue, then a perturbation (\mathbf{u}, h) , after sufficiently long time, will be a linear combination of ϕ^R and ϕ^I growing in time like $\exp(\sigma t)$, and oscillating between ϕ^R and ϕ^I with frequency ω .

2.4 Symmetries

2.4.1 Symmetries of Boussinesq equations

Symmetries play an important role in the possible transitions undergone by this system. The Boussinesq equations (2.1) with boundary conditions described in § 2.2, have a \mathbb{Z}_2 symmetry, meaning that they are invariant under reflection with respect to the horizontal midplane. They have also $O(2)$ symmetry, being invariant under reflections with respect to every plane containing the z axis and to rotations about this axis.

2.4.2 \mathbb{Z}_2 symmetry and inverse patterns

The conductive solution also has both $O(2)$ and \mathbb{Z}_2 symmetry. However, the reflection symmetry with respect to the horizontal midplane is broken by the first bifurcation to a convective state. At this moment two solutions appear. For an axisymmetric solution with flow ascending at the axis, there exists a corresponding axisymmetric solution in which the flow descends at the axis; a flow composed of two counter-rotating parallel rolls can have either hot ascending or cold descending fluid on the diameter. For every solution to (2.1), an inverse solution can be deduced using the transformation

$$\begin{pmatrix} u_r \\ u_\theta \\ u_z \\ h \end{pmatrix} (r, \theta, z) \mapsto \begin{pmatrix} u_r \\ u_\theta \\ -u_z \\ -h \end{pmatrix} (r, \theta, -z).$$

We can then refer to patterns and their inverse equivalents, but a distinction between these two groups is not always feasible – for example, inverting a three-roll state will give the same pattern rotated about π . As for a given solution its inverse pattern can be deduced mathematically, we did not seek inverse equivalents of each pattern found, but assumed its existence. In further discussion we will not distinguish between these two families.

2.4.3 $O(2)$ symmetry

If the first convective state consists of axisymmetric convective rolls, then its remaining symmetries are reflection and rotation in θ , which together comprise the symmetry group $O(2)$. The $O(2)$ symmetry is broken by secondary bifurcations with azimuthal wavenumber $m \neq 0$. Bifurcations in the presence of $O(2)$ symmetry were studied and classified during the 1980s by a large number of researchers, e.g. Bajaj (1982); Golubitsky & Stewart (1985); Knobloch (1986); van Gils & Mallet-Paret (1986); Kuznetsov (1998); Coullet & Iooss (1990). We give a brief summary of their results.

If the critical eigenvalue is real, then the resulting bifurcation is a circle pitchfork, leading to a “circle” of steady states parametrised by phase. Each steady state is reflection symmetric in θ (about some value θ_0). If reflection symmetry is broken by a subsequent bifurcation, the scenario is that of a drift pitchfork, leading to slow motion (“drift”) along the circle.

A complex eigenvalue, like that found by Wanschura *et al.* (1996) in the region of $1.45 \leq \Gamma \leq 1.57$, $Ra > 23000$, at $Pr = 1$, leads to a Hopf bifurcation which engenders three nonlinear branches: standing waves, counterclockwise travelling waves, and clockwise travelling waves. The standing waves are reflection-symmetric in θ (again about some value θ_0), while the travelling waves break this symmetry. One of the aims of our study was to determine which of these types of waves is realised by our physical system.

2.4.4 Representations of complex eigenvectors in $O(2)$ symmetry

The linear problem (2.8) for perturbations (\mathbf{u}, h) about an axisymmetric convective state (\mathbf{U}, H) can be divided into decoupled subproblems, each corresponding to a single azimuthal wavenumber m . The problem for wavenumber m can in turn be divided into two identical decoupled subproblems, corresponding to fields of the form

$$\hat{u}_r(r, z) \cos(m\theta), \quad \hat{u}_\theta(r, z) \sin(m\theta), \quad \hat{u}_z(r, z) \cos(m\theta), \quad \hat{h}(r, z) \cos(m\theta), \quad (2.19a)$$

and

$$\hat{u}_r(r, z) \sin(m\theta), \quad \hat{u}_\theta(r, z) \cos(m\theta), \quad \hat{u}_z(r, z) \sin(m\theta), \quad \hat{h}(r, z) \sin(m\theta). \quad (2.19b)$$

The first set describes fields symmetric and the second – antisymmetric about the $\theta = 0$ plane (the u_θ is treated differently, because the antisymmetry of the unit vector $\hat{\mathbf{e}}_\theta$). For simplicity, we will represent each of these types of vector fields by its temperature component $\hat{h}(r, z)$ and leave the dependence on θ and on t to be written explicitly. We may write the linear evolution problem (2.9) restricted to fields with trigonometric dependence on $m\theta$ such as (2.19a)-(2.19b) as

$$\partial_t \hat{h} = \hat{L}_m \hat{h}. \quad (2.20)$$

A real eigenvalue breaking azimuthal symmetry in an $O(2)$ symmetric situation is associated with a two-dimensional eigenspace, consisting of linear combinations of vectors of type (2.19a) and (2.19b). Since

$$\alpha \hat{h}(r, z) \cos(m\theta) + \beta \hat{h}(r, z) \sin(m\theta) = C \hat{h}(r, z) \cos(m(\theta - \theta_0)), \quad (2.21a)$$

where

$$C = \sqrt{\alpha^2 + \beta^2}, \quad m\theta_0 = \text{atan}(\beta/\alpha), \quad (2.21b)$$

all real eigenvectors have m nodal lines and reflection symmetry about some θ_0 . If we take $C \propto \sqrt{Ra - Ra_{c2}}$ and add (2.21a) to the basic axisymmetric state, we obtain the “circle” of steady states resulting from a circle pitchfork described in § 2.4.

A complex eigenvalue in the $O(2)$ symmetric situation is associated with a four-dimensional eigenspace. Within each eigenvector class (2.19a) and (2.19b), the eigenspace is two-dimensional, spanned by two linearly independent eigenvectors \hat{h}^R and \hat{h}^I , which are transformed by \hat{L}_m as

$$\hat{L}_m \begin{pmatrix} \hat{h}^R \\ \hat{h}^I \end{pmatrix} = \begin{pmatrix} \mu & -\omega \\ \omega & \mu \end{pmatrix} \begin{pmatrix} \hat{h}^R \\ \hat{h}^I \end{pmatrix} \quad (2.22)$$

In (2.22), \hat{h}^R can be replaced by any linear combination of \hat{h}^R and \hat{h}^I , but once \hat{h}^R is selected, the choice of \hat{h}^I follows from (2.22). Although the components of equation (2.22) are the real and imaginary parts of the complex equation

$$\hat{L}_m(\hat{h}^R + i\hat{h}^I) = (\mu + i\omega)(\hat{h}^R + i\hat{h}^I), \quad (2.23)$$

the customary designation of \hat{h}^R and \hat{h}^I as the real and the imaginary part of the eigenvector is arbitrary, as reflected by the fact that an eigenvector can be multiplied by any complex number.

To form eigenvectors of the full cylindrical problem belonging to the four-dimensional eigenspace, each of \hat{h}^R and \hat{h}^I is multiplied by a trigonometric function. This yields as a basis for the four-dimensional eigenspace:

$$\hat{h}^R(r, z) \cos(m\theta), \quad (2.24a)$$

$$\hat{h}^I(r, z) \cos(m\theta), \quad (2.24b)$$

$$\hat{h}^R(r, z) \sin(m\theta), \quad (2.24c)$$

$$\hat{h}^I(r, z) \sin(m\theta). \quad (2.24d)$$

One choice for a complex eigenvector pair is (2.24a)-(2.24b), since

$$\hat{L}_m \begin{pmatrix} \hat{h}^R \cos(m\theta) \\ \hat{h}^I \cos(m\theta) \end{pmatrix} = \begin{pmatrix} \mu & -\omega \\ \omega & \mu \end{pmatrix} \begin{pmatrix} \hat{h}^R \cos(m\theta) \\ \hat{h}^I \cos(m\theta) \end{pmatrix} \quad (2.25)$$

Each of $\hat{h}^R(r, z) \cos(m\theta)$ and $\hat{h}^I(r, z) \cos(m\theta)$ has m nodal lines and m axes of reflection symmetry, including $\theta = 0$. More generally, the trigonometric dependence can be taken as in (2.21a), with the same trigonometric dependence for each of \hat{h}^R and \hat{h}^I , to form a complex conjugate eigenvector pair each of whose members has m nodal lines and m axes of reflection symmetry, including $\theta = \theta_0$. The evolution in time under (2.20) for a field with an initial condition of this form is

$$h(r, \theta, z, t) = \alpha e^{i\mu t} [\hat{h}^R(r, z) \cos(\omega t) - \hat{h}^I(r, z) \sin(\omega t)] \cos(m(\theta - \theta_0)). \quad (2.26)$$

The subspace of fields with azimuthal dependence $\cos(m(\theta - \theta_0))$ is invariant under linearised time evolution. (There also exists an invariant subspace under the nonlinear time evolution, which includes harmonics $\cos(km(\theta - \theta_0))$, with the same m axes of reflection symmetry.) If we take $\mu = 0$ and $\alpha \propto \sqrt{Ra - Ra_{c2}}$ in (2.26), and add this to the basic axisymmetric solution, then we obtain to first order the standing wave solution mentioned in § 2.4.

Any combination of (2.24a)-(2.24d) is also a member of a complex eigenvector pair. The calculation

$$\begin{aligned} \hat{L}_m & \begin{pmatrix} \alpha \hat{h}^R(r, z) \cos(m\theta) + \beta \hat{h}^I(r, z) \sin(m\theta) \\ \alpha \hat{h}^I(r, z) \cos(m\theta) - \beta \hat{h}^R(r, z) \sin(m\theta) \end{pmatrix} \\ &= \begin{pmatrix} \mu & -\omega \\ \omega & \mu \end{pmatrix} \begin{pmatrix} \alpha \hat{h}^R(r, z) \cos(m\theta) + \beta \hat{h}^I(r, z) \sin(m\theta) \\ \alpha \hat{h}^I(r, z) \cos(m\theta) - \beta \hat{h}^R(r, z) \sin(m\theta) \end{pmatrix}, \end{aligned} \quad (2.27)$$

when compared with (2.22), shows that the two components of the vector in (2.27) form a complex conjugate pair of eigenvectors for the full cylindrical problem, as in (2.22). Because $\hat{h}^R(r,z)$ and $\hat{h}^I(r,z)$ have different functional forms in (r,z) , these vectors, unlike those of (2.21a), cannot be combined into a single trigonometric function. Neither of the two components of (2.27) has nodal lines or reflection symmetry about any axis if both α and β are non-zero. The evolution in time under (2.20) for a field whose initial condition is the first component of (2.27) is:

$$h(r,\theta,z,t) = e^{\mu t} [\hat{h}^R(r,z)(\alpha \cos(m\theta) \cos(\omega t) - \beta \sin(m\theta) \sin(\omega t)) + \hat{h}^I(r,z)(\alpha \cos(m\theta) \sin(\omega t) + \beta \sin(m\theta) \cos(\omega t))]. \quad (2.28)$$

If $\beta = \pm\alpha$, then (2.28) becomes

$$h(r,\theta,z,t) = e^{\mu t} \alpha [\hat{h}^R(r,z) \cos(m\theta \pm \omega t) + \hat{h}^I(r,z) \sin(m\theta \pm \omega t)], \quad (2.29)$$

where t or θ may be replaced by $(t - t_0)$ or $(\theta - \theta_0)$. If we take $\mu = 0$ and $\alpha \propto \sqrt{Ra - Ra_{c2}}$ in (2.29) and add the basic axisymmetric solution, then we obtain, to first order, the expression for clockwise ($m\theta + \omega t$) or counterclockwise ($m\theta - \omega t$) travelling waves mentioned in § 2.4.

2.5 Amplitude equations and normal form

The linearised evolution treated in the previous section permits any combinations of (2.24a)–(2.24d). The mathematical analysis of Hopf bifurcation in the presence of $O(2)$ symmetry carried out by e.g. Bajaj (1982); Golubitsky & Stewart (1985); Knobloch (1986); van Gils & Mallet-Paret (1986); Kuznetsov (1998) describes the effect of including generic nonlinear terms compatible with the symmetries. Following the formulation of these authors, we decompose the field into a sum of clockwise and counterclockwise travelling waves with complex amplitudes $\zeta_- = \rho_- e^{i\phi_-}$ and $\zeta_+ = \rho_+ e^{i\phi_+}$, respectively. The four variables ρ_\pm, ϕ_\pm form another description of the four-dimensional space described in the previous section. The nonlinear evolution of ζ_\pm near the bifurcation can be described by the following amplitude equations or normal form:

$$\dot{\zeta}_+ = (\mu + i\omega + a|\zeta_-|^2 + b(|\zeta_+|^2 + |\zeta_-|^2)) \zeta_+ \quad (2.30a)$$

$$\dot{\zeta}_- = (\mu + i\omega + a|\zeta_+|^2 + b(|\zeta_+|^2 + |\zeta_-|^2)) \zeta_- \quad (2.30b)$$

Separating (2.30) into equations for real amplitudes $\rho \pm$ and phases $\phi \pm$ leads to

$$\dot{\rho}_+ = (\mu + a_r \rho_-^2 + b_r (\rho_+^2 + \rho_-^2)) \rho_+ \quad (2.31a)$$

$$\dot{\rho}_- = (\mu + a_r \rho_+^2 + b_r (\rho_+^2 + \rho_-^2)) \rho_- \quad (2.31b)$$

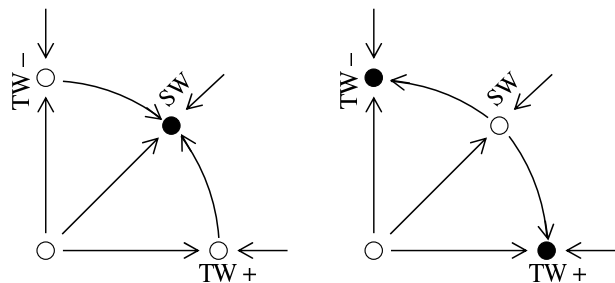
$$\dot{\phi}_+ = \omega + a_i \rho_-^2 + b_i (\rho_+^2 + \rho_-^2) \quad (2.31c)$$

$$\dot{\phi}_- = -\omega - a_i \rho_+^2 - b_i (\rho_+^2 + \rho_-^2). \quad (2.31d)$$

Periodic solutions to (2.31) must be either standing or travelling waves. Solutions to (2.31) and their properties are given in Table 2.1. This table shows that both standing and travelling wave solutions exist for $\mu > 0$ if b_r and $a_r + 2b_r$ are both negative. A positive growth rate from a solution indicates instability. Thus, the stability of the solutions depends on the sign of a_r : if $a_r > 0$, then standing waves are stable and travelling waves unstable, and vice versa for $a_r < 0$. Figure 2.2 shows phase portraits for the amplitudes (ρ_+, ρ_-) , for the cases in which all three branches co-exist and either the standing or the travelling waves are stable.

name	solution	growth rates	frequencies
Base state	$\rho_+ = \rho_- = 0$	μ, μ	
Counterclockwise wave	$\rho_+ = \sqrt{\frac{-\mu}{b_r}}, \rho_- = 0$	$-2\mu, -\frac{a_r}{b_r}\mu$	$\omega - \frac{b_i}{b_r}\mu$
Clockwise wave	$\rho_- = \sqrt{\frac{-\mu}{b_r}}, \rho_+ = 0$	$-2\mu, -\frac{a_r}{b_r}\mu$	$-(\omega - \frac{b_i}{b_r}\mu)$
Standing wave	$\rho_+ = \rho_- = \sqrt{\frac{-\mu}{a_r + 2b_r}}$	$-2\mu, \frac{2a_r}{a_r + 2b_r}\mu$	$\pm(\omega - \frac{a_i + 2b_i}{a_r + 2b_r}\mu)$

Table 2.1: Solutions to (2.31) and their properties.

Figure 2.2: Phase diagram illustrating stability of standing waves (left) or travelling waves (right). The axes represent amplitudes of counterclockwise and clockwise travelling waves ρ_+ and ρ_- . Standing waves can be constructed as an equal superposition of the two.

Chapter 3

Numerical integration

In this chapter a rough description of the code is given. The algorithm was implemented by Tuckerman in the 1980s and a detailed description of all techniques used can be found in (Tuckerman, 1989). The task undertaken at the beginning of this project was optimising the program for a vector platform, building in the Arnoldi procedure, finding resolutions appropriate for three-dimensional cases, and developing postprocessing and visualisation tools. We also improved the user interface and created basic documentation.

3.1 Spectral discretisation – Galerkin projection

3.1.1 Galerkin decomposition

We used a pseudospectral method to integrate the equations (Gottlieb & Orszag, 1977). This is based on representing every field as a truncated sum of functions, usually polynomials or others having known derivatives and good numerical properties. This technique is called Galerkin projection and the basis functions are often referred to as spectral modes. The vectors of coefficients coming from spectral projection belong to what is called *spectral space*, while the vector of values of fields evaluated on the gridpoints belong to *physical space*. A method is pseudospectral if a part of the calculation is performed in the physical space. This is the case of our method – we evaluate the linear (diffusive) terms in spectral space and the nonlinear (advection) terms in physical space (the latter is less expensive than calculating the convolution of the spectral coefficients).

3.1.2 Fourier series in θ

In the azimuthal direction a Fourier series is used, which is appropriate for representing periodic fields. For any field $f(\theta)$, this projection gives the approximation

$$f(\theta) \approx \sum_{m=-M}^M \hat{f}_m e^{im\theta}, \quad (3.1)$$

where the coefficients \hat{f}_m are complex. The properties of the Fourier transform of a real function $f(\theta)$ require that

$$\hat{f}_m = \overline{\hat{f}_{-m}}.$$

Thus we use only $m \geq 0$. A property of Fourier representation, very useful from the numerical point of view, is that the differentiation formula consists only of multiplication by im in the

spectral space

$$\partial_\theta \hat{f} e^{im\theta} = im \hat{f} e^{im\theta},$$

which means that every operator ∂_θ^n is a diagonal matrix.

3.1.3 Chebyshev polynomials in z

We used Chebyshev polynomials for decomposition of the fields in the vertical direction. A Chebyshev polynomial of order k is defined by the formula

$$T_k(x) = \cos(k \arccos(x)), \quad (3.2)$$

which can be transformed, using trigonometric identities, into a recursive explicit polynomial form. Chebyshev polynomials have a number of desirable approximation properties (Press *et al.*, 1997). They form an orthogonal basis on the interval $[-1, 1]$, with the scalar product defined discretely as a sum of products of values in the collocation points; and continuously as an integral over $[-1, 1]$ with a weight $(1 - x^2)^{-1/2}$. If we want to approximate a function $f(x)$ by

$$f(x) \approx \sum_{k=0}^K c_k T_k(x), \quad (3.3)$$

the coefficients c_k of the expansion can be calculated by inverting $f(x_j) = \sum_k c_k T_k(x_j)$. Using an expansion in Chebyshev polynomials implies using Chebyshev collocation points, which are more densely spaced near the boundaries -1 and 1 . Two types of collocation grids can be used: the zeros or the extrema of the highest polynomial T_K , both sets of $K + 1$ points. The zeros are given by the formula

$$x_k = \cos\left(\frac{\pi(k + \frac{1}{2})}{K}\right), \quad k = 0, \dots, K,$$

and called Gauss-Radau quadrature, while the extrema, called Gauss-Lobatto collocation points, are

$$x_k = \cos\left(\frac{\pi k}{K}\right), \quad k = 0, \dots, K.$$

In addition, if we know the coefficients c_k of the expansion of $f(x)$, we can calculate the coefficients c'_k of its derivative $f'(x)$.

We used a Gauss-Lobatto grid, which includes the boundary points. Since after nondimensionalising we have $z \in [-0.5, 0.5]$, the Chebyshev representation for the vertical direction takes the form

$$f(z) \approx \sum_{k=0}^K \hat{f}_k T_k(2z). \quad (3.4)$$

3.1.4 Chebyshev polynomials in r

We also used Chebyshev polynomials and a Gauss-Lobatto grid in the radial direction r . As r varies from 0 to Γ , our approximation formula is

$$f(r) \approx \sum_{k=0}^K \hat{f}_k T_k(r/\Gamma) \quad (3.5)$$

and we are interested only in the positive parts of the Chebyshev polynomials. However, when coupling the trigonometric representation in θ with the Chebyshev polynomials in r , a problem

of singularity at the vertical axis can appear, due to gluing the part $f(r, \theta)$ with $f(r, \theta + \pi)$. These terms should match smoothly, having the same values and derivatives. Also, at $r = 0$, the function should have the same values for every θ , $f(r = 0, \theta) = \text{const}$. A representation which does not contain the singular components can be created by introducing parity restrictions for the Chebyshev and Fourier functions (Tuckerman, 1989). Scalar fields and the vertical velocity are then approximated by the formula

$$f(r, \theta, z) = \sum_{m=-M}^M \sum_{\substack{j \geq m \\ j+m \text{ even}}}^J \sum_{k=0}^K \hat{f}_{j,m,k} T_j(r/\Gamma) T_k(2z) e^{im\theta} \quad (3.6)$$

and for the fields u_r and u_θ the same representation is used, except that the condition $j + m$ odd is required. In the code, less strict parity rules are used, ensuring only that the first three derivatives of f are continuous at the cylinder axis.

3.2 Time discretisation

In order to discretise the time dependence, we use a mixed semi-implicit second-order scheme. The nonlinear (advective) terms and buoyancy term $h\hat{\mathbf{e}}_z$ are calculated in physical space and integrated via the Adams–Bashforth explicit formula, while the linear (diffusive) terms are calculated in spectral space and integrated via the implicit Crank–Nicolson scheme. Both formulas approximate the problem

$$\frac{df}{dt} = g \quad (3.7)$$

over a time interval $[t, t + \Delta t] \mapsto [t^n, t^{n+1}]$, evaluating the value of g at the midpoint $t^{n+1/2}$ with second-order precision. The Crank–Nicolson method approximates equation (3.7) as

$$\frac{f^{n+1} - f^n}{\Delta t} = \frac{1}{2} (g^n + g^{n+1}) \quad (3.8)$$

and Adams–Bashforth as

$$\frac{f^{n+1} - f^n}{\Delta t} = \frac{3}{2} g^n - \frac{1}{2} g^{n-1}. \quad (3.9)$$

Applying these formulas to the equations (2.1a)–(2.1b), we obtain the following time-stepping scheme

$$\begin{aligned} \left(\frac{\mathbb{I}}{Pr} - \frac{\Delta t}{2} \Delta \right) \mathbf{u}^{n+1} + \Delta t p^{n+1} &= \frac{\Delta t}{2Pr} [-3(\mathbf{u}^n \cdot \nabla) \mathbf{u}^n + (\mathbf{u}^{n-1} \cdot \nabla) \mathbf{u}^{n-1}] \\ &\quad + \left(\frac{\mathbb{I}}{Pr} + \frac{\Delta t}{2} \Delta \right) \mathbf{u}^n + \frac{\Delta t}{2} [(3h^n - h^{n-1}) \mathbf{e}_z] \end{aligned} \quad (3.10a)$$

$$\begin{aligned} \left(\mathbb{I} - \frac{\Delta t}{2} \Delta \right) h^{n+1} &= \frac{\Delta t}{2} (-3(\mathbf{u}^n \cdot \nabla) h^n + (\mathbf{u}^{n-1} \cdot \nabla) h^{n-1}) \\ &\quad + Ra \frac{\Delta t}{2} (u_z^{n+1} + u_z^n) + \left(\mathbb{I} + \frac{\Delta t}{2} \Delta \right) h^n. \end{aligned} \quad (3.10b)$$

where \mathbb{I} is the identity operator.

3.3 Influence matrix

3.3.1 Tau method

The equations (3.10), together with (2.1c) are linear and can be represented in the spectral space in a matrix form. However, they do not take into account the boundary conditions. Consider a function $f(x)$ approximated by any spectral series of basis functions T_k

$$f(x) = \sum_{n=0}^N \hat{f}_n T_n(x).$$

For a boundary point x_b we can express a boundary condition $f(x_b) = f_b$ by

$$f_b = \sum_{n=0}^N \hat{f}_n T_n(x_b).$$

Note that b indexes the boundary points, varying from 1 to B . We can then replace one row of the linear operator by the values given by this condition, thus sacrificing the accuracy of the solution. This can be done for the last spectral components, which are also the least significant. This procedure, called the *tau method*, gives us a solution which satisfies the boundary conditions.

3.3.2 Velocity–pressure decoupling

In equation (3.10a), velocity and pressure are coupled. In order to decouple these fields, we can apply to both sides of the equation the divergence operator ($\nabla \cdot$). This operator commutes with the laplacian operator Δ , and therefore terms $\nabla \cdot \mathbf{u}$ appear, for example

$$\nabla \cdot \left(\frac{\mathbb{I}}{Pr} - \frac{\Delta t}{2} \Delta \right) \mathbf{u} = \left(\frac{\mathbb{I}}{Pr} - \frac{\Delta t}{2} \Delta \right) \nabla \cdot \mathbf{u}.$$

These terms can then be dropped because of the incompressibility equation $\nabla \cdot \mathbf{u} = 0$ stated in (2.1c). In this way we obtain a Poisson equation for the pressure

$$\Delta p = rhs, \quad (3.11)$$

where *rhs* denotes all the terms remaining in the right-hand side, which are to be evaluated at times t^n and t^{n-1} .

3.3.3 Influence matrix

Now the difficulty lies in the boundary conditions for the pressure. These are defined indirectly: we must find the pressure field for which the velocity field will have null divergence ($\nabla \cdot \mathbf{u} = 0$) on the boundaries. This cannot be done by the tau method, so we use a discrete equivalent of the Green functions method for solving Poisson equations with boundary conditions, called the *influence matrix* method. We give here only a rough description of this complex procedure.

The influence matrix method is based on two principles: the uniqueness of the solution to a Poisson equation with boundary conditions and the decomposition of the solution into a homogeneous and particular part. Let us write the pressure p as

$$p = p^H + p^P,$$

where p^H denotes the homogeneous pressure, i.e. a solution to the Laplace equation

$$\Delta p^H = 0. \quad (3.12)$$

The pressure p^P is a particular solution to (3.11), time dependent, with simple (zero) boundary conditions. We assume that the velocity can then also be represented as a sum of two terms, obtained with p^H and p^P , respectively,

$$(\mathbf{u}, p) = (\mathbf{u}, p)^H + (\mathbf{u}, p)^P. \quad (3.13)$$

The boundary conditions are still defined indirectly for the homogeneous pressure p^H , which should ensure that

$$\nabla \cdot \mathbf{u}^P + \nabla \cdot \mathbf{u}^H = 0. \quad (3.14)$$

Zero boundary conditions for p^P permit us to solve (3.11) for the particular solution $(\mathbf{u}, p)^P$, after which (3.14) becomes

$$\nabla \cdot \mathbf{u}^H = -\nabla \cdot \mathbf{u}^P, \quad (3.15)$$

or

$$\text{Div}_{Bdy} \begin{pmatrix} \mathbf{u} \\ p \end{pmatrix}^H = -\text{Div}_{Bdy} \begin{pmatrix} \mathbf{u} \\ p \end{pmatrix}^P, \quad (3.16)$$

where Div_{Bdy} denotes an operator returning the value of the divergence of \mathbf{u} on the boundaries.

We construct the homogeneous solution $(\mathbf{u}, p)^H$ in the following way. For each of B boundary points x_b , we find a pressure solution p_b^H , which satisfies (3.12) and is zero at each boundary point $x_{b'}$ except for the point x_b , i.e.

$$p_b^H(x_{b'}) = \delta_{b,b'}. \quad (3.17)$$

We then solve the equations for the velocity \mathbf{u}_b^H as follows. Let $V_b \equiv (\mathbf{u}_b, p_b)^H$. For B boundary points, we obtain B solutions V_b , each satisfying (3.17) for a different value of b . We can represent the homogeneous solution $(\mathbf{u}, p)^H$ as a weighted sum of functions V_b

$$\begin{pmatrix} \mathbf{u} \\ p \end{pmatrix}^H = \underbrace{\begin{pmatrix} V_1 & \cdots & V_B \end{pmatrix}}_{\equiv D} \begin{pmatrix} C \end{pmatrix}, \quad (3.18)$$

with vector C containing the weights. The boundary condition (3.16) then becomes

$$\underbrace{\text{Div}_{Bdy} \begin{pmatrix} V_1 & \cdots & V_B \end{pmatrix}}_{\equiv D} \begin{pmatrix} C \end{pmatrix} = -\text{Div}_{Bdy} \begin{pmatrix} \mathbf{u} \\ p \end{pmatrix}^P. \quad (3.19)$$

(influence matrix)

The *influence matrix* is defined to be the product of the operator Div_{Bdy} and the matrix containing the entire set of vectors V_b . Denoting the influence matrix by D , we can rewrite (3.19) in a more compact form

$$DC = -\text{Div}_{Bdy} \begin{pmatrix} \mathbf{u} \\ p \end{pmatrix}^P. \quad (3.20)$$

The coefficients C can then be obtained by inverting the influence matrix

$$C = -D^{-1} \text{Div}_{Bdy} \begin{pmatrix} \mathbf{u} \\ p \end{pmatrix}^P. \quad (3.21)$$

As the vectors V_b and the matrix D are time-independent, we calculate them and invert the influence matrix once at the beginning of the simulation. Then, during each time step, after calculating the particular solution term $(\mathbf{u}, p)^P$, we can find the coefficients C from (3.21) and then the homogeneous term from (3.18).

Storing all of the B functions V_b during the entire simulation is expensive, as each of them has dimension equal to the number of gridpoints in the whole volume. We can, however, calculate them in a preprocessing step, and store only D^{-1} , as, according to the definition of p_b^H , the coefficients C are the values of p^H at the boundaries x_b . As these values are the same for the total pressure p (since $p^P = 0$ at the boundaries), we can solve the original problem (3.11) and (3.10) and obtain directly the complete solution (\mathbf{u}, p) , instead of calculating the homogeneous part.

We summarise the procedure. We calculate once, in the beginning, the set of B homogeneous solutions V_b . We then construct the influence matrix, containing the divergence of velocity for each V_b at each boundary point; we calculate D^{-1} and abandon V_b and D . During every timestep, we calculate the particular solution $(\mathbf{u}, p)^P$ on the boundaries, its divergence at the boundaries, the coefficients C and finally the whole solution (\mathbf{u}, p) with the pressure given by C .

In the pseudospectral code we used, each Fourier mode m is decoupled from the other Fourier modes, which makes the size of the influence matrix reasonable. Many other manipulations are performed before implementing the code. The influence matrix is not invertible, and so must be regularised. The matrices representing differential operations, which are used at each time iteration, can be reduced to block matrices or banded matrices in order to use optimised multiplication algorithms. All the procedures and methods used by the code are described in detail in Tuckerman (1989).

3.3.4 Tau correction

Acting on the equations with the operator $(\nabla \cdot)$, described in § 3.3.2, propagates the inaccuracy in the last coefficient resulting from the tau method. Losing the last mode, we lose also its derivatives, which contain lower frequencies. This can lead to high oscillations in the physical solution and, in some cases, influence the results significantly (Canuto *et al.*, 1988). In order to improve the accuracy of the tau method, a remedy, called the *tau correction*, can be applied. In this method the trace of the derivatives of the dropped frequencies is kept in the equations, and, once the solution is obtained, the necessary correction is applied to it. In the code, the tau correction is implemented, together with the boundary conditions, in the influence matrix.

3.4 Linear simulation

3.4.1 Power method

The power method, described in § 2.3.2, is not appropriate for situations where the critical eigenvalues are complex, or degenerate, or too close to each other. In addition it gives only one eigenvalue. However, since in linear simulation about an axisymmetric state there is no coupling between Fourier frequencies in the azimuthal direction, every mode evolves separately,

and for each of them we obtain one eigenvector. We identify the critical eigenvector by determining which eigenvalue first becomes positive as the Rayleigh number is increased. This type of calculation is inexpensive numerically: there is no coupling of Fourier frequencies, so the simulation also can run separately for each mode. For small aspect ratios, we expect the critical eigenvector to have small wavenumber and so there is no need to check a large number of azimuthal modes. In addition, when perturbing about the conductive state $(\mathbf{U}, H) = 0$, all terms containing \mathbf{U} and H disappear. This is why the stability of the conductive state could be examined numerically already in the 1980s, while the secondary instabilities are still subject to investigation.

3.4.2 Arnoldi–Krylov method

An indirect diagonalisation method which does not have the limits of the power method is the *Arnoldi–Krylov* procedure, which extracts the leading real or complex eigenvalues (those of largest real part) and corresponding eigenvectors. We postprocess the results of integrating (2.8) by an *Arnoldi decomposition* as follows. A small number of fields

$$\begin{pmatrix} \mathbf{u} \\ h \end{pmatrix}(0), \begin{pmatrix} \mathbf{u} \\ h \end{pmatrix}(T), \begin{pmatrix} \mathbf{u} \\ h \end{pmatrix}(2T), \dots, \begin{pmatrix} \mathbf{u} \\ h \end{pmatrix}((K-1)T), \quad (3.22)$$

obtained respectively at times $0, T, 2T, 3T, \dots, KT$, are calculated and orthonormalised to one another to generate a set of vectors $v_1, v_2, v_3, \dots, v_K$ which form a basis for the K -dimensional *Krylov space*. The action of the operator on the Krylov space is represented by a *Hessenberg matrix*, whose elements are $\langle v_j, e^{LT} v_k \rangle$. This small matrix is directly diagonalised. Its eigenvalues approximate eigenvalues λ of e^{LT} , while its eigenvectors consist of coefficients of the vectors v_j , to be combined and normalised to form approximate eigenvectors ϕ of e^{LT} . The accuracy of these approximate eigenpairs is measured by the residue $\|e^{Lt}\phi - \lambda\phi\|$ in the case of real eigenvalues or by the residues $\|e^{Lt}\phi^R - (\lambda^R\phi^R - \lambda^I\phi^I)\|, \|e^{Lt}\phi^I - (\lambda^R\phi^I + \lambda^I\phi^R)\|$ in the case of complex eigenvalues. If the desired eigenvalues have sufficiently small residues, they are accepted; otherwise we continue integration of (2.8), replacing (3.22) by

$$\begin{pmatrix} \mathbf{u} \\ h \end{pmatrix}(T), \begin{pmatrix} \mathbf{u} \\ h \end{pmatrix}(2T), \begin{pmatrix} \mathbf{u} \\ h \end{pmatrix}(3T), \dots, \begin{pmatrix} \mathbf{u} \\ h \end{pmatrix}(KT) \quad (3.23)$$

and so on, until the residue is below the acceptance criterion.

3.4.3 Calculating the base state

Before simulating the linearised equations, we must know the steady base state (\mathbf{U}, H) about which to perturb. To calculate a non-trivial base solution, we run a nonlinear simulation, in which the fields evolve in time towards a stationary flow. As, in order to reproduce the results of Wanschura *et al.* (1996), we needed an axisymmetric base state, we run the nonlinear simulations using only the axisymmetric Fourier mode, $m = 0$.

3.5 Code vectorisation

We optimised the code for a vector supercomputer NEC SX-5. The principle of vector architecture is performing operations rather on a group (vector) of data instead of every separate piece of data. For each such global operation, a *pipeline* is first constructed, i.e. the operations to be

	before	after
performance in MFLOPS	35	516
vectorisation ratio in %	32	95
time in seconds CPU per 100 iterations	11	0.7

Table 3.1: Performance of the code before and after optimisation (for a resolution $N_r = 15$, $N_z = 9, N_\theta = 9$).

performed are defined and the input and output data vectors are prepared. Then the computation is started and, after an initialisation time, once per processor tick a calculated piece of data leaves the pipeline. For long vectors, where the time to prepare the pipeline is much smaller than the time to use it, we then obtain approximately one complete operation per processor clock tick. This is much more efficient than computations in a non-vector processor, where an equivalent operation takes several ticks. In contrast, every scalar (non-vectorised) operation is much slower on a vector platform, as the clock frequency of such a processor is relatively low.

Vectorisation of a source code is supposed to be done by the compiler, which looks for sequences where the same operation is to be performed on a large amount of data. Usually the loops are well vectorised if the data is to be accessed sequentially, one piece after another or with a skip, but problems arise when the same piece of data is to be accessed more than once. A memory access conflict can then appear, which inhibits efficient vectorisation. Such problems must be solved manually, by changing, if possible, the order of operations inside the loop.

Another problem is overly aggressive optimisation and vectorisation. Aggressive optimisation is a problem of every compiler since, in order to accelerate the execution, the compiler makes some assumptions on the data, reorganises it and changes the order of operations. If some of the assumptions are false, the program can return incorrect results. On a vector platform an analogous problem is vectorisation, for which false assumptions can lead to side effects and influence the results. In addition, incorrect optimisation and vectorisation can slow down the program instead of accelerating it. For these reasons the compilation options of optimisation/vectorisation should be carefully chosen.

We optimised the simulation code in the following way. First we ran the code compiled without any optimisation (debug mode). We considered the fields obtained as a correct solution. Then we tried various optimisation and vectorisation options for each source file, checking whether it changed the results. While comparing the results, we tolerated a certain error, recalling that for a finite precision computation, every change of order of operations, even permitted mathematically and necessary for good optimisation, can induce slight differences: numerically we often have $a + (b + c) \neq (a + b) + c$.

The next step was using a profiling tool (PsuitePerf on the NEC SX). This provided performance statistics for every subroutine: CPU time, degree of vectorisation, memory conflicts, call count and others. This permitted us to find the most expensive subroutines. If these were called many times and not well vectorised, we tried changing the optimisation degree, or, if this was not feasible, we tried reorganising the loop order. For standard operations, like matrix multiplication or fast Fourier transforms, we replaced the original subroutines by versions optimised for the vector platform.

All these methods permitted us to accelerate the code by a factor of about 15. On the NEC SX-5, for a resolution $35 \times 39 \times 17$ we achieve over 15 iterations per CPU second. The performance of the code is then 1.4 GFLOPS (giga floating-point operations per second). The characteristics of the code before and after optimising it are given at the table 3.1. The performance grows with the resolution, as the ratio of vector operations is 99%.

During the optimisation manipulations, we strove to keep the code portable, introducing preprocessor directives for the machine-dependent fragments of code. We also compiled the program under a PC, without seeking to optimise it. While it was impossible to run three-dimensional nonlinear simulations on a PC computer (because of the higher azimuthal resolution required) we were able to use a PC Athlon 2000+ for running linear simulations.

3.6 Program output

During each simulation, we saved, over short time intervals, the value of h at two fixed points inside the cylinder. This permitted us to quickly check whether the solution was converged. Another quantity systematically saved was the total energy, defined here as

$$E \equiv \frac{1}{Ra} \left(\frac{\langle \mathbf{u}, \mathbf{u} \rangle}{Pr} + \frac{\langle h, h \rangle}{Ra} \right). \quad (3.24)$$

We calculated and saved its values separately for each azimuthal mode. We also saved several spectral fields (\mathbf{u}, h) for different time instants, and thus kept a complete trace of the time evolution of the system. This permitted us to perform post-processing statistics, visualise the fields and reuse them as initial conditions for other runs.

3.7 Visualisation

Our post-processing program transformed the binary files with spectral fields into files in a given visualisation format (AVS/Tecplot/VTK). In this document we show mainly the visualisations of the field h in the midplane of the cylinder. Dark areas indicate hot zones and bright areas indicate cold zones, which correspond to ascending and descending flow, respectively, and therefore gives an idea of the shape of convective rolls.

Chapter 4

Code validation

In order to establish that the code works correctly, we performed several tests, verifying spectral and temporal convergence and reproducing some results already published. We present a few of these tests, especially those which justify the choice of resolution.

4.1 Choice of resolution

Choosing a sufficient spatial resolution is not an easy task, since it depends on the pattern and we do not know *a priori* how the initial field will evolve. We should avoid deforming the grid too much, i.e. the three dimensions of a grid cell should be approximately the same (except possibly at the boundaries, where higher resolution is needed). On the other hand, large resolution is computationally expensive, so reducing the grid size in any direction can be an important and necessary optimisation. A general rule we followed was finding a grid compromising between these two requirements and adding a certain security margin to its dimensions.

The number of gridpoints is determined by the highest order of functions used for the approximation. According to (3.6), a combination $N_r \times N_\theta \times N_z$ means the number of gridpoints $(N_r + 1) \times 2(N_\theta + 1) \times (N_z + 1)$. The Chebyshev collocation points are not regularly spaced, so we will always have non-square elements in the r - z plane; however, for a cylinder of a given aspect ratio $\Gamma = R/d$, we should have approximately

$$N_r/N_z = \Gamma.$$

As for the azimuthal direction we have $2(N_\theta + 1)$ points on the circumference, this gives

$$N_\theta/N_r = \pi.$$

Therefore, for $\Gamma \approx 1.5$, a non-deformed mesh $N_r \times N_\theta \times N_z$ would be, for example, $15 \times 35 \times 10$ or $30 \times 70 \times 20$. We were especially interested in reducing the ratio N_θ/N_z .

If the grid is too deformed or the resolution is insufficient, the fields start oscillating in time and the evolution diverges. An example of this behaviour is given on figure 4.1, where time evolution of a spectral mode $\hat{h}_{0,0,1}$ is displayed for different resolutions. As we increase the resolution, numerical oscillations disappear, but the results can still depend quantitatively on the resolution. Figure 4.2 shows such dependence for a situation in which the spatial convergence in the z direction has been attained – for slight changes of resolution the values differ only about 0.1%.

While watching the evolution of one quantity can already inspire confidence in the resolution used, there exists a more appropriate test for spectral simulations. We can choose a direction,

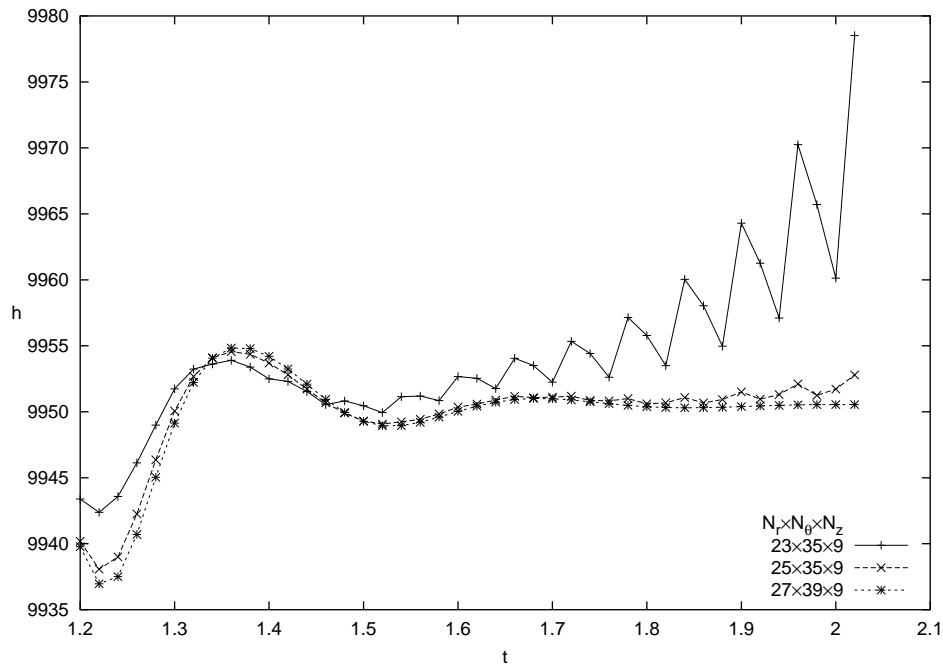


Figure 4.1: Evolution of temperature at $r = 0.7$, $z = 0.3$, $\theta = 0$ for different spatial resolutions ($Ra = 25\,000$, $\Gamma = 1.47$).

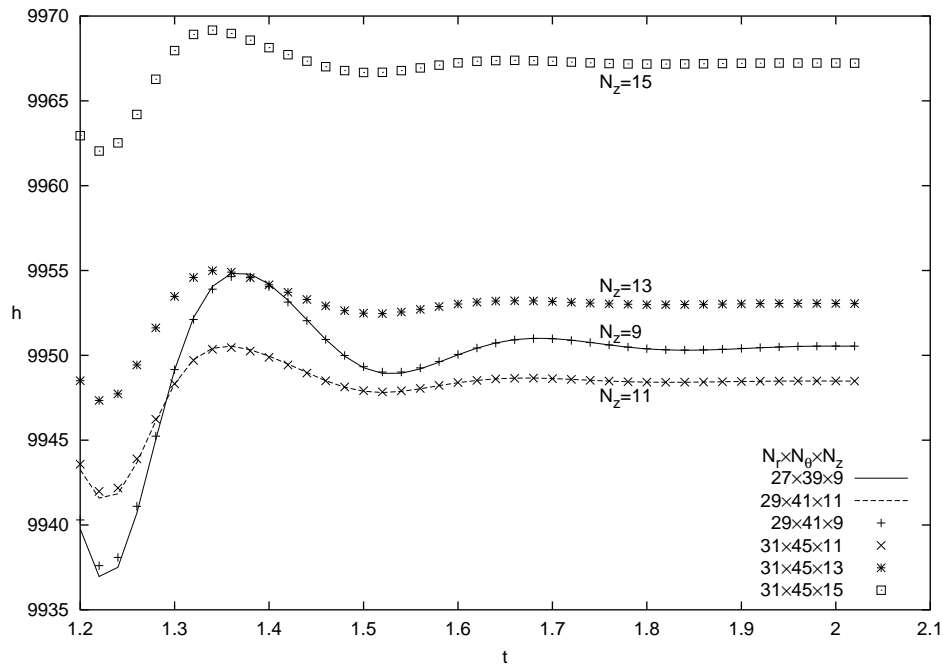


Figure 4.2: Evolution of temperature at $r = 0.7$, $z = 0.3$, $\theta = 0$ for different spatial resolutions ($Ra = 25\,000$, $\Gamma = 1.47$).

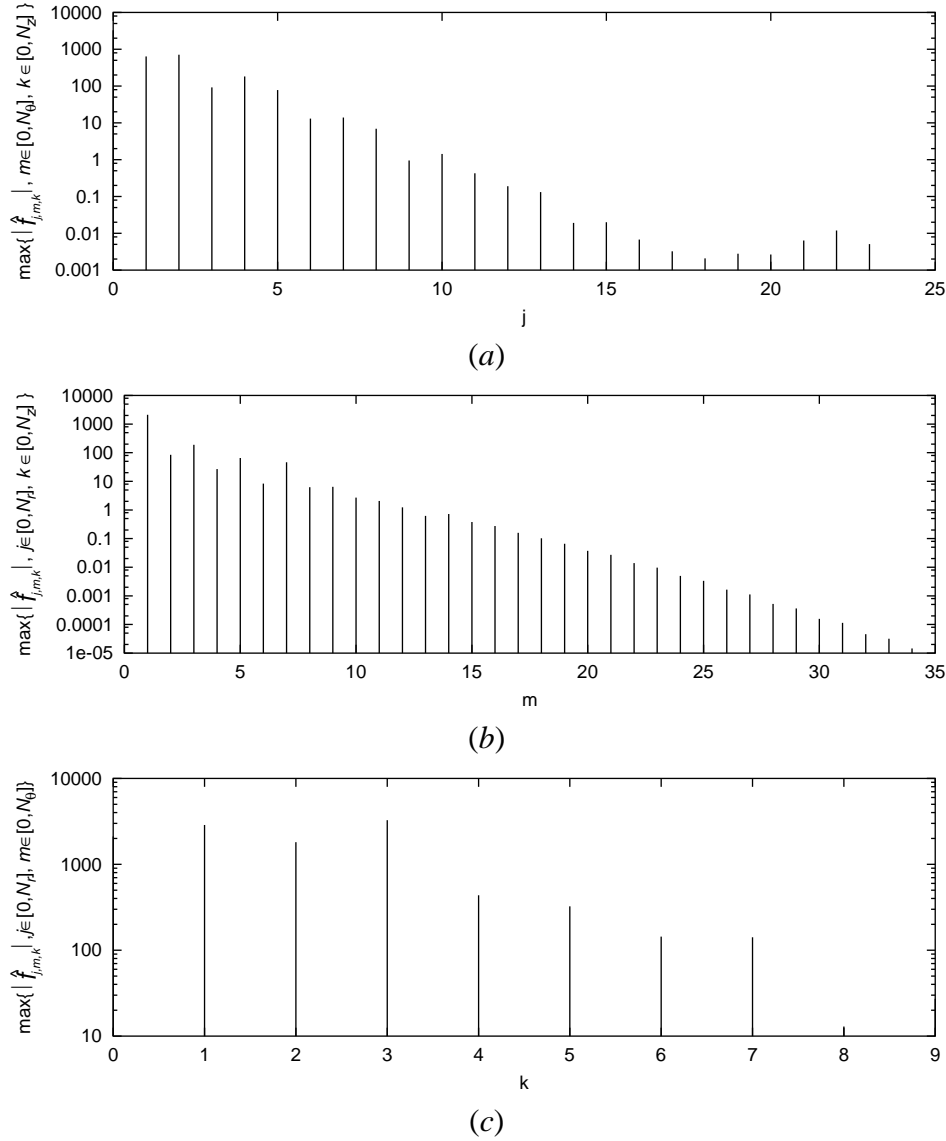


Figure 4.3: Resolution $23 \times 35 \times 9$ for $\Gamma = 1.47$: maxima of spectral coefficients as a function of one direction, for: (a) r , (b) θ , (c) z .

and monitor the maximal spectral coefficients for every spectral mode in this direction, e.g. for r we would look at $(h_k)_{max} = \max \{ h_{k,j,m}, 0 \leq j \leq N_z, 0 \leq m \leq 2N_\theta \}$ for every $k \in [0, N_r]$. These should descend exponentially as i is increased. We show two examples of such a spectrum: figure 4.3 shows a distribution for an obviously insufficient resolution in the r direction – there is a Gaussian peak at the high-frequencies area; the number of points in the vertical direction seems also insufficient. Figure 4.4 shows an example of a good resolution – in all directions the coefficients decrease exponentially.

In order to choose our resolution we did a series of runs at a rather high Rayleigh number, with the same configuration and a timestep 2×10^{-4} , varying only $N_r \times N_\theta \times N_z$, and we compared the evolution of several quantities, like temperature and velocity at certain points in physical space, several spectral coefficients and the total energy. We decided that a good compromise between the accuracy and efficiency would be:

- for $\Gamma \approx 1.5$: $35 \times 39 \times 17$

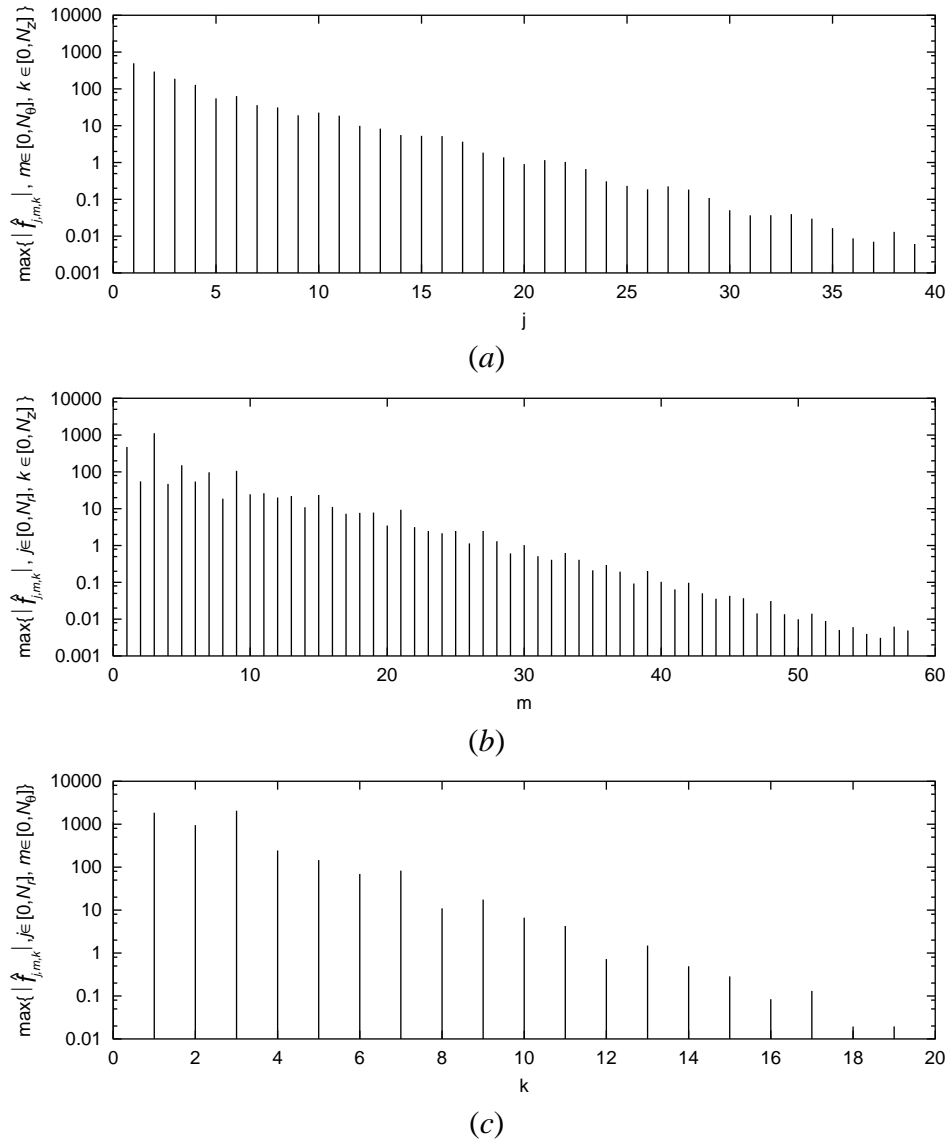


Figure 4.4: Resolution $39 \times 59 \times 19$ for $\Gamma = 2$: maxima of spectral coefficients as a function of coefficient index in the direction: (a) r , (b) θ , (c) z .

- for $\Gamma = 2$: $39 \times 59 \times 19$.

When we had any doubts concerning the resulting pattern, we ran a simulation with more refined mesh. However, each such test only confirmed the results obtained with the previous resolution.

4.2 Choice of timestep

The choice of the timestep Δt depends on Rayleigh number and on the evolution of the system. For higher Rayleigh numbers and abrupt transitions, a smaller timestep is required. For slowly evolving fields, the number of iterations necessary for convergence becomes too great, unless we use larger Δt . We chose the initial timesteps as a function of Rayleigh number and if the evolution slowed down, we continued the simulation with an increased Δt . The timesteps we used varied from $\Delta t = 2 \times 10^{-4}$ for $Ra = 30000$ to $\Delta t = 8 \times 10^{-4}$ for $Ra = 2000$. We refined it in case of any doubt, especially when any oscillations appeared.

4.3 Choice of parameters for linear runs

After integrating the axisymmetric version of the nonlinear equations (2.1) at a given Rayleigh number to create the nonlinear axisymmetric solution (\mathbf{U}, H) , we integrated the non-axisymmetric linearised equations (2.8) to evolve (\mathbf{u}, h) from an arbitrary initial condition. As there is no coupling between the Fourier modes in these linearised equations, the resolution in the azimuthal direction can be coarser than the resolution in r and z . In addition, for small aspect ratio (here $\Gamma \approx 1.5$), we can expect the leading eigenvectors to lie in lower frequencies. Therefore we usually used no more than ten azimuthal modes. Figure 4.5 shows the real part of the leading eigenvalue as a function of timestep, for simulations for three different $r-z$ resolutions: 23×17 , 35×19 and 47×29 . There is no visible difference between the results for the two higher resolutions. There is, however, a visible influence of timestep. We chose a small timestep $\Delta t = 10^{-4}$. It is also possible to obtain more precise eigenvalues by *Richardson extrapolation* for $\Delta t \rightarrow 0$. The spatial resolution we used was $N_r = 47, N_z = 29$ for each azimuthal mode. To construct the Krylov space (3.22) and approximate eigenpairs, we used $K = 10$ vectors, a time interval of $T = 100\Delta t = 10^{-2}$, and an acceptance criterion of 10^{-5} .

4.4 Convergence criteria

In nonlinear simulation, we can define a state as stable if it no longer evolves in time, or, for a time-dependent state, if its amplitude and frequency do not evolve. We monitored the flow structure, its energy and the evolution of the azimuthal velocity at two arbitrarily chosen points and we qualified a state as stable if the observed quantities did not change more than about 0.1% and seemed to saturate. We were especially careful about classifying as stable a state we qualified already as transitional for another Rayleigh number. We cannot, however, completely exclude the possibility that a long-lasting transitional state was interpreted as stable.

4.5 Test cases

One of the tests we performed was an analysis of linear stability of the conductive state for perfectly insulating sidewalls. Figure 4.6 shows the stability limits of the trivial solution to

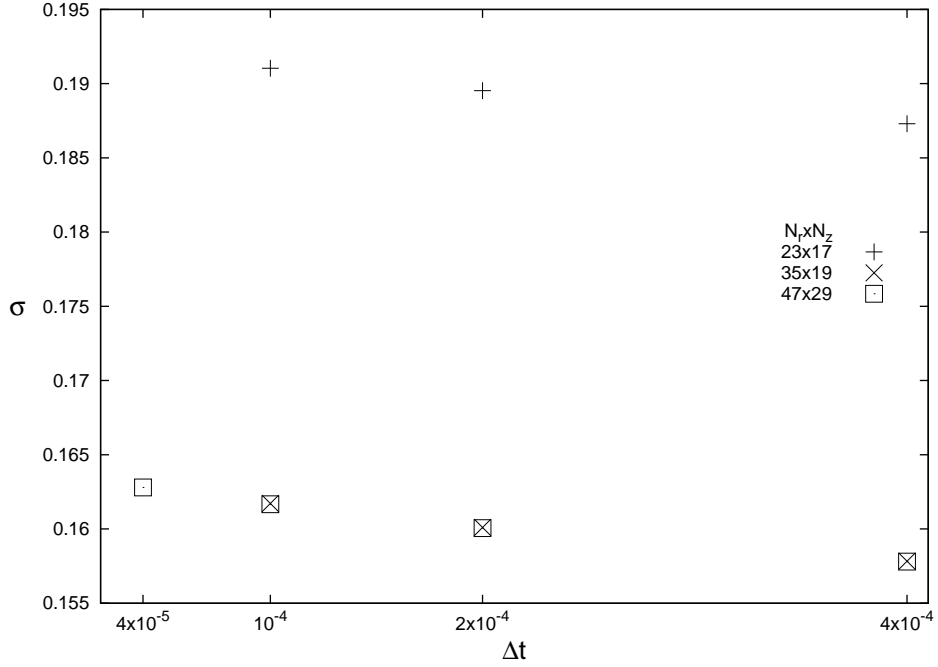


Figure 4.5: Dependence of leading eigenvalue on the timestep for three different resolutions.

perturbations with azimuthal wavenumbers $m = 0, 1$, and 2 . These results, obtained with the linearised version of the code, agree very closely with those presented by Wanschura *et al.* (1996). In the range $0.9 < \Gamma < 1.57$, the primary instability is axisymmetric; immediately below and above this range of aspect ratio, the first instability is to an eigenvector with azimuthal wavenumber $m = 1$.

The code was validated and used previously, on platforms Cray C90 and C98. The results obtained with the nonlinear axisymmetric version are described in several publications (Tuckerman & Barkley, 2000; Barkley & Tuckerman, 1989). The nonaxisymmetric nonlinear version was validated by Nore & Tuckerman (1999, 2000) by comparing the results obtained with those of Touihri *et al.* (1999).

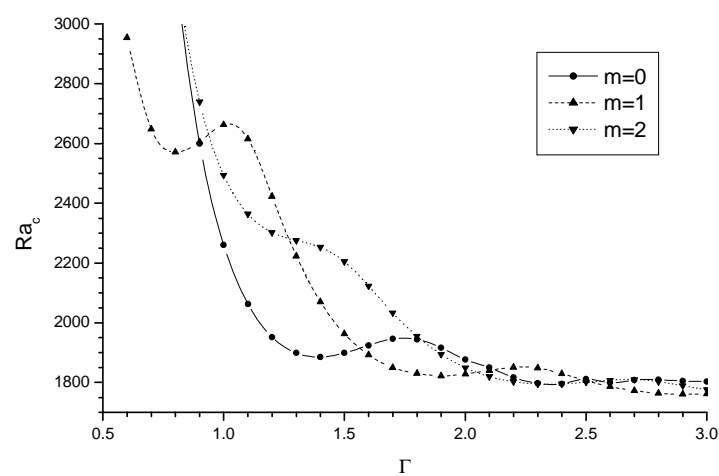


Figure 4.6: Test case: linear stability of the conductive state for insulating sidewalls.

Chapter 5

Standing and travelling waves

This chapter presents the results of our simulations for the configuration $Pr = 1$, $1.45 \leq \Gamma \leq 1.57$, for which Wunschura *et al.* (1996) reported an oscillatory bifurcation. We reproduced their results, conducting a linear analysis, and completed them by constructing and visualising representative eigenvectors associated with a complex conjugate eigenpair in an $O(2)$ -symmetric configuration. We then investigated nonlinear regimes and observed unstable standing waves and stable travelling waves.

5.1 Oscillatory bifurcation of the axisymmetric state — linear analysis

5.1.1 Steady axisymmetric state

We reproduced the primary flow for $Pr = 1$, $\Gamma = 1.47$ and $Ra = 1950$, parameters for which, according to Wunschura *et al.* (1996) and figure 4.6, the conductive state is unstable only to axisymmetric perturbations. In a fully three-dimensional simulation, starting the evolution from an arbitrary non-axisymmetric perturbation about the conductive state, we obtained an axisymmetric flow consisting of one toroidal roll. We used this state as the initial condition for higher Rayleigh numbers. According to the calculations of Wunschura *et al.* (1996), the axisymmetric state first bifurcates towards a flow with azimuthal wavenumber $m = 3$ for $1.45 \leq \Gamma < 1.53$ and with wavenumber $m = 4$ for $1.53 \leq \Gamma \leq 1.57$. The critical Rayleigh numbers Ra_{c2} at which this loss of stability occurs are given in table 5.1.

5.1.2 Eigenvalues and eigenvectors

Using the methods described in § 3.4.2, we integrated the evolution equations (2.8) linearised about axisymmetric solutions for aspect ratios $1.45 \leq \Gamma \leq 1.57$ and several different Rayleigh numbers. The leading eigenpairs calculated for $Ra = 24\,000$, $\Gamma = 1.57$ are given in Table 5.2. For these parameter values, the critical eigenvectors are (in order of decreasing growth rate): two conjugate pairs with azimuthal wavelengths $m = 4$ and $m = 3$, a real eigenvector with $m = 1$, and another conjugate pair with $m = 5$.

Figure 5.1 represents the dependence of the leading eigenvalues on Rayleigh number for aspect ratios $\Gamma = 1.47$ and $\Gamma = 1.57$, along with the azimuthal wavenumbers of the corresponding eigenvectors. Ra_{c2} was calculated by determining the zero crossing of $\mu(Ra)$, the growth rate of the leading eigenvalue (that of largest real part), by linear interpolation. (Critical Rayleigh numbers calculated by introducing perturbations into nonlinear simulations at various values of Ra ,

Γ		present study	Wanschura <i>et al.</i> (1996)	error
1.47	Ra_{c2}	24 738	24 928	0.76%
	ω_{c2}	42.33	42.54	0.48%
	m_{c2}	3	3	
1.57	Ra_{c2}	22 849	23 011	0.70%
	ω_{c2}	45.26	45.47	0.45%
	m_{c2}	4	4	

Table 5.1: The parameters of the oscillatory bifurcations found by linear analysis: critical Rayleigh numbers Ra_{c2} , critical frequencies ω_{c2} and azimuthal wavenumbers of critical eigenvectors for two aspect ratios.

and fitting the initial evolution to an exponential to calculate growth or decay rates $\mu(Ra)$ gave similar results.) We then calculated $\omega_{c2} \equiv \omega(Ra_{c2})$, also by linear interpolation. The values we obtained for two aspect ratios $\Gamma = 1.47$ and $\Gamma = 1.57$, and the corresponding values published by Wanschura *et al.* (1996) are those given in Table 5.1. The critical wavenumbers are the same, and the errors in Ra_{c2} and in ω_{c2} are less than 1%. In what follows, we will focus on the $m = 3$ instability, since the behaviour and the mechanism of the $m = 4$ transition are similar; the aspect ratio is $\Gamma = 1.47$ unless otherwise specified.

We summarise here the differences between our numerical method and that of Wanschura *et al.* (1996). We linearised a timestepping code in order to, in effect, carry out the power method (supplemented by an Arnoldi decomposition) on the exponential $\exp(L\Delta t)$ of the Jacobian. Wanschura *et al.* (1996) constructed the Jacobian matrix L and used inverse iteration to compute its eigenvalues. Our calculation was restricted to one of the two identical decoupled subproblems, corresponding to only one of the invariant subspaces of the form (2.19a) or (2.19b). As a result, the complex eigenfunctions we show in table 5.2 are all in the eigenspace corresponding to standing waves, with three axes of reflection symmetry. Basis vectors for the remainder of the four-dimensional eigenspace can be found by rotating the eigenvectors of table 5.2, i.e. multiplying by $\sin(m\theta)$ instead of $\cos(m\theta)$. Wanschura *et al.* (1996), in contrast, used the travelling wave form as an initial condition or invariant subspace, as we show below.

In figure 5.2, we show representative elements of the eigenspace associated with the $m = 3$ complex eigenvector at $Ra = 25 000$. Figures 5.2(a, b) show $\hat{h}^R(r, z) \cos(m\theta)$ and $\hat{h}^I(r, z) \cos(m\theta)$, while figures 5.2(c-g) are generated via

$$C(\hat{h}^R(r, z) \cos(m(\theta - \theta_0)) + \hat{h}^I(r, z) \sin(m(\theta + \theta_0))), \quad (5.1)$$

a form equivalent to (2.28) after translation of θ and of t . Clockwise travelling waves ensue for $m\theta_0 = 0$ (c), counterclockwise travelling waves for $m\theta_0 = \pi/2$ (e), and standing waves at different temporal phases for $m\theta_0 = \pm\pi/4$ (d,f). Thus, the angle $m\theta_0$ is similar to that used in figure 2.2. An eigenvector which corresponds to neither travelling nor standing waves is shown in figure 5.2(g). These are all depicted on the slice $z = 0$; when we plot the field of figure 5.2(c) at $z = 0.3$, we recover the form shown by Wanschura *et al.* (1996). We emphasize, however, that the other fields depicted in figure 5.2 are all equally valid eigenvectors. In particular, a nonlinear analysis, such as the simulations presented below, is required to determine whether the resulting nonlinear flow near onset is a travelling or a standing wave.

eigenvalue	eigenvector visualisation real part	\pm imaginary part	wavenumber	error
$0.86 \pm 46.3i$			4	10^{-10}
$0.24 \pm 41.6i$			3	2×10^{-10}
-0.81		-	1	6×10^{-10}
$-4.40 \pm 45.9i$			5	9×10^{-7}

Table 5.2: For $Ra = 24\,000$, $\Gamma = 1.57$: eigenvalues, visualization of corresponding eigenvectors, azimuthal wavenumber and residual error. The visualised field is the temperature at the midplane; for complex conjugate eigenpairs the real and imaginary parts of the eigenvector are depicted. Solid (dashed) contours indicate positive (negative) values of h .

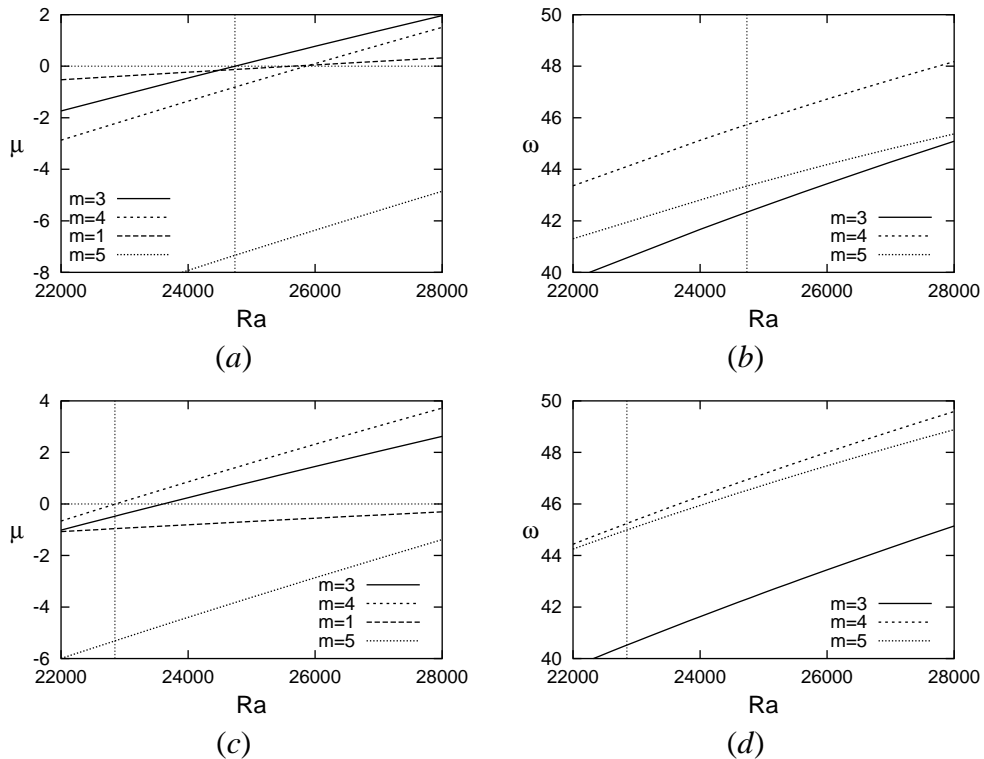


Figure 5.1: Leading eigenvalues as a function of Rayleigh number for aspect ratio $\Gamma = 1.47$: (a) real part, (b) imaginary part and for aspect ratio $\Gamma = 1.57$: (c) real part, (d) imaginary part. Vertical thin dashed line marks Ra_{c2} .

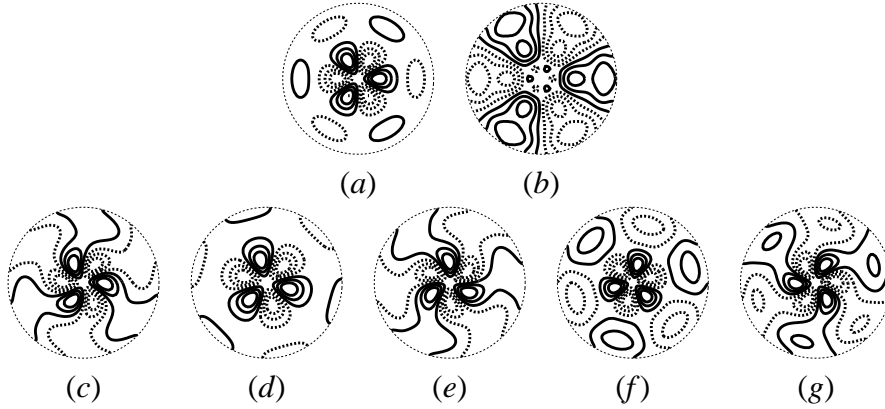


Figure 5.2: Eigenvectors for $\Gamma = 1.47$, $Ra = 25\,000$ (temperature field contours at $z = 0$): (a) real part of the critical eigenvector; (b) imaginary part of the critical eigenvector; (c-g) superposition of the two fields via $\hat{h}^R(r, z) \cos(m(\theta - \theta_0)) + \hat{h}^I(r, z) \sin(m(\theta + \theta_0))$, with $m\theta_0$ of (c) 0, (d) $\pi/4$, (e) $\pi/2$, (f) $3\pi/4$, (g) 0.92π .

5.2 Nonlinear simulation of time-dependent states

5.2.1 Weakly unstable standing waves

Above the critical Rayleigh number Ra_{c2} , a slightly perturbed axisymmetric state evolved in our simulations towards a three-dimensional time-dependent state, presented, for $\Gamma = 1.47$, in figures 5.3 and 5.4. Figure 5.3 shows temperature contours in the midplane at six regularly spaced instants in time within one oscillation period. In contrast to the eigenvectors depicted previously, figure 5.3 displays full nonlinear temperature fields, which are dominated by a large axisymmetric component. There are six pulsing extrema, engendering oscillation between two triangular structures of opposite phases (figures 5.3 *a* and 5.3 *d*). Figure 5.4 shows the temperature dependence on the angle θ for fixed radius and height at different times. Six fixed nodes identify this state as a standing wave with azimuthal wavelength $2\pi/3$. At each instant, the flow is invariant under rotation in θ by $2\pi/3$. In addition, this flow is also symmetric with respect to three different axes of reflection.

The standing wave state persists for such a long time that it might seem stable. However, a small reflection-symmetry breaking imperfection develops that eventually leads to the transition to travelling waves. Figure 5.5 shows the temperature dependence on the angle θ for the same parameters as figure 5.4, but at a later time. The breaking of reflection symmetry can be observed when the amplitude of the standing wave is small. The standing waves can be stabilised by imposing reflection symmetry. When we did this, above a threshold $Ra_{c3} \approx 27\,000$, we discovered a new (unstable) standing-wave solution, displayed in figure 5.7 for $Ra = 30\,000$.

In order to study the transition from standing to travelling waves, we monitored the growth of antisymmetric components. When the standing wave is still dominant, the amplitude of the antisymmetric components behaves in time like $(A \cos \omega t + B) \exp(\mu_{sw \rightarrow tw} t)$, where $\mu_{sw \rightarrow tw}$ is the growth rate from standing waves to travelling waves. The growth rate $\mu_{sw \rightarrow tw}$, shown on figure 5.6 as a function of Ra , is about two thirds of $\mu_{0 \rightarrow 3}$, the growth rate from the axisymmetric state to an $m = 3$ flow (denoted in the previous sections by μ). The observed lifetime of the standing waves decreases as the Rayleigh number is increased, since the growth rate $\mu_{sw \rightarrow tw}$ increases.

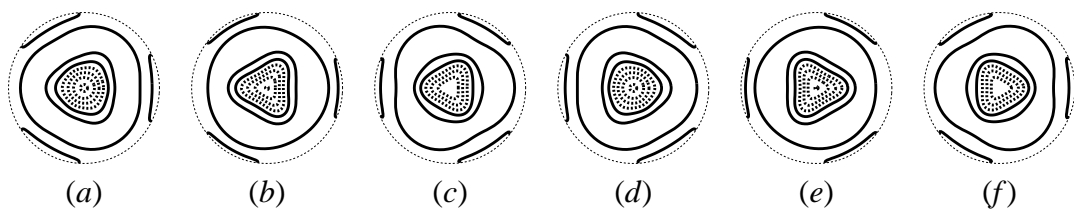


Figure 5.3: Standing waves at $\Gamma = 1.47$, $Ra = 26000$: temperature contours at $t = 0, T/6, 2T/6, \dots$

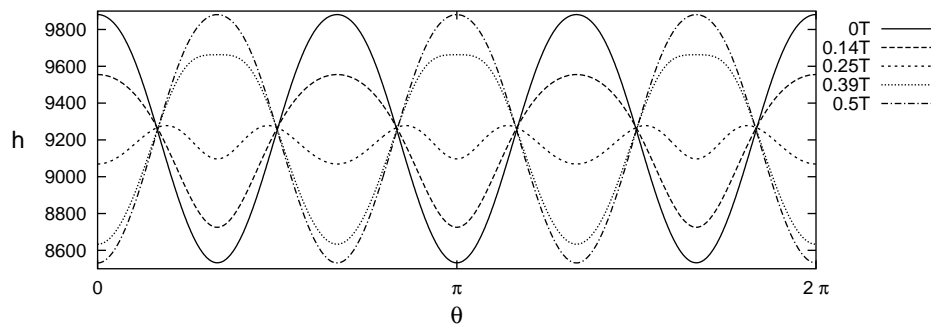


Figure 5.4: Standing waves at $\Gamma = 1.47$, $Ra = 26000$: temperature versus θ at $(r,z) = (0.7,0.3)$ at five successive times.

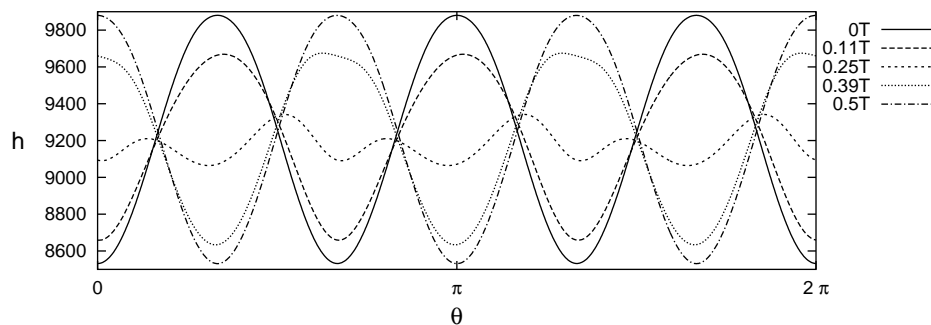


Figure 5.5: Standing waves at $Ra = 26000$ after a time integration sufficiently long to see the beginning of breaking of reflection symmetry. Temperature versus θ at $(r,z) = (0.7,0.3)$ at five successive times.

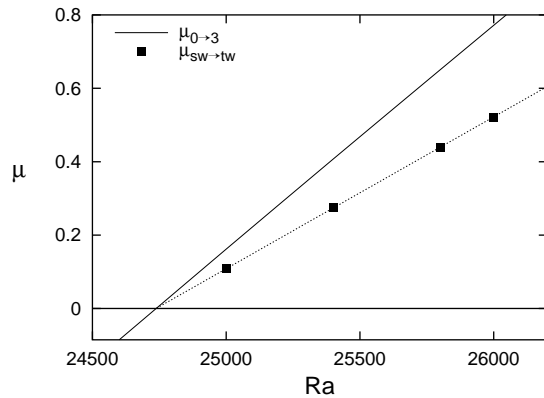


Figure 5.6: Growth rates as a function of Rayleigh number. Solid line: growth rate $\mu_{0 \rightarrow 3}$ of $m = 3$ eigenvector (either standing or travelling waves) from the axisymmetric solution (from linear evolution). Squares: growth rate $\mu_{SW \rightarrow TW}$ of travelling waves from standing waves (from nonlinear simulation) with linear fit as dashed line.

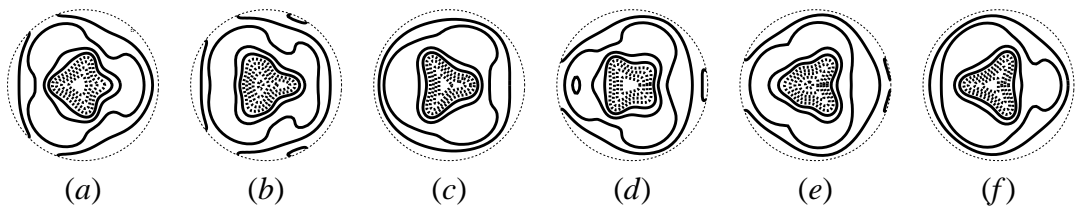


Figure 5.7: Oscillatory solution obtained at $Ra = 30000$ by imposing reflection symmetry: temperature contours at $t = 0, T/6, 2T/6, \dots$

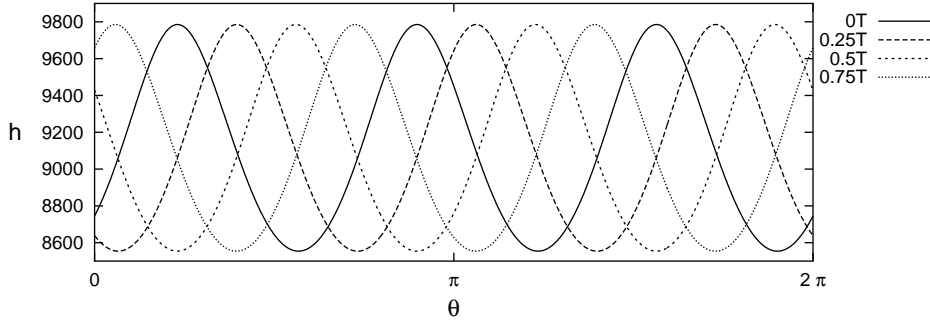


Figure 5.8: Travelling waves at $Ra = 26000$: temperature versus θ angle, for $(r, z) = (0.7, 0.3)$, at four different instants during one oscillation period T .

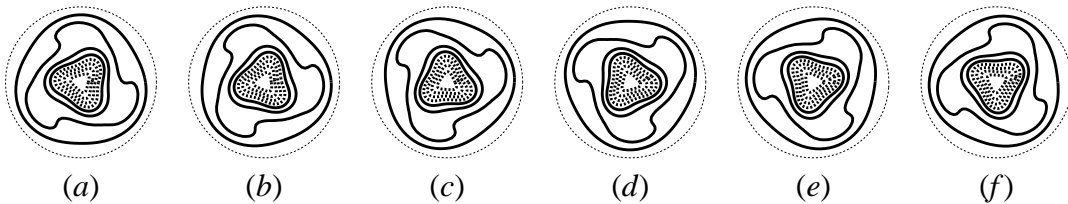


Figure 5.9: Counterclockwise travelling wave at $Ra = 26000$: temperature contours at $t = 0, T/6, 2T/6, \dots$

5.2.2 Stable travelling waves

After the pattern has evolved sufficiently from the standing wave state, the fixed antinodes abruptly begin to rotate about the cylinder axis. The six pulsing spots change into three rotating spots, as the standing waves become travelling waves with the same azimuthal wavenumber. Figures 5.8 and 5.9 depict the temperature profiles and contours of the travelling waves. The travelling waves, like the standing waves, have three-fold rotational symmetry, but do not have reflection symmetry.

Travelling waves are the final state of the time evolution. The reason for which we obtained standing waves before travelling waves in our simulations is that our initial conditions were reflection symmetric and our numerical procedures introduce antisymmetric perturbations at a low rate. When the Rayleigh number is decreased, travelling waves persist until Ra reaches Ra_{c2} .

We conducted simulations for several values of Γ in the range $1.45 \leq \Gamma < 1.53$ and observed weakly unstable standing waves and stable travelling waves for all of them. The same scenario also occurs for $1.53 \leq \Gamma \leq 1.57$, but with azimuthal wavenumber $m = 4$ instead of $m = 3$.

5.2.3 Amplitudes and frequencies

We calculated the energy E of both types of waves by first defining a norm whose square is

$$\frac{1}{Ra} \left(\frac{\langle \mathbf{u}, \mathbf{u} \rangle}{Pr} + \frac{\langle h, h \rangle}{Ra} \right), \quad (5.2)$$

where $\langle \cdot, \cdot \rangle$ denotes spatial integration; (5.2) is one of many possible choices for this system. We then simulated the nonlinear evolution equations and calculated (\mathbf{u}, h) as the difference between

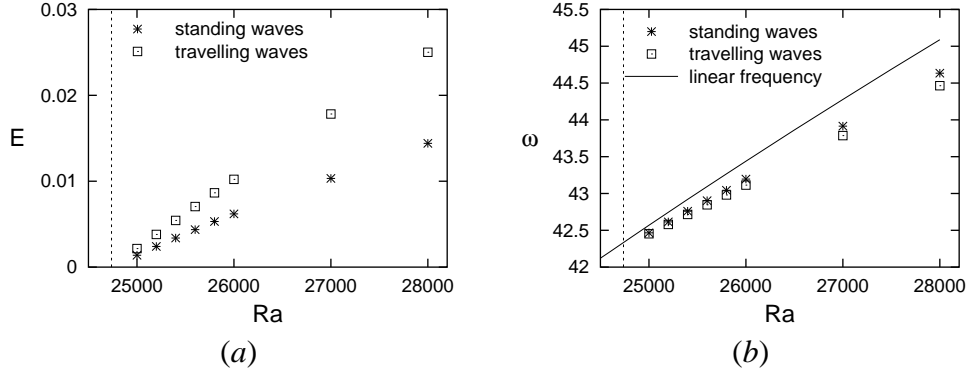


Figure 5.10: Dependence of energy (a) and frequency (b) on Rayleigh number for standing and travelling waves. Vertical dashed line indicates the critical Rayleigh number Ra_{c2} for onset of the waves.

the three-dimensional and the axisymmetric solution. We define E to be the integral of (5.2) over one oscillation period.

The energies E_{sw} , E_{tw} and frequencies ω_{sw} , ω_{tw} as a function of Ra are shown in figure 5.10. The energies and frequencies for the two types of waves are quite close. The frequency $\omega_{0 \rightarrow 3}$ obtained from linear stability analysis is also reproduced from figure 5.1 (b) for comparison. For both types of waves, the frequencies near the threshold are close to the Hopf frequency and the energy satisfies $E \propto (Ra - Ra_{c2})$. These are hallmarks of a supercritical Hopf bifurcation.

5.2.4 Normal form coefficients

Using the growth rates, amplitudes and frequencies of the standing and travelling waves that we have presented in sections 5.1.2 and 5.2.3, it is possible to calculate the coefficients of the normal form (2.31) for our particular case. The bifurcation parameter $\mu = \mu_{0 \rightarrow 3}$ and frequency $\omega = \omega_{0 \rightarrow 3}$ vary linearly with $Ra - Ra_{c2}$, while the other coefficients a_r , b_r , a_i , b_i are constants.

From the data in figure 5.1 (a,b), we extract the fits

$$\mu_{0 \rightarrow 3} = 14.98 \frac{Ra - Ra_{c2}}{Ra_{c2}}, \quad (5.3a)$$

$$\omega_{0 \rightarrow 3} = 42.33 + 21.21 \frac{Ra - Ra_{c2}}{Ra_{c2}}. \quad (5.3b)$$

From the data in figure 5.10 we extract the fits

$$E_{tw} = A_{tw}^2 = \rho_+^2 = \frac{-\mu}{b_r} = 0.2037 \frac{Ra - Ra_{c2}}{Ra_{c2}}, \quad (5.4a)$$

$$E_{sw} = A_{sw}^2 = \rho_+^2 + \rho_-^2 = 2 \frac{-\mu}{a_r + 2b_r} = 0.13 \frac{Ra - Ra_{c2}}{Ra_{c2}}, \quad (5.4b)$$

$$\omega_{tw} = \omega_{0 \rightarrow 3} - \frac{b_i}{b_r} \mu = 42.33 + 16.26 \frac{Ra - Ra_{c2}}{Ra_{c2}}, \quad (5.4c)$$

$$\omega_{sw} = \omega_{0 \rightarrow 3} - \frac{a_i + 2b_i}{a_r + 2b_r} \mu = 42.33 + 17.29 \frac{Ra - Ra_{c2}}{Ra_{c2}}. \quad (5.4d)$$

Equations (5.4) are used to determine the nonlinear coefficients as:

$$b_r = -73.5, \quad (5.5a)$$

$$a_r = -83.6, \quad (5.5b)$$

$$b_i = -24.3, \quad (5.5c)$$

$$a_i = 11.7. \quad (5.5d)$$

An additional equation is provided by the data in figure 5.6 showing the growth rate $\mu_{sw \rightarrow tw}$ from standing to travelling waves:

$$\mu_{sw \rightarrow tw} = \frac{2a_r}{a_r + 2b_r} \mu = 10.23 \frac{Ra - Ra_{c2}}{Ra_{c2}}, \quad (5.6)$$

and provides a second determination of a_r

$$a_r = \frac{-\mu_{sw \rightarrow tw}}{A_{sw}^2} = -78.8. \quad (5.7)$$

which differs by 6% from (5.5b).

5.3 Conclusion

We have used both nonlinear simulations and linear stability analysis to elucidate the behaviour of Rayleigh–Bénard convection in the parameter region of $1.45 \leq \Gamma \leq 1.57$, $Pr = 1$ first studied by Wanschura *et al.* (1996). In this regime, the primary axisymmetric convective state loses stability to an $m = 3$ or $m = 4$ perturbation via a Hopf bifurcation whose critical eigenspace is four-dimensional. We calculated representative eigenvectors and explained how these relate to those computed by Wanschura *et al.* (1996). The bifurcation scenario guarantees that branches of standing waves and of travelling waves are created at the bifurcation, but that at most one of these branches is stable. Our nonlinear simulations showed long-lived standing waves which were eventually succeeded by travelling waves, both as time progressed and as the Rayleigh number was increased. We explained this by showing that the rate of transition from standing waves to travelling waves, while positive, is nevertheless small. In the absence of long-time integration and of these analyses, it would be easy to conclude that the standing waves were stable. This underlines the importance of calculating growth rates, in addition to carrying out nonlinear simulations, and of using established bifurcation scenarios to interpret physical phenomena.

We have not sought to determine the limits of the range of this phenomenon, in aspect ratio and Prandtl number. As these ranges were given by Wanschura *et al.* (1996) only for $Pr = 1$, a future direction would be to determine the whole zone in the parameter space where the Hopf bifurcation occurs.

Chapter 6

Convective patterns – insulating sidewalls

The second part of our study was inspired by the results of Hof *et al.* (1999), who observed coexistence of several stable states for one configuration of control parameters. In our simulations we matched their Prandtl number and aspect ratio and used two kinds of thermal boundary conditions. This chapter presents the convective patterns we obtained for perfectly insulating sidewalls and the next chapter those for perfectly conducting sidewalls. For both cases we obtained a wide variety of coexisting steady and time-dependent flows.

6.1 Simulation of the experiment

Hof, Lucas & Mullin (1999) in their experiment produced a large number of convective patterns by increasing and decreasing the Rayleigh number in a variety of ways. We run nonlinear simulations for their configuration of control parameters, and different thermal boundary conditions. While in the experiment the cylinder sidewalls were well insulating, we used either perfectly insulating or perfectly conducting sidewalls. In this chapter we describe the results we obtained for the first case. Matching the parameters of Hof *et al.* (1999), we set the Prandtl number to 6.7 (that of water) and the aspect ratio to 2. We have performed a sequence of simulations, varying the initial state and the Rayleigh number, in order to find the asymptotic state for each configuration. Rather than filling in the whole table of combinations of Rayleigh numbers and initial conditions, we attempted to probe this space, concentrating in particular on obtaining patterns resembling those of Hof *et al.* (1999) at $Ra = 14\,200$, for which they observed five different steady patterns. The flows we obtain can be used in the future as a basis for constructing the complete bifurcation diagrams. Unlike in the experiment, we did not seek inverse patterns for the reasons given in § 2.4.2.

In order to qualify a solution as stable, we watched its nonlinear evolution as explained in § 4.4. The field visualised throughout this and the next chapter is the temperature deviation from the basic vertical profile, referred to elsewhere just as temperature, as for fixed z they differ only by a constant. The horizontal cuts are done in the midplane, dark (bright) areas indicate hot (cold) zones. The time is expressed in dimensionless units of the vertical thermal diffusion time $[t] = d^2/\kappa$.

We initialised the simulations with slightly perturbed conductive solution. This can be seen as corresponding to a sudden jump of heating power in an experimental setup, where previously a fluid was maintained below the convection threshold. Such simulations gave us different patterns, depending on Rayleigh number. Once we obtained these stable convective flows, we used them as initial states at other Rayleigh numbers. This is again comparable to an experimental situation in which, once a pattern is stabilised, the heating power is changed abruptly. The pat-

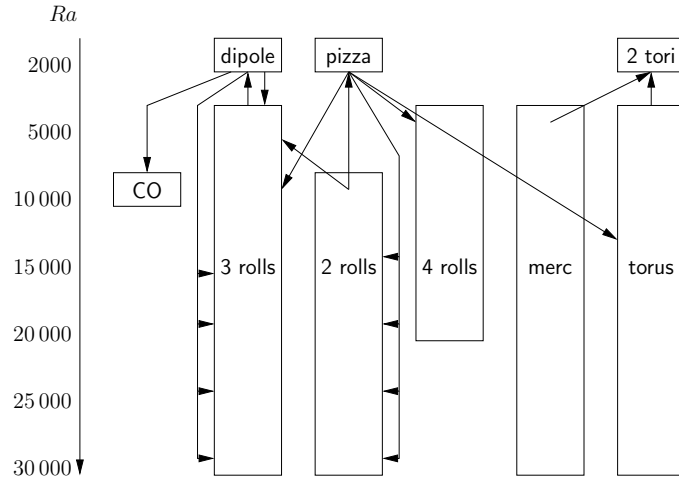


Figure 6.1: Schematic diagram of stability ranges and transitions between convective patterns as a function of Rayleigh number for $\Gamma = 2$, $Pr = 6.7$ and insulating sidewalls.

terns we observed and the transitions between them are described in the sections which follow. In order to orient the reader, we anticipate these results and present on figure 6.1 a simplified diagram of the stable patterns we observed for different Rayleigh numbers. A more quantitative summarising diagram can be found in § 6.11, where we present the value of the temperature at one point as a function of Ra for all stable patterns found (figure 6.28).

6.2 Evolution from perturbed conductive state

In the first series of simulations, we initialised the fields with the conductive solution slightly perturbed by an arbitrary non-physical perturbation satisfying the boundary conditions (presented on figure 6.2, *a*). We run a series of simulations for Rayleigh numbers between 1600 and 23 000. Depending on the Rayleigh number, this state evolves towards different flows shown on figure 6.2 (*b-e*).

For $Ra \lesssim 1900$, the initial perturbation decays to zero, resulting in the conductive state. For Ra near 2000, the final state is a pattern with symmetry D_2 , which we will call the *pizza state* (shown on figure 6.2, *b*). This state has four well-separated sections, resembling pieces of a pizza. Each section has either a hot round spot in the centre with colder area along the sidewall, or a cold round spot in the centre with warmer area at the sidewall.

For Ra between 3000 and 20 000, the system evolves towards states with parallel or rather quasi-parallel rolls (see figure 6.2, *c, d*): below 10 000 the final state is a four-roll pattern and for 10 000 and above, the final solution is a three-roll state. Finally, for $Ra \approx 23 000$, the final pattern consists of three radial spokes of cold descending fluid, named by Hof (1997) a *mercedes pattern* (figure 6.2, *e*). For all these patterns, the roll boundaries become more curved as the Rayleigh number is increased.

6.3 Three-roll patterns

In the second series of simulations, we used as the initial condition the three-roll state previously converged at $Ra = 14 200$. Below the critical Rayleigh number this pattern decays to zero via an intermediate *dipole pattern* and for $Ra = 2000$ the three rolls transform into a stable dipole

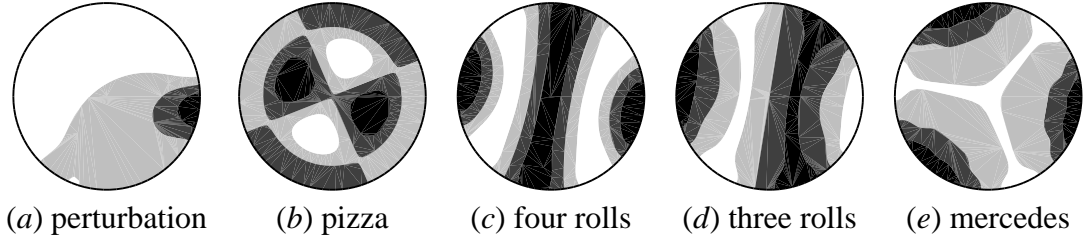


Figure 6.2: Initial perturbation (a) and convective patterns obtained from perturbed conductive state at different Rayleigh numbers: (b) pizza at $Ra = 2400$, (c) four rolls at $Ra = 5000$, (d) three rolls at $Ra = 12000$, (e) mercedes at $Ra = 24000$. Visualisation of the temperature in the cylinder's midplane, dark: hot/ascending, bright: cold/descending fluid.

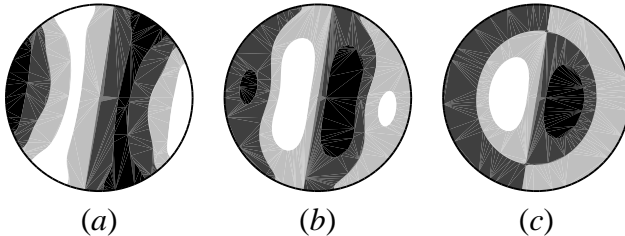


Figure 6.3: Evolution of the convective pattern at $Ra = 2000$ for a simulation initialised with a three-roll pattern (stabilised previously at $Ra = 10000$): (a) $t = 0$, (b) $t = 8$, (c) $t = 32$.

state, as shown on figure 6.3. The dipole pattern (c) resembles an $m = 1$ azimuthal mode.

For $Ra = 5000$ and above, up to $Ra = 33000$, the three-roll state remains stable, with the rolls more curved for higher Rayleigh numbers (see figure 6.4). An exception is the range between $Ra = 20000$ and $Ra = 25000$, where the band of colder fluid between the central roll and the left roll moves slightly towards the centre as the Rayleigh number is increased (see figure 6.5). This is similar to the results of Hof *et al.* (1999). They observed the same tendency and found that the leftmost roll vanishes eventually at $Ra = 21000$, where the flow forms a two-roll pattern. We did not obtain two rolls in our simulations, nevertheless we did observe a different evolution of the system. Figure 6.6(a) displays the temperature at one arbitrarily chosen point as a function of Rayleigh number. We can see that for $20000 < Ra < 25000$ this quantity deviates from the general profile. Figure 6.6(b) displays the dependence on Rayleigh number of the total energy of the system defined in (3.24). In the zone of interest the energy deviates slightly from the profile; therefore we can already conclude that a bifurcation is present. In the experiment this evolution yielded a two-roll pattern and, during our further analysis of two-roll states, we found that their energy indeed approaches that of shifting three rolls.

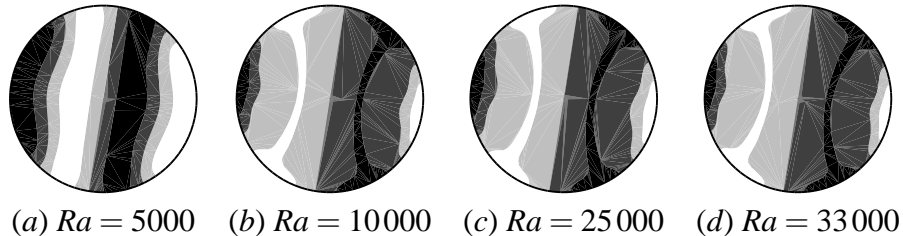


Figure 6.4: Three-roll patterns converged at different Rayleigh numbers.

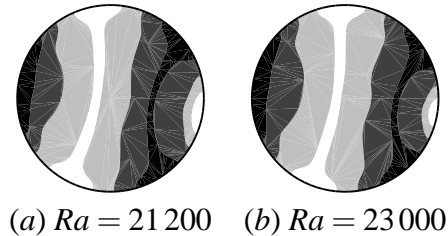


Figure 6.5: Three-roll pattern with the central roll moving to the right, obtained for Rayleigh numbers between 20 000 and 25 000.

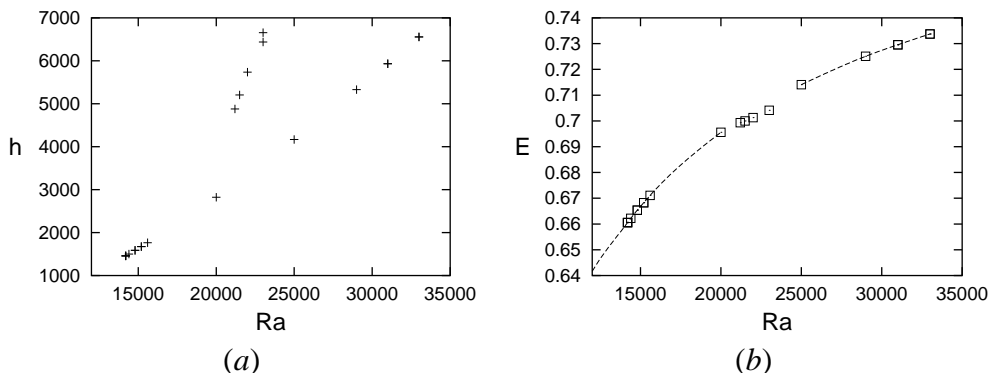


Figure 6.6: Dependence of the three-roll patterns on Rayleigh number: (a) temperature at $r = 0.3$, $z = 0.25$, $\theta = 0$; (b) energy.

6.4 Evolution from four-rolls

We used a four-roll pattern converged at $Ra = 3000$ as initial condition for simulations at $14200 \leq Ra \leq 20000$. The newly evolved patterns are also of the four-roll family, and, as in the case of three rolls, they are more curved as the Rayleigh number is increased (see figure 6.7).

We used the four-roll state converged for $Ra = 20000$ as initial condition at Rayleigh numbers 25 000 and 29 000. This time the geometry of the pattern changes, as displayed on figure 6.8 – the four-roll pattern turns into a *cross pattern* with four spokes of descending cold fluid. The cross flow does not saturate, but still slightly evolves; we suspect that it is rather a transitional than an asymptotic state. This would be in agreement with Hof (2003), who observed that the cross pattern is a long-lasting transient state unstable to a mercedes pattern.

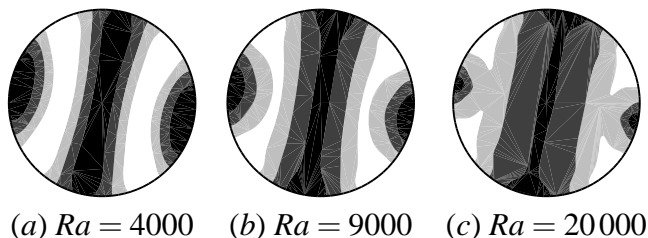


Figure 6.7: Four-roll pattern for different Rayleigh numbers.

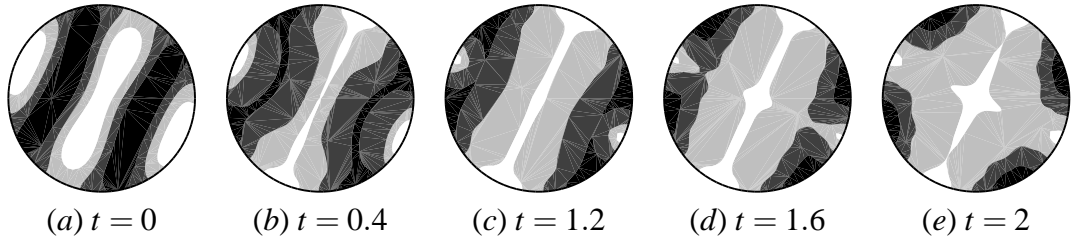


Figure 6.8: Evolution of the four-roll pattern towards (probably transitional) cross pattern at $Ra = 25\,000$.

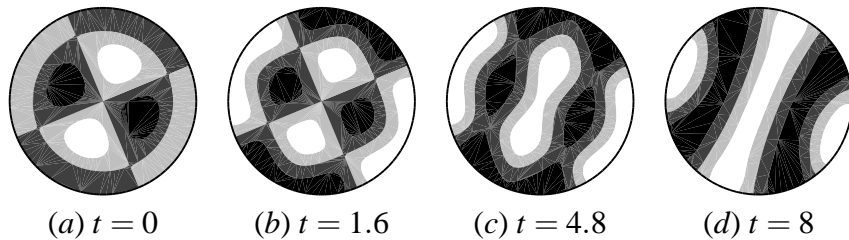


Figure 6.9: Evolution from pizza pattern at $Ra = 5000$.

6.5 Evolution from pizza pattern

We used the pizza pattern evolved at $Ra = 2000$ as an initial condition for a series of simulations at several Rayleigh numbers between 5000 and 29 000. In this range the pizza pattern is not stable. For $Ra = 5000$ it changes into four rolls (see evolution on figure 6.9) and for $Ra = 10000$ into three rolls (figure 6.10). For $Ra = 14\,200$ the initial pizza flow evolves into a *torus pattern* – an axisymmetric state with one toroidal roll, passing before through an intermediate *eight pattern*. This evolution is displayed on figure 6.11. The transitional eight pattern was also observed by Hof (2003).

For $Ra \geq 15\,000$ the pizza state, after passing through a series of various transitional patterns, becomes eventually a two-roll flow. Figure 6.12 displays the evolution of the system for $Ra = 16\,000$, where we describe the intermediate states as: *triangle mosaic* (b), *eye* (d) and *imperfect eight* (f). Figure 6.13 presents the system behaviour for $Ra = 29\,000$, where the intermediate patterns between pizza and two rolls are *six-radius elongated-star* (d) and *six-radius star* (e).

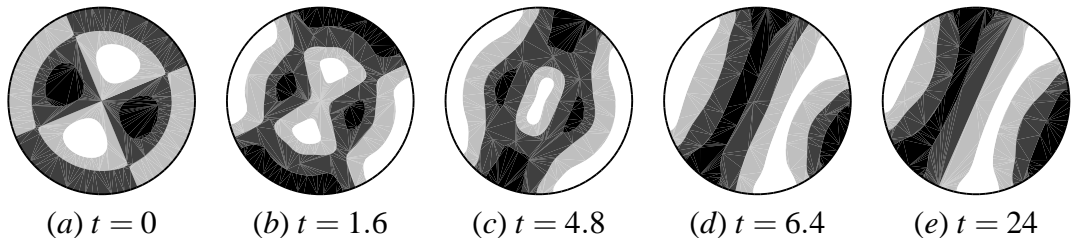


Figure 6.10: Evolution from pizza pattern at $Ra = 10\,000$.

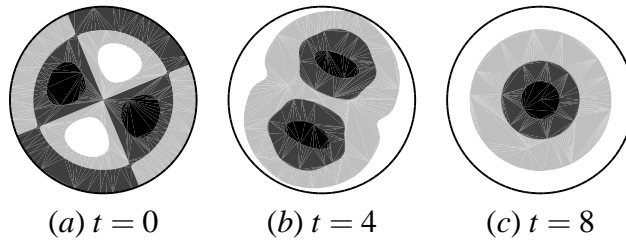


Figure 6.11: Evolution of convective pattern at $Ra = 14\,200$: from initial pizza through eight towards final torus pattern.

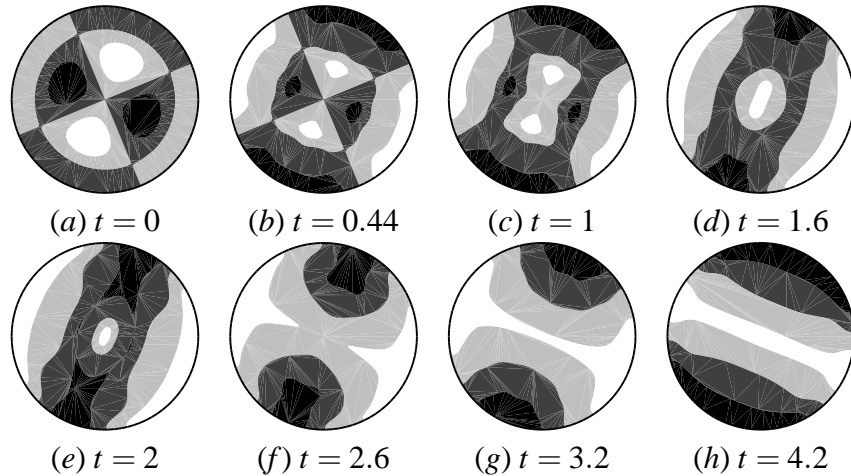


Figure 6.12: Evolution of convective pattern at $Ra = 16\,000$ from initial pizza through a series of intermediate states towards the final two-roll pattern.

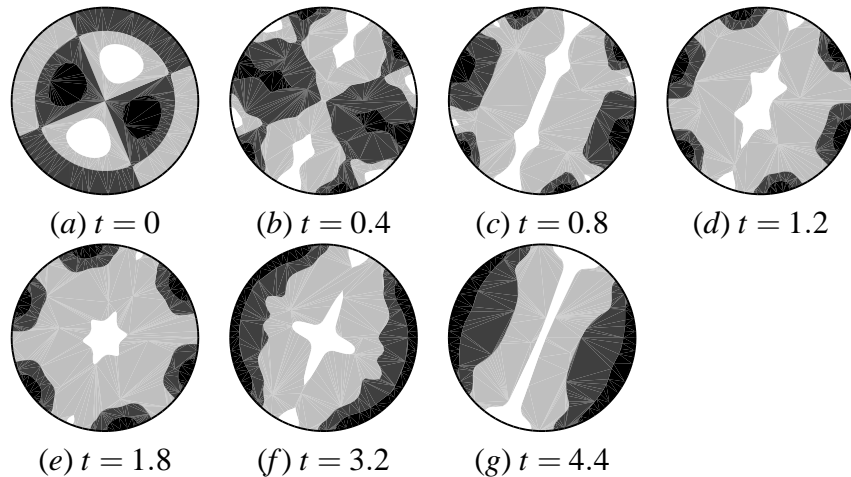


Figure 6.13: Evolution of convective pattern at $Ra = 29\,000$ from initial pizza through a series of intermediate states towards the final two-roll pattern.

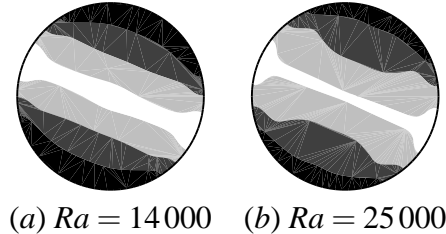


Figure 6.14: Two-roll pattern at different Rayleigh numbers.

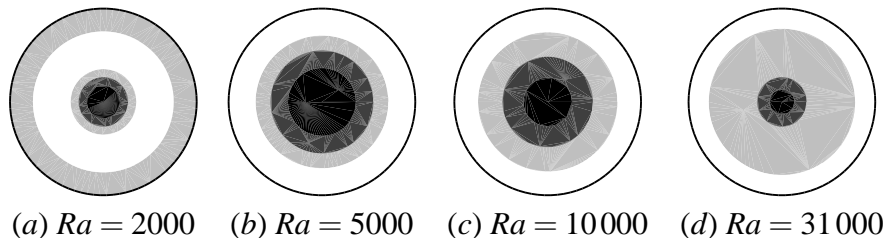


Figure 6.15: Axisymmetric patterns at different Rayleigh numbers.

6.6 Evolution from two rolls

Another initial condition we used was the two-roll state, converged previously at $Ra = 15\,000$. For $Ra = 2000$ it leads to the pizza pattern, and for $Ra = 5000$ a three-roll state. For $10\,000 \leq Ra < 29\,000$, we found the two roll pattern stable. At $Ra = 29\,000$ the roll boundaries start oscillating slightly. Figure 6.14 presents two-roll flow visualisations for different Rayleigh numbers.

6.7 Axisymmetric flows

The axisymmetric pattern, obtained at $Ra = 14\,200$ and used as initial condition, also leads to axisymmetric patterns for a wide range of Rayleigh numbers $2000 \leq Ra \leq 33\,000$ (see figure 6.15). For $Ra = 2000$ there are two concentric toroidal rolls instead of one. This is in partial agreement with Hof (1997), who found toroidal flow stable for $Ra > 3500$, but unstable towards travelling waves for $Ra \gtrsim 23\,000$. It cannot be excluded that the time of the simulation was too short, but the pattern seems to converge towards a stationary flow, although in an oscillatory way. All axisymmetric patterns we observed were truly two-dimensional, with no azimuthal velocity.

6.8 Evolution from mercedes pattern

We ran a series of simulations using as the initial condition the mercedes pattern evolved at $Ra = 23\,000$. For every Rayleigh number in the range $5000 \leq Ra \leq 29\,000$ this gave stable mercedes patterns and for $Ra = 2000$ it evolves to a two-roll axisymmetric pattern. Figure 6.16 displays the final patterns for different Rayleigh numbers.

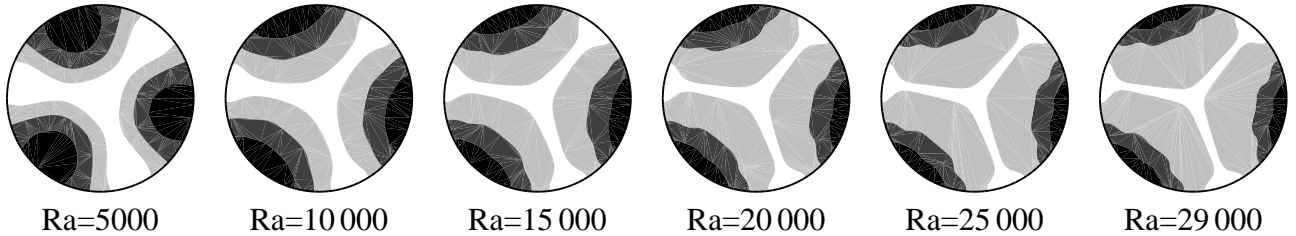


Figure 6.16: Mercedes patterns at different Rayleigh numbers.

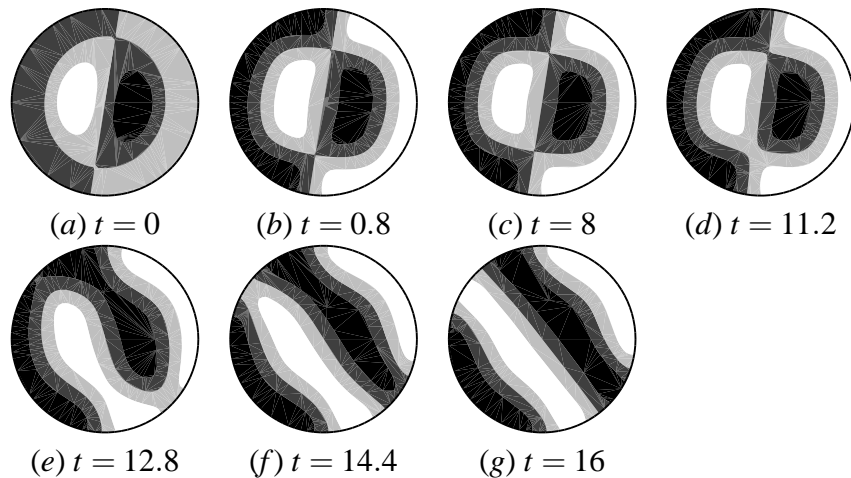


Figure 6.17: Evolution of dipole pattern at $Ra = 5000$.

6.9 Evolution from dipole pattern

Another initial condition we used was the dipole pattern converged from three rolls at $Ra = 2000$. For Rayleigh numbers between 5000 and 29 000, with the exception of 10 000, the flow evolves towards a three-roll pattern.

The evolution of the flow at $Ra = 5000$ is presented on figures 6.17 and 6.18. At this Rayleigh number the system passes through a long-lasting intermediary *dipole smile state* (figure 6.17, *c*). The lifetime of the intermediate pattern is of order 10.

The flow patterns appearing for $Ra = 10000$ are depicted on figure 6.19. An intermediate dipole smile state appears also (*b*), with lifetime of about 2. The final solution is a *CO pattern* (*c*), composed of one curved and one circular roll. It looks like a three-roll pattern with the ends of two neighbouring rolls joined together, but its energy is higher than that of the three-roll state at the same Ra .

At higher Rayleigh numbers, where the asymptotic solution is again three-roll flow, transitional patterns also appear (figure 6.20). The final patterns are shown on figure 6.21, with the initial dipole pattern for comparison. The initial pattern orientation does not seem to predetermine the direction of the rolls of the final pattern.

Figure 6.22 depicts the energy as a function of Rayleigh number. For comparison, the energy of three-roll states from §6.3 is also displayed. They are in perfect agreement with the sole exception of $Ra = 10000$: the energy of the CO state is higher.

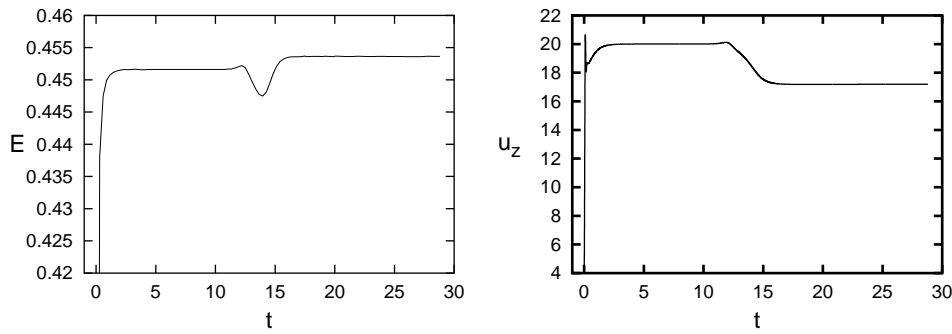


Figure 6.18: Evolution from the dipole pattern at $Ra = 5000$: (a) energy, (b) vertical velocity at one point. A long-lasting transient state is visible between $t = 3$ and $t = 12$.

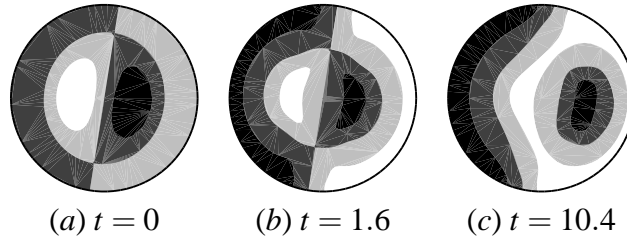


Figure 6.19: Evolution of dipole pattern through dipole smile into final CO pattern at $Ra = 10000$.

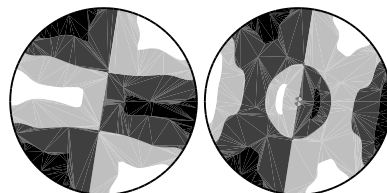


Figure 6.20: Transitional patterns observed during evolution from dipole into three-roll pattern: (a) $Ra = 14200$, $t = 0.8$; (b) $Ra = 20200$, $t = 0.4$.

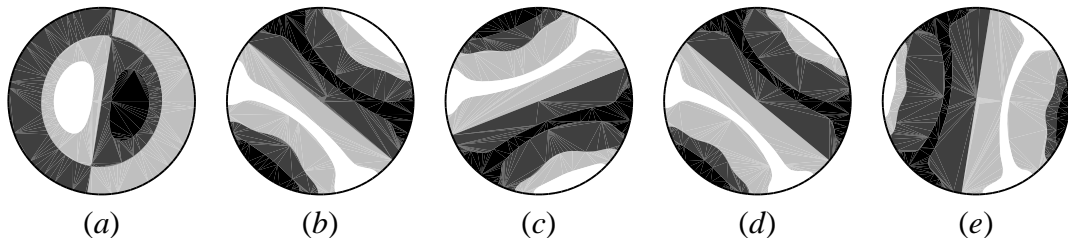


Figure 6.21: Initial dipole state (a) and final patterns for Rayleigh numbers: (b) 14200, (c) 16000, (d) 20000, (e) 29000.

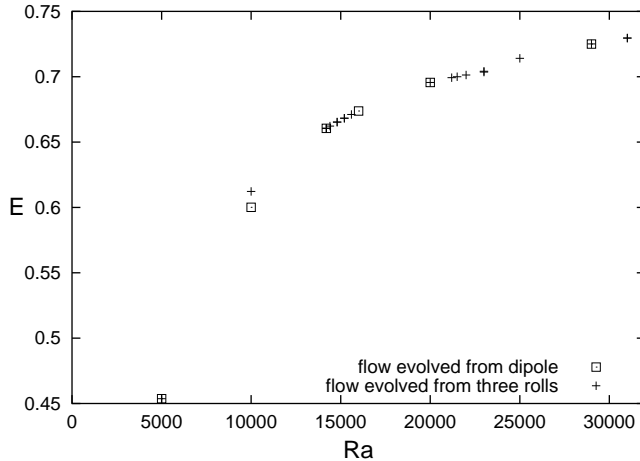


Figure 6.22: Squares: energy of the flow evolved from dipole state as a function of Rayleigh number; crosses: energy of the flow evolved from three-roll state (for comparison). At $Ra = 10000$ the dipole pattern evolves into a CO pattern.

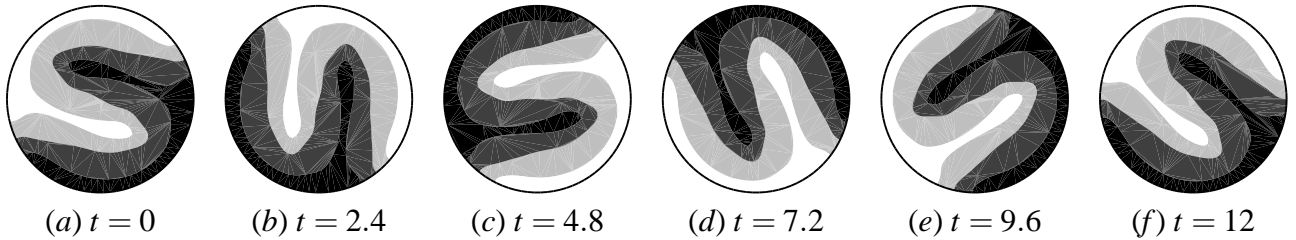


Figure 6.23: Rotating S pattern at $Ra = 12500$ at six different times.

6.10 Dipole-shaped perturbation

Finally we used as the initial condition the conductive state with a small perturbation. This protocol resembled that used in § 6.2 in that the amplitude was very small; the difference was the shape of the initial perturbation. In § 6.2, we started the simulations with an unrealistic, arbitrary sum of modes (figure 6.2, *a*). Here we used the transient dipole form, which appears for a three-roll state below the threshold ($Ra = 1200$) before the convective motions die completely (a pattern similar to that depicted on 6.3, *c*). We consider this initial condition as a perturbation to the conductive state rather than a converged pattern, as all the fields already have very small values, but it can be regarded also as a transient structure, observed during the evolution of the system, and thus reachable experimentally.

As in the case of initialisation with a well converged dipole pattern, for $Ra = 2000$ the simulation gives a stable dipole and for $Ra = 5000$ three rolls. However, for higher Rayleigh numbers, the dynamics is different. The dipole-shaped perturbation, used as initial condition at $10000 \leq Ra \leq 15000$, gives at first a transitional dipole smile and then a slowly rotating roll in the shape of the letter S, which we will refer to as a *rotating S pattern*. A visualisation of this time-dependent state at different times is displayed on figure 6.23 and the evolution of the temperature at two points is plotted in figure 6.24. The rotation is very slow: one period is of the order of ten, and the frequency grows with the Rayleigh number. Figure 6.25 shows the dependence of the frequency and energy of this type of flow on Rayleigh number.

The evolution of the dipole pattern at $Ra = 16000$ is shown on figure 6.26. It passes through an intermediary *three-part dipole pattern* before finally becoming a dipole-smile pattern. This

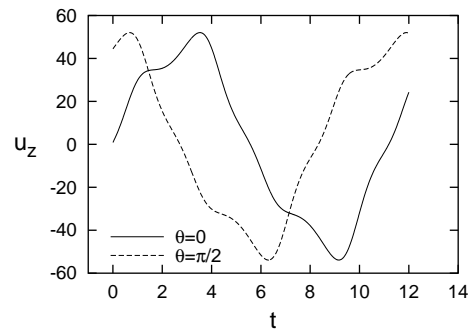


Figure 6.24: Evolution of vertical velocity in time for rotating S pattern at two points of the same r and z and different θ .

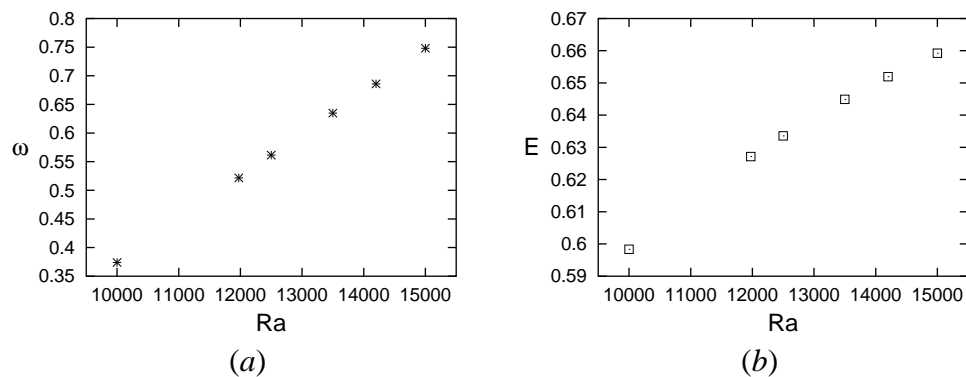


Figure 6.25: Frequency and energy of the rotating S pattern as a function of Rayleigh number.

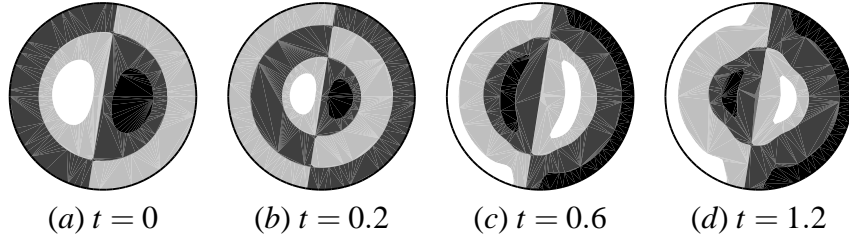


Figure 6.26: Evolution from dipole-shaped perturbation into a stable dipole smile pattern at $Ra = 16000$.

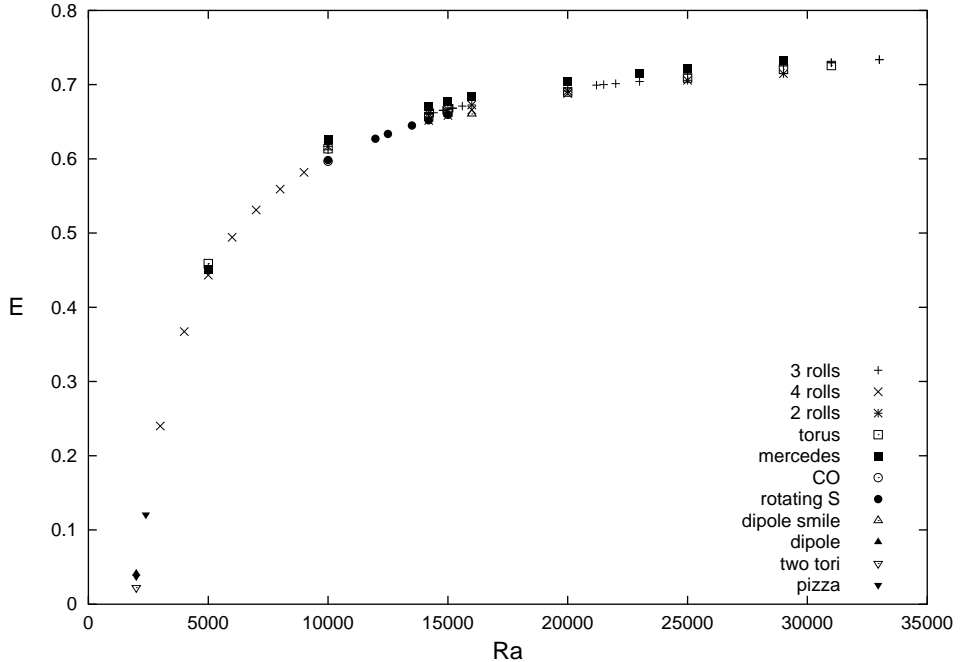


Figure 6.27: Energy of all stable patterns obtained for $\Gamma = 2$, $Pr = 6.7$ and insulating sidewalls as a function of Rayleigh number.

pattern, observed for $5000 \leq Ra \leq 15000$ as a transient pattern, seems to be stable for this Rayleigh number.

For $20000 \leq Ra \leq 29000$, the dipole pattern transforms at first into a transitional pattern, similar to dipole smile, then into an S roll and finally it becomes a stable three-roll flow. The transition occurs without any oscillatory evolution and the energy of the final state fits the already observed dependence between three-roll pattern energy and Rayleigh number.

6.11 Summary diagram

The energy of all stable patterns described above, as a function of Rayleigh number, is depicted on figure 6.27. The energy depends not only on the Rayleigh number, but also on the type of the convective pattern, but the values for different patterns obtained at the same Rayleigh number are very close. For every type of flow the energy grows with the Rayleigh number, faster close to the convection threshold and slower for higher Ra .

Figure 6.28 shows summary diagram with all the stable patterns found. The plotted value is the maximum of temperature deviation h over θ , $\max_\theta h(r = 0.3, \theta, z = 0)$, as a function of Rayleigh number (this guarantees the diagram to be independent of the azimuthal phase). Well

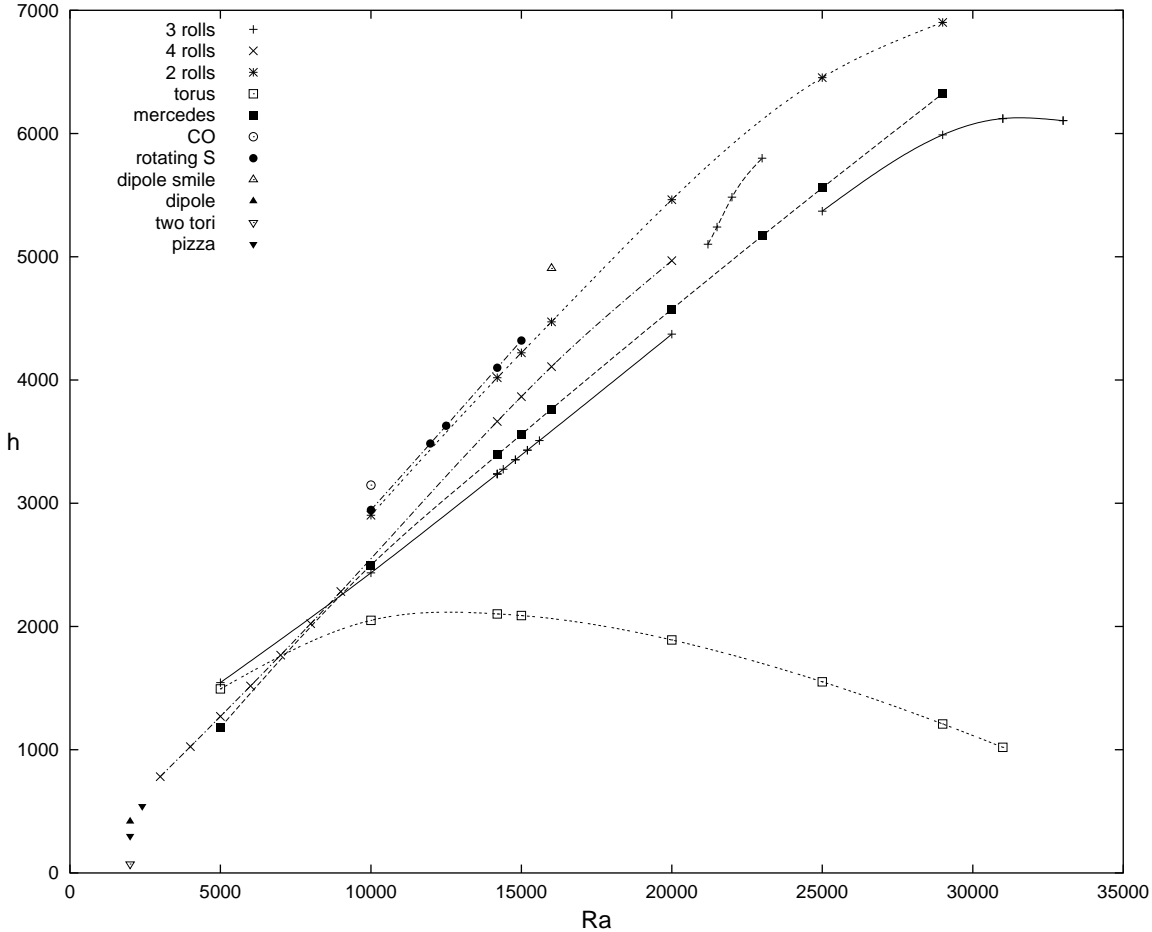


Figure 6.28: Summary diagram: temperature $\max_{\theta} h(r = 0.3, \theta, z = 0)$ as a function of Rayleigh number for all stable convective patterns found.

separated curves are visible for three, four and two parallel rolls, mercedes structure and toroidal roll. In a shorter stability interval there exists the rotating S pattern. The curve for three rolls is interrupted between $Ra = 20\,000$ and $Ra = 25\,000$: a branch detaches where the pattern, instead of converging, slightly shifts in the direction perpendicular to the rolls. At Rayleigh number $Ra = 2\,000$ there exist three stable patterns, different from those observed for higher Rayleigh numbers: dipole, pizza and two tori.

We have successfully simulated numerically all of the steady patterns obtained experimentally by Hof. For the same Rayleigh number $Ra = 14200$ we observed the five stable steady solutions they reported: a toroidal roll; two, three and four parallel rolls; and a three-spoke (“mercedes”) pattern. Additionally, we obtained the rotating S structure.

Chapter 7

Convective patterns – conducting sidewalls

We continue the description of the results we obtained in our numerical simulations of the experiment of Hof *et al.* (1999) at $\Gamma = 2$ and $Pr = 6.7$. The only difference from the configuration used in the previous chapter is that the cylinder sidewalls are assumed to be perfectly conducting, i.e. we apply homogeneous Dirichlet boundary conditions.

7.1 Start from perturbed conductive state

We proceeded in the same way as described in chapter 6 for a container with perfectly conducting sidewalls. This is less close to the parameters of the experiment Hof *et al.* (1999), as the sidewalls of their convective cell were made of well insulating material. A simplified diagram organising all the results is shown on figure 7.1. As before, we initialised the first series of simulations with a perturbed conductive solution at various Rayleigh numbers between 1900 and 40 000. The initial perturbation and final states are displayed on figure 7.2. For $Ra = 1900$ and 2000 the final state is of dipole form. For $2100 \leq Ra \leq 2500$, instead of the pizza pattern observed for the insulating case, we found an *hourglass* pattern of the same D_2 symmetry, but with the elongated cold spots touching each other at the centre. For $Ra = 2700$ and 4000 we obtained three rolls and for $6000 \leq Ra \leq 15\,000$ four rolls, which differ from the analogous patterns described in the previous chapter only at the sidewalls, as the deviation from conductive profile must be zero at the boundaries. For $Ra = 20\,000$ we observed a *Y* pattern (figure 7.2, *g*) with three bands of hot fluid in the shape of the letter *Y*. It is similar to the previously observed mercedes pattern, but has only one and not three symmetry axes. For $Ra = 25\,000$ we obtained a state in the form of a six-armed star, presented on figure 7.2 (*h*). For $Ra = 30\,000$ and above, up to 40 000, we obtained a pattern we call da Vinci, because of its resemblance with the sketch of human body proportions (figures 7.2, *i,j*). All these flows were stationary.

7.2 Three rolls

In this series of simulations we used as initial condition a three-roll pattern, previously converged at $Ra = 4000$. We then obtained stable three roll patterns for a wide range of Rayleigh numbers $3000 \leq Ra \leq 29\,000$, except for 25 000. The rolls become curved as the Rayleigh number is increased (see figure 7.3). In order to obtain a steady three-roll pattern at $Ra = 25\,000$, we must use the three-roll state obtained at $Ra = 20\,000$ as initial condition. If we follow our usual protocol and begin with the three-roll state obtained at $Ra = 4000$, the flow evolves instead,

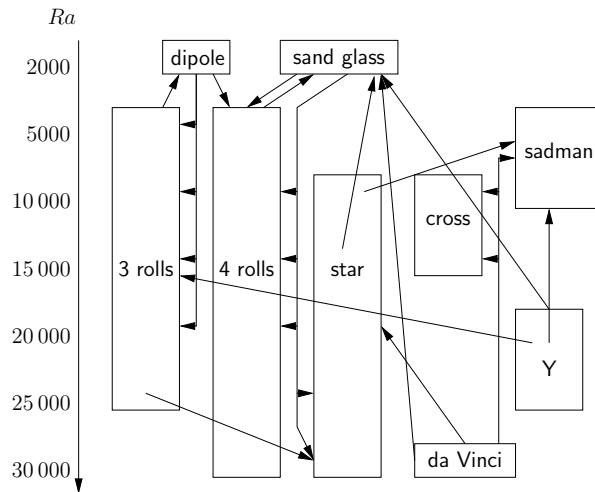


Figure 7.1: Schematic diagram of stability ranges and transitions between convective patterns as a function of Rayleigh number for $\Gamma = 2$, $Pr = 6.7$ and conducting sidewalls.

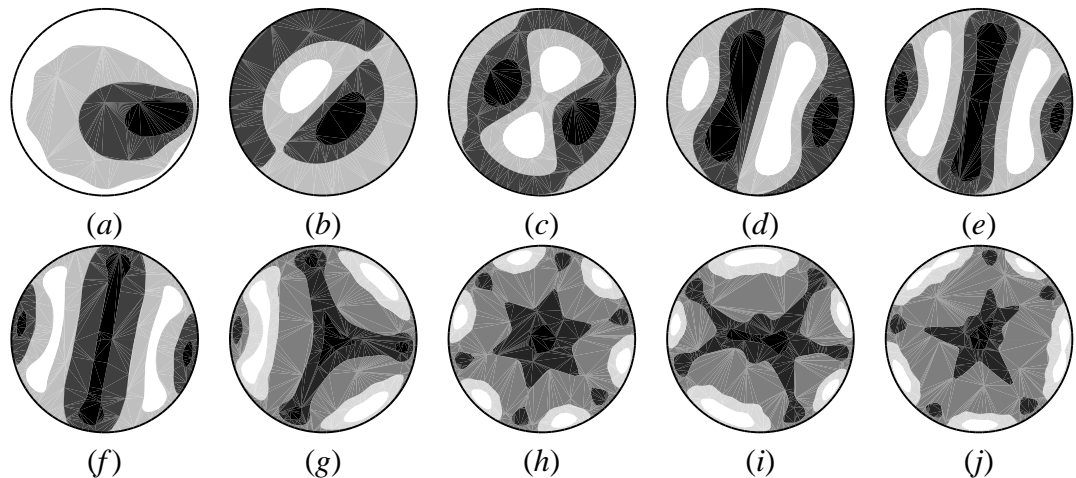


Figure 7.2: Arbitrary perturbation used for initialising simulations (a) and final patterns at various Rayleigh numbers: (b) dipole at $Ra = 2000$, (c) hourglass at $Ra = 2100$, (d) three rolls at $Ra = 4000$, (e) four rolls at $Ra = 6000$, (f) four rolls at $Ra = 15000$, (g) Y at $Ra = 20000$, (h) star at $Ra = 25000$, (i) da Vinci at $Ra = 30000$, (j) da Vinci at $Ra = 40000$.

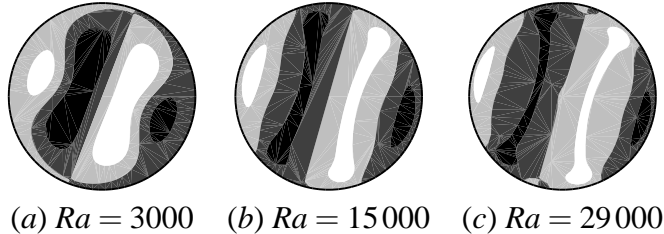


Figure 7.3: Stable three-roll patterns at different Rayleigh numbers.

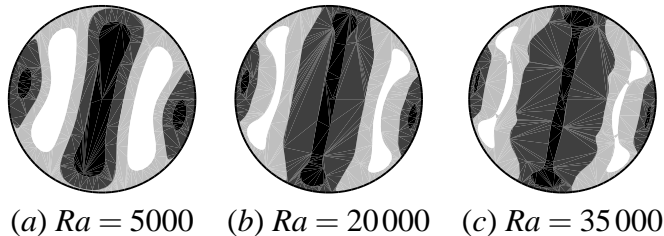


Figure 7.4: Stable four-roll patterns at different Rayleigh numbers.

probably towards a two-roll state. This occurs only at $Ra = 25\,000$; for 24 000 and 26 000 we obtained three stable rolls.

7.3 Four rolls

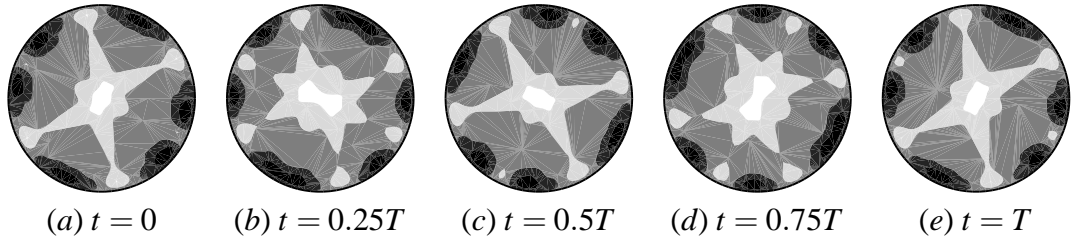
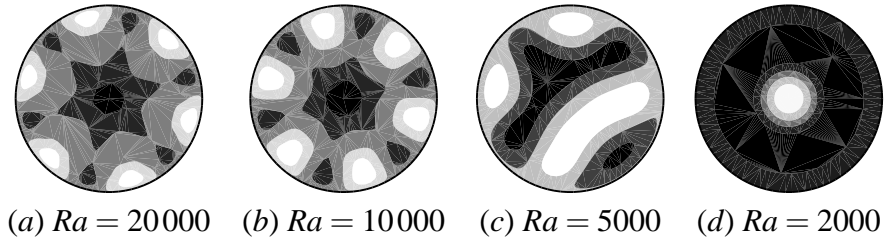
Every four-roll pattern we used as initial condition retained its structure within a large range of Rayleigh numbers $5000 \leq Ra \leq 35\,000$ (see figure 7.4). For $Ra = 2000$ the initial four-roll flow evolves into an hourglass pattern (like that on figure 7.2, c) and at $Ra = 40\,000$ it remains a four-roll pattern, but with the roll boundaries vibrating slightly with an oscillation period $T = 0.026$.

7.4 Evolution from dipole pattern

When we used the dipole pattern stabilised at $Ra = 2000$ as an initial condition at higher Rayleigh numbers, the flow evolved into three rolls for $Ra = 5000$ and four rolls for $10\,000 \leq Ra \leq 20\,000$. For $Ra = 25\,000$ we obtained a Y pattern (like that of figure 7.2, g). For $Ra = 30\,000$ the dipole flow evolves towards a three-roll state. As we know from previous simulations (§ 7.2), the three-roll flow is unstable at this Rayleigh number and this evolution should lead to a star pattern.

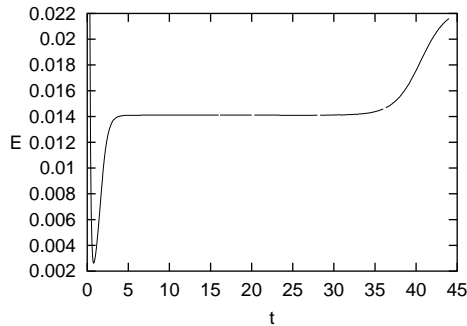
7.5 Evolution from hourglass pattern

For simulations initialised with the hourglass pattern (converged previously at $Ra = 2100$) we obtained: a stable hourglass pattern for $Ra = 2000$; four-roll flow for $5000 \leq Ra \leq 20\,000$; and a six-armed star for $Ra = 25\,000$ and 30 000. For $Ra \geq 35\,000$ a time-dependent state appears, which oscillates between a left-tilted and right-tilted X-letter shape passing via intermediate star-like patterns (see figure 7.5). The oscillation period is $T = 3.05$.

Figure 7.5: Oscillatory pattern at $Ra = 35\,000$.Figure 7.6: Convective patterns evolved from star flow: (a) star at $Ra = 20\,000$, (b) star at $Ra = 10\,000$, (c) sadman at $Ra = 5\,000$, (d) transient two tori at $Ra = 2\,000$.

7.6 Evolution from star pattern

In order to obtain patterns in the form of a six-armed star, we used as initial condition the star flow converged at $Ra = 25\,000$. Several final convective structures obtained for different Rayleigh numbers are presented on figure 7.6. The star flow remains stable for $10\,000 \leq Ra \leq 30\,000$ (figure 7.6, a-b). Below this range the initial pattern evolved into a *sadman pattern* (figure 7.6, c) at $Ra = 5\,000$ and an hourglass pattern at $Ra = 2\,000$. For both $Ra = 2\,000$ and $Ra = 5\,000$, axisymmetric transient patterns appear. For $Ra = 2\,000$ the transient state is composed of two concentric toroidal rolls, and its lifetime is about 30. Figure 7.7 shows the evolution of the energy during the transition from the initial star flow, through a long-lasting axisymmetric state into the asymptotic hourglass pattern. In the region where the axisymmetric state exists, the energy remains relatively constant.

Figure 7.7: Evolution of the system initialised with star pattern at $Ra = 2000$: energy as a function of time. Between $t = 5$ and $t = 35$ a long-lasting axisymmetric pattern exists.

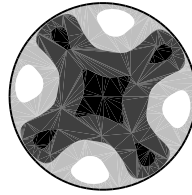


Figure 7.8: Cross pattern evolved at $Ra = 10000$ from da Vinci flow.

7.7 Evolution from da Vinci pattern

The da Vinci pattern (figure 7.2, *i*), used as initial condition, was stable only for $Ra \geq 30000$. For $Ra = 25000$ this structure evolves slowly towards a possibly stable five-armed star. For lower Rayleigh numbers the initial star flow evolves into: a star at $Ra = 20000$, a cross at 14200 and 10000 (figure 7.8), sadman at 5000 and hourglass at 2000.

7.8 Evolution from Y pattern

Having obtained the Y pattern at $Ra = 20000$ we reused it as initial condition. We found stable Y flows for Rayleigh numbers $20000 \leq Ra < 30000$. For $Ra = 14200$ the evolution led to three rolls. For lower Rayleigh numbers we obtained sadman patterns at $Ra = 10000$ and $Ra = 5000$ and hourglass at $Ra = 2000$. Since there is a resemblance between the sadman and Y pattern, these may be related, in the same way as straight three rolls at lower Rayleigh numbers are connected to curved four rolls at higher Rayleigh numbers.

7.9 Summary diagram

Figure 7.9 shows the energy of all stable patterns found for Dirichlet thermal boundary condition. As in the case of insulating sidewalls, the energy depends primarily on Rayleigh number, with a slight variation between types of convective patterns.

The bifurcation diagram is shown on figure 7.10. The maximum of temperature deviation $\max_\theta h(r = 0.3, \theta, z = 0,)$ is plotted as a function of Rayleigh number, for all stable patterns found. For higher Rayleigh numbers, several patterns remain stable on large intervals of Ra : three rolls, four rolls and star. Patterns da Vinci, Y and cross were observed in smaller ranges. For lower Rayleigh numbers we observed only two stable patterns: dipole and hourglass.

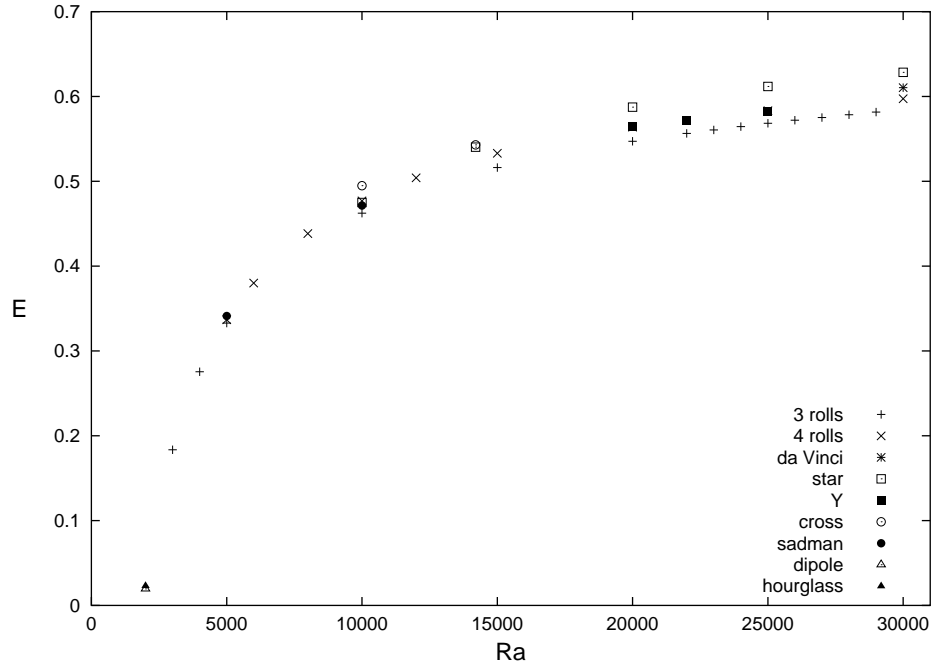


Figure 7.9: Energy of all stable patterns obtained for conducting sidewalls at $\Gamma = 2$ and $Pr = 6.7$ as a function of Rayleigh number.

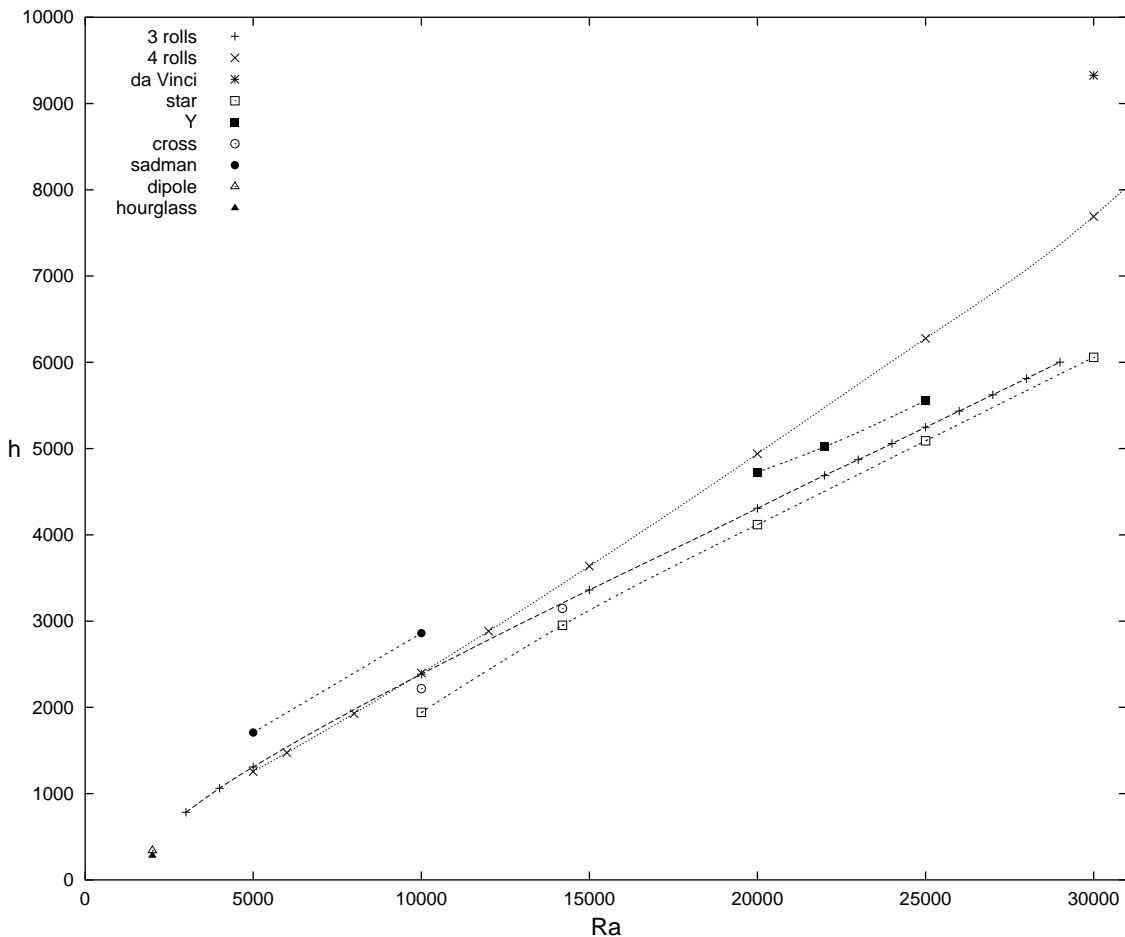


Figure 7.10: Summary diagram: temperature $\max_{\theta} h(r = 0.3, \theta, z = 0)$ as a function of Rayleigh number for all stable convective patterns found.

Chapter 8

Conclusion

We have presented the results of our three-dimensional simulations of convective flows for two different configurations. In the first part, we studied convective flows for aspect ratios $1.45 \leq \Gamma \leq 1.57$, Prandtl number $Pr = 1$ and insulating sidewalls. We conducted linear analysis of axisymmetric states. The critical Rayleigh numbers, frequencies and azimuthal wavenumbers of the eigenvectors found were in agreement with the results of Wanschura *et al.* (1996). We gave a prescription for obtaining a set of leading eigenpairs. We showed a presentation of the eigenvectors which takes into account the symmetries of the system: the eigenvectors corresponding to the same eigenvalue can take different spatial forms, with, or without nodal lines. Thus we explained and completed the results of Wanschura *et al.* (1996).

The theory of Hopf bifurcation in an $O(2)$ symmetry system predicts that the nonlinear evolution should lead to either standing or travelling waves. However, this is not possible to determine, using only linear analysis, which (if either) of these two solutions is stable. Our nonlinear simulations answered this question: travelling waves are the solution finally chosen by the system. Additionally, we succeeded in observing unstable standing waves. We evoked the results of Golubitsky & Stewart (1985) and Knobloch (1986) for Hopf bifurcation in the presence of $O(2)$ symmetry and we estimated the coefficients of the normal form describing the dynamics of the waves.

In the second part of our project we performed simulations with aspect ratio $\Gamma = 2$ and Prandtl number $Pr = 6.7$. Thus we matched the configuration of Hof, Lucas & Mullin (1999), who observed experimentally several different convective patterns at the same Rayleigh number. While their sidewalls were well insulating, we ran the simulations for both perfectly conducting and perfectly insulating sidewalls.

For both types of boundary conditions we found multiple stable solutions for the same Rayleigh number. We preserved the nomenclature of Hof (1997) and gave names to some novel patterns. We presented summary diagrams organising the complicated dependencies between the coexisting stable solutions.

Our simulations confirm the fact that, even for cylinders of small aspect ratio, the form of the convective flow depends not only on Rayleigh number, but also on the initial condition of time evolution. Furthermore, we observed this even for Rayleigh number as low as 2000, where we found up to three stable patterns.

We showed the existence of several long-lasting transient states, for example in the case of initialisation with a dipole pattern and conducting boundaries, for which the dipole smile state persisted for some time, with relatively constant energy, before transforming into the final three-roll flow. We believe classifying patterns as transitional is important for further study.

The behaviour of the system is influenced by the boundary conditions. Both the existence

and shape of the pattern are affected. For higher Rayleigh numbers and perfectly insulating boundary conditions, among the patterns we obtain are: two, three and four rolls, torus, mercedes and dipole smile. When we change the sidewalls to perfectly conducting, only three and four rolls can be observed. The axisymmetric state disappears and the mercedes state is replaced by the Y flow, thus losing its three-fold reflection symmetry. On the other hand, for conductive sidewalls, new cross and da Vinci flows appear. The other patterns, such as two rolls or dipole smile, may or may not also exist for conducting sidewalls. At lower Rayleigh numbers, insulating boundaries yield dipole, pizza and axisymmetric patterns. For conducting boundaries the dipole flow also exists, but the pizza pattern is replaced by hourglass and an axisymmetric pattern appears only as a transient state. In general, it seems that switching to perfectly conducting sidewalls makes some of the patterns lose their symmetries. This transition could be elucidated by performing a study in which intermediate values of sidewall conductivity would be used, and checking how the flow symmetry changes.

The results of our simulations for insulating sidewalls are in a good agreement with the experiment of Hof *et al.* (1999) – it was for the insulating case that we succeeded in obtaining all five steady patterns obtained experimentally by for $Ra = 14\,200$. Now we plan to conduct a quantitative comparison with experimental Nusselt numbers.

There are some disagreements between our observations and the Hof *et al.* (1999) experiments. Among the major ones is the fact that they suggested the existence of oscillatory flows above $Ra = 20\,000$. In contrast, although we found several time-dependent states, most patterns we observed above this threshold were steady.

An important part of our work was optimising and parametrising the spectral code that was not previously run in such high Rayleigh number regimes. We found the spectral resolutions and timesteps giving satisfying results and developed post-processing tools. However, we believe that a further reduction of resolution is possible, leading us to be optimistic about using the code in the future for larger aspect ratios.

Despite the great variety of flows we have obtained, we are far from an exhaustive study even for this specific configuration of control parameters. It is very likely that other stable solutions exist which we did not observe because they were topologically too far from any of our initial conditions. We also found many transitional patterns that should be studied more carefully in the future. There is still much work to be done in classifying the patterns and determining their exact stability limits. Many zones of the summary diagrams, especially the areas where new solutions appear, should be completed in the future. The dynamics of almost every pattern found could be an object of a separate study.

Close to the threshold (at $Ra = 2000$), for both types of boundary conditions, we observed different stable patterns, but none of them seem to be stable at higher Rayleigh number; conversely none of the patterns observed at higher Ra could be observed at $Ra = 2000$. We plan to study the Rayleigh number range over which the low- Ra patterns cease to be observed, in order to see whether this transformation is smooth or abrupt and how the new branches are created.

A study of time-dependent states is an aspect still open to future research. We observed several new time-dependent flows, but we believe that we are far from describing all existing unsteady solutions in the range of Rayleigh numbers simulated. Except for the rotating S pattern which exists for $Ra \approx 15\,000$, we observed oscillations mainly above $Ra = 30\,000$. It would also be interesting to reproduce the pulsing pattern found by Hof *et al.* (1999) at $Ra = 33\,000$, $\Gamma = 2$, $Pr = 6.7$, in order to determine whether this state, evolving from axisymmetric flow, is a result of a Hopf bifurcation similar to that we described in chapter 5.

At this stage of our investigation, we have surveyed the various flows which can be obtained from different initial conditions, following closely the experimental protocols. In the near fu-

ture, we plan to add Newton's method to the code. This procedure, instead of time stepping, solves the governing equations for steady states (see Mamun & Tuckerman, 1995). The initial fields converge then rapidly towards the closest solution, regardless of its stability. We would then conduct linear analysis to determine the stability along each branch of steady states. In contrast, the time-stepping procedure we used lets us follow the dynamics known from the experimental scenario, including transitions between the steady and time-dependent states. The patterns we obtained constitute a good preliminary survey for using a steady state solver and constructing a complete bifurcation diagram.

Recently, convection in small cylinders has received less interest than large containers. In our three-dimensional direct numerical simulations of convective regimes, we observed rich dynamics and a great variety of stable flows; we also reported some novel patterns. We hope that our results convince the reader that this chapter of hydrodynamical research is not yet thoroughly written.

Bibliography

- AHLERS, G., CANNELL, D. & STEINBERG, V. 1985 Time Dependence of Flow Patterns near the Convective Threshold in a Cylindrical Container. *Phys. Rev. Lett.* **54**, 1373–1376.
- BAJAJ, A. 1982 Bifurcating periodic solutions in rotationally symmetric systems. *SIAM J. Appl. Math.* **42**, 1078.
- BARKLEY, D. & TUCKERMAN, L. 1989 Traveling waves in axisymmetric convection: the role of sidewall conductivity. *Physica D* **37**, 288.
- BÉNARD, H. 1901 Les tourbillons cellulaires dans une nappe liquide transportant la chaleur par convection en régime permanent. *Ann. Chim. Phys.* **23**, 62–144.
- BODENSCHATZ, E., PESCH, W. & AHLERS, G. 2000 Recent Developments in Rayleigh-Bénard convection. *Annu. Rev. Fluid Mech.* **32**, 709–778.
- BUELL, J. & CATTON, I. 1983 The effect of wall conduction on the stability of a fluid in a right circular cylinder heated from below. *Journal of Heat Transfer* **105**, 255.
- BUSSE, F. H. 1978 Non-linear properties of thermal convection. *Rep. Prog. Phys.* **41**, 1929–67.
- CANUTO, C., HUSSAINI, M. Y., QUARTERONI, A. & ZANG, T. A. 1988 *Spectral Methods in Fluid Dynamics*. Springer-Verlag New York Inc.
- CHARLSON, G. & SANI, R. 1970 Thermoconvective instability in a bounded cylindrical fluid layer. *Int. Journal. Heat Mass Transfer* **13**, 1479–96.
- CHARLSON, G. & SANI, R. 1971 On thermoconvective instability in a bounded cylindrical fluid layer. *Int. Journal. Heat Mass Transfer* **14**, 2157–60.
- CHARLSON, G. & SANI, R. 1975 Finite amplitude axisymmetric thermoconvective flows in a bounded cylindrical layer of fluid. *J. Fluid Mech.* **71**, 209.
- CILIBERTO, S., PAMPALONI, E. & PÉREZ-GARCÍA, C. 1988 Competition between Different Symmetries in Convective Patterns. *Phys. Rev. Lett.* **61**, 1198–1201.
- COULLET, P. & IOOSS, G. 1990 Instabilities of one-dimensional cellular patterns. *Phys. Rev. Lett.* **64**, 866.
- CROQUETTE, V. 1989 Convective pattern dynamics at low Prandtl number: Part I and II. *Cont. Phys.* **30**, 113–133, 153–171.
- CROQUETTE, V., LE GAL, P. & POCHEAU, A. 1986 Spatial features of the transition to chaos in an extended system. *Physica Scripta* **T13**, 135.

- CROQUETTE, V., MORY, M. & SCHOSSELER, F. 1983 Rayleigh-Bénard convective structures in a cylindrical container. *J. Phys.* **44**, 293–301.
- CROSS, M. C. & HOHENBERG, P. C. 1993 Pattern formation out of equilibrium. *Rev. Mod. Phys.* **65**, 851–1112.
- GETLING, A. V. 1998 *Rayleigh-Bénard Convection*. World Scientific.
- VAN GILS, S. A. & MALLET-PARET, J. 1986 Hopf bifurcation and symmetry: travelling and standing waves on the circle. *Proc. Roy. Soc. Edinburgh* **104A**, 279.
- GOLUBITSKY, M. & STEWART, I. 1985 Hopf bifurcation in the presence of symmetry. *Arch. Rat. Mech. Anal.* **87**, 107.
- GOTTLIEB, D. & ORSZAG, S. A. 1977 *Numerical Analysis of Spectral Methods: Theory and Applications*. Philadelphia: SIAM.
- HARDIN, G. & SANI, R. 1993 Buoyancy-driven instability in a vertical cylinder: Binary fluids with Soret effect. Part 2: Weakly non-linear solutions. *Intl J. Numer. Meth. Fluids* **17**, 755.
- HOF, B. 1997 The visualisation of convective flow patterns in water in tilted cells with variable geometry. Master's thesis, University of Manchester, Department of Physics and Astronomy.
- HOF, B. 2003 Private communication.
- HOF, B., LUCAS, G. J. & MULLIN, T. 1999 Flow state multiplicity in convection. *Phys. Fluids* **11**, 2815–2817.
- KNOBLOCH, E. 1986 Oscillatory convection in binary mixtures. *Phys. Rev. A* **34**, 1538.
- KOSCHMIEDER, E. L. 1993 *Bénard cells and Taylor vortices*. Cambridge University Press.
- KOSCHMIEDER, E. L. & PALLAS, S. G. 1974 Heat transfer through a shallow, horizontal convecting fluid layer. *Int. Journal. Heat Mass Transfer* **17**, 991–1002.
- KUZNETSOV, Y. 1998 *Elements of Applied Bifurcation Theory*. Springer.
- LEONG, S. S. 2002 Numerical study of Rayleigh-Bénard convection in a cylinder. *Numerical Heat Transfer, Part A* **41**, 673–683.
- LORD RAYLEIGH 1916 On convective currents in a horizontal layer of fluid when the higher temparture is on the under side. *Phil. Mag.* **32**, 529.
- MAMUN, C. K. & TUCKERMAN, L. S. 1995 Asymmetry and Hopf bifurcation in spherical Couette flow. *Phys. Fluids* **7**, 80–91.
- MANNEVILLE, P. 1990 *Dissipative structures and weak turbulence*. Academic Press.
- MARCUS, P. S. 2004 Prediction of a global climate change on jupiter. *Nature* **428**, 828–831.
- MORRIS, S. W., BODENSCHATZ, CANNELL, D. S. & AHLERS, G. 1993 Spiral Defect Chaos in Large Aspect Ratio Rayleigh-Bénard Convection. *Phys. Rev. Lett.* **71**, 2026–2029.

- MÜLLER, G., NEUMANN, G. & WEBER, W. 1984 Natural convection in vertical Bridgeman configurations. *J. Cryst. Growth* **70**, 78–93.
- NORE, C. & TUCKERMAN, L. S. 1999 Three-dimensional Rayleigh-Bénard convection in a cylindrical domain. *Rapport d'activité du LIMSI*.
- NORE, C. & TUCKERMAN, L. S. 2000 Convection de Rayleigh-Bénard en cavité cylindrique. *Rapport d'activité du LIMSI*.
- PLAPP, B. B., EGOLF, D. A., BODENSCHATZ, E. & PESCH, W. 1998 Dynamics and Selection of Giant Spirals in Rayleigh-Bénard Convection. *Phys. Rev. Lett.* **81**, 5334–5337.
- PRESS, W., TEUKOLSKY, S., VETTERLING, W. & FLANNERY, B. 1997 *Numerical recipies in C*. Cambridge Univ. Press, ISBN 0 521 43108 5.
- ROSENBLAT, S. 1982 Thermal convection in a vertical circular cylinder. *J. Fluid Mech.* **122**, 395–410.
- RÜDIGER, S. & FEUDEL, F. 2000 Pattern formation in Rayleigh Bénard convection in a cylindrical container. *Phys. Rev. E* **62**, 4927–4931.
- SIGGERS, J. H. 2003 Dynamics of targets in low-prandtl number convection. *J. Fluid Mech.* **475**, 357–375.
- STORK, K. & MÜLLER, U. 1975 Convection in boxes: An experimental investigation in vertical cylinders and annuli. *J. Fluid Mech.* **71**, 231–240.
- TOUIHRI, R., BEN HADID, H. & HENRY, D. 1999 On the onset of convective instabilities in cylindrical cavities heated from below. I. Pure thermal case. *Phys. Fluids* **11**, 2078–2088.
- TUCKERMAN, L. 1989 Divergence-free velocity fields in nonperiodic geometries. *J. Comput. Phys.* **80**, 403–441.
- TUCKERMAN, L. S. & BARKLEY, D. 2000 *Bifurcation analysis for time-steppers*, in *Numerical Methods for Bifurcation Problems and Large-Scale Dynamical Systems*. Springer, New York, ed. by E. Doedel and L. S. Tuckerman.
- WANSCHURA, M., KUHLMANN, H. C. & RATH, H. J. 1996 Three-dimensional instability of axisymmetric buoyant convection in cylinders heated from below. *J. Fluid Mech.* **326**, 399–415.